Master's thesis

NTNU
Norwegian University of Science and Technology
Faculty of Natural Sciences
Department of Materials Science and Engineering

Nora Kvalsvik

# In situ formation of a polypyrrole-coating on a carbon-coated LiNi0.5Mn1.5O4 cathode in Li-ion batteries as a strategy for enhanced cycling stability.

Master's thesis in Materials Science and Engineering
Supervisor: Ann Mari Svensson
Co-supervisor: Muhammad Abdelhamid
June 2023

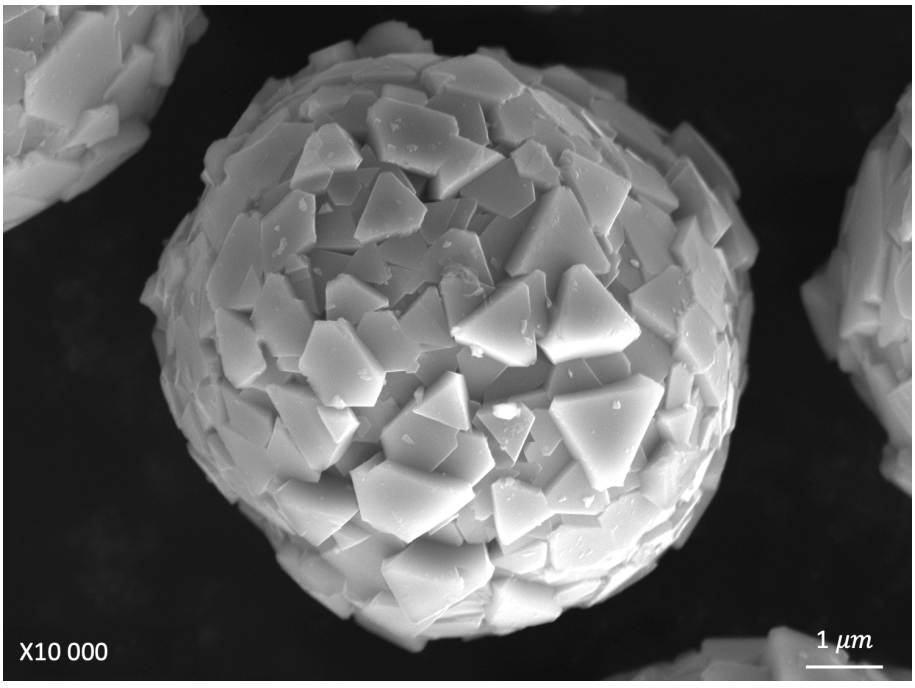


pristine LNMO particle

NTNU
Norwegian University of Science and Technology

IFE Institutt for energiteknikk

Nora Kvalsvik

# In situ formation of a polypyrrole-coating on a carbon-coated LiNi0.5Mn1.5O4 cathode in Li-ion batteries as a strategy for enhanced cycling stability.

Master's thesis in Materials Science and Engineering
Supervisor: Ann Mari Svensson
Co-supervisor: Muhammad Abdelhamid
June 2023

Norwegian University of Science and Technology
Faculty of Natural Sciences
Department of Materials Science and Engineering

NTNU
Norwegian University of
Science and Technology

# Preface

This project is a collaboration between IFE and NTNU, falling under the initiative Sustainable Materials for the Battery Value Chain (SUMBAT), in conjunction with IFE's internal project "Electrolytes and additives". Most of the work was conducted at IFE's battery lab, with additional testing performed at NTNU's Department of Materials Science and Engineering. The thesis is based on the findings from the specialization project, "In situ formation of a polypyrrole-coating on the $LiNi_{0.5}Mn_{1.5}O_2$ cathode in Li-ion batteries", done during the autumn of 2022 by the author. A summary of relevant key findings can be found in Appendix D. The theory and experimental part of the specialization project have been extensively elaborated and rewritten. However, some figures have been directly adapted from the specialization project and will be to referenced accordingly.

First and foremost, I want to thank my supervisor at IFE, Muhammad Abdelhamid, for his exceptional guidance. His expertise and insights have contributed to an enriching learning experience, which further sparked my interest in battery science. Additionally, I would like to thank Abirdu Woreka Nemag and Theresa Nguyen for their continuous cooperation and coordination at the Lab to ensure that I could complete all my experiments as intended. I also want to thank John Ostrander for the cross-section polisher training, David Wragg for XRD guidance, and Raphael Kuhan for XRD training and Hybridizer assistance. Thank you to the head of the IFE battery department, Hanne Flåten Andresen, for initiating the project. Lastly, I want to thank the rest of the IFE team for the exciting discussions and for making me feel welcome.

I want to extend my gratitude to my supervisor at NTNU, Ann Mari Svensson, for valuable feedback on my results, proofreading, and helpful discussions throughout the semester. Additionally, I want to thank Silje N. Bryntesen for taking the time to proofread parts of the project. Great help was also received by Johannes Ofstad for Raman training and Inger-Emma Nylund for the supply of LNMO powders. Lastly, thanks to the FACET battery group for providing input during weekly project meetings.

A special thanks to my beautiful family and friends for supporting me over the past five years. Especially, I want to thank my wife Marita. Her encouragement and great sense of humor have played a crucial role in keeping me motivated throughout this journey.

Oslo, 2023

*Nora Kvalsvik*

# Abstract

Li-ion batteries (LiBs) are currently the leading battery technology for portable devices and consumer electronics. Unfortunately, the dominant cathode materials used in these batteries contain cobalt, posing issues related to its toxicity, high cost, and ethical concerns. The high voltage cobalt-free cathode material $LiNi_{0.5}Mn_{1.5}O_2$(LNMO) has emerged as a cost-effective and environmentally friendly alternative to conventional cathode materials. The LNMO material operates at voltages up to 4.9 V vs. $Li/Li^+$, resulting in higher energy density. However, at such high operating voltages, the LNMO-electrolyte interface is unstable, suffering from parasitic side reactions and Mn and Ni dissolution. Thus, this project aimed to develop a double-layer coating to stabilize the LNMO electrode-electrolyte interface. Initially, a carbon coating was created, and then a pyrrole monomer was added to the electrolyte, leading to electropolymerization forming a protective polypyrrole coating on the carbon-LNMO composite during electrochemical cycling.

Acetylene was used as a carbon source to form a carbon coating on the LNMO particles via a chemical vapor deposition method. This led to a decomposition of the LNMO structure, likely due to a reducing atmosphere from the acetylene. Therefore, the carbon coating technique was switched to a dry coating process with a hybridizer machine and carbon black as the coating material. Scanning electron microscopy (SEM) images of the carbon-coated LNMO particles' surface and cross-sections revealed that a relatively thick (0-1.2 nm thickness) and non-uniform coatings had formed. The presence of the carbon coating was further confirmed via Energy-dispersive X-ray spectroscopy (EDX). X-ray diffraction (XRD) analysis showed that the carbon coating did not affect the LNMO crystal structure.

Galvanostatic cycling tests were conducted to investigate the effect of the carbon coating on LNMO's electrochemical properties. The carbon-coated and the non-carbon-coated LNMO had a similar initial discharge capacity in range 131-134 mAh/g at C-rate of C/20, indicating that the carbon coating did not contribute to the battery capacity. Despite the non-uniform and thick coating, the cells with carbon-coatings demonstrated improved cycling stability. After 60 cycles at C-rate C/10 the carbon-coated LNMO had a capacity retention of about 88-89 %, while uncoated LNMO only retained 82 %. The cells with carbon-coated LNMO generally experienced a lower degree of polarization, possibly explaining their improved cycling stability. All cells generally displayed unstable cycling performance after 80 cycles.

In rate capability tests, carbon-coated LNMO showed improved rate capability compared to the uncoated LNMO at all C-rates (C/10 - 2C). An intermittent current interruption test revealed that the cells with carbon coating had a lower internal resistance at the beginning of charge and end of discharge (from 5 - 35 % state of charge), indicating that the carbon coating led to enhanced electrical conductivity. The enhanced cycling stability and rate capability of cells with carbon-coated LNMO was attributed to enhanced electrical conductivity provided by the carbon coating. This may have allowed for better utilization of the LNMO active material and improved electrical contact between the LNMO particles and the current collector. Additionally, the carbon coating may have acted as a protective barrier against the electrolyte, hindering interfacial degradation.

The second part of the project investigated if carbon-coated LNMO particles could help to create a more uniform polypyrrole coating on the LNMO electrode during in-situ electropolymerization of pyrrole. In cyclic voltammetry tests with positive potential scans to 4.1 V vs. $Li/Li^+$, electropolymerization peaks for the cells containing 0.5 wt%pyrrole electrolyte additive were observed during the first cycle at about 3.8 vs. $Li/Li^+$. This indicated formation of a polypyrrole layer prior to electrolyte decomposition, which typically occurs at about 4.3 V vs. $Li/Li^+$. The presence of a polypyrrole layer was confirmed on the positive LNMO electrode by SEM images and raman spectroscopy. Moreover, the polypyrrole layer on the carbon-coated LNMO appeared more uniform than on the non-carbon-coated LNMO, confirming that a carbon coating could facilitate the formation of a more uniform polypyrrole coating.

From galvanostatic cycling tests, an electropolymerization process was confirmed upon the first charge cycle for the cells containing the pyrrole additive. Cells without carbon coating had an initial discharge capacity of 121 mAh/g, while cells with carbon coating had an initial discharge capacity ranging from 126-131 mAh/g. Both were generally lower compared to the cells without pyrrole (131-134 mAh/g). The polypyrrole layer should be electrochemically active, and with polypyrrole's lower theoretical specific capacity (72 mAh/g) compared to LNMO (140 mAh/g), the lower initial discharge capacity was expected. However, in prolonged cycling (up to 100 cycles) at high operating voltages (4.9 V vs. $Li/Li^+$), the polypyrrole layer led to poor cycling performances and did not

function as intended. A potential explanation for the reduced electrochemical performance could be that the polypyrrole was overoxidized, which may have destroyed its functional and electrochemical properties.

In summary, a pure carbon coating lead to improved electrochemical performance of LNMO based cells. A carbon coating also seems to help create a more uniform polypyrrole coating. However, the polypyrrole coating degraded the cell performance most likey due to its instability at high operating voltages (4.9 V). In future work, the uniformity and thickness of the carbon coating should be optimized. In addition, it should be a priority to find a functional polymer that can be electropolymerized via anodic oxidation and is stable at high operating voltages.

# Sammendrag

Li-ion batterier (LiBs) er den ledende batteriteknologien for bærbare enheter og forbrukerelektronikk i dagens marked. Konvensjonelle katodematerialer anvendt i disse batteriene inneholder ofte kobolt, som er giftig, dyrt, og ofte tilknyttet etiske kontroverser. Et katodemateriale som har fått mer oppmerksomhet nylig er $LiNi_{0.5}Mn_{1.5}O_2$ (LNMO), et kobolt-fritt materiale som opererer ved høy spenning, hvilket gjør det til et kostnadseffektivt og miljøvennlig alternativ. LNMO opererer på spenninger opp til 4.9 V vs. $Li/Li^+$, hvilket resulterer i høyere energitetthet. Imidlertid er grensesnittet mellom LNMO elektroden og elektrolytten ustabilt ved såpass høye driftsspenninger, hvor materialet lider av parasittiske sidereaksjoner samt oppløsning av Mn og Ni. Målet med dette prosjektet var derfor å utvikle et beskyttende belegg bestående at to lag for å stabilisere grensesnittet mellom LNMO-elektroden og elektrolytten. Først ble det konstruert et karbon-belegg, og deretter ble det tilsatt en pyrrol-monomer til elektrolytten. Under elektrokjemisk sykling ble pyrrol-monomeren elektropolymerisert for å danne et polypyrrol-belegg på karbon-LNMO-kompositten.

I første omgang ble acetylen brukt som karbonkilde for å danne karbon-belegget på LNMO-partiklene via kjemisk dampavsetting. Mest sannsynlig førte acetylen til en hydrogen-rik, reduserende atmosfære, som resulterte i at LNMO-strukturen ble ødelagt. Derfor byttet vi til en tørr beleggingsprosess med en hybridizer maskin, der carbon black ble brukt som beleggingsmaterial. Skannende elektronmikroskop (SEM)-bilder av LNMO-partikkelens overflate og tverrsnitt viste at et relativt tykt (0-1.2 nm tykkelse) og lite homogent karbon-belegg hadde blitt dannet. Karbon-beleggets forekomst ble videre bekreftet ved bruk av energi-dispersiv røntgen-spektroskopi (EDX). En røntgen-diffraksjons (XRD) analyse bekreftet at krystallstrukturen til LNMO ikke ble påvirket av karbon-belegget eller beleggsmetoden benyttet.

For å undersøke effekten av karbon-belegget på LNMO sine elektrokjemiske egenskaper ble det cellene syklet galvanostatisk. LNMO med og uten karbon-belegg hadde lik initial utladningskapasitet på mellom 131-134 mAh/g ved en C-rate på C/20. Dette indikerte at karbon-belegget ikke hadde noen effekt på batterikapasiteten, hvilket var forventet ettersom carbon black skal være elektrokjemisk inaktivt. Cellene med karbon-belegg viste forbedret sykle-stabilitet til tross for det tykke og lite uniforme belegget. Etter 60 sykler hadde karbon-LNMO cellene en kapasitetsretensjon på omtrent 88-89 % (C/10), mens cellene uten karbonlag hadde en kapasitetsretensjon på 82%. Cellene med karbonbelagt LNMO opplevde generelt sett en lavere grad av polarisering, hvilket kan forklare den forbedrede syklestabiliteten til karbon-LNMO cellene. Alle cellene hadde lav syklestabilitet etter 80 sykler.

For å undersøke effekten av karbon belegget ved økt C-rate, ble det utført en rate test. Cellene med karbon-LNMO viste en bedre ytelse en cellene uten karbon belegg på alle C-rater (C/20 - 2C). Resultatene fra en "intermittent current interruption" test viste en redusert intern celle resistans ved begynnelsen av opplading og ved slutten av utlading (fra 5 - 35 % state of charge) for karbon-LNMO cellene. Den redusere interne resistansen indikerte at karbon belegget mest sannsynlig førte til økt elektronisk ledningsevne. Basert på den forbedrede elektroniske ledningsevnen så ble den forbedrede syklestabiliteten og batteri ytelsen på høyere C-rate tilskrevet karbon belegget. Belegget kan ha tilrettelagt for bedre utnyttelse av LNMO aktivt materiale, samt forbedret den elektriske kontakten mellom LNMO-partiklene og strømsamleren. I tillegg kan karbon belegget ha fungert som en beskyttende barriere mot elektrolytten, noe som også kan ha bidratt til den forbedrede elektrokjemiske batteri ytelsen.

Den andre delen av prosjektet undersøkte om karbon belagte LNMO partikler kunne fasilitere dannelse av et uniformt polypyrrol belegg på LNMO-elektroden under in-situ elektropolymerisering av pyrrol. Fra sykliske voltammetri tester hvor potensialet ble skannet til 4.1 vs. $Li/Li^+$ ble det observert elektropolymerisasjonstopper under den første syklusen ved omtrent 3.8 vs. $Li/Li^+$ for alle cellene som inneholdt pyrrol. Dette indikerte at ett polypyrrole belegg ble dannet før dekomponering av elektrolytten, som vanligvis skjer ved omtrent 4.3 V vs. $Li/Li^+$. SEM-bilder og Raman spektroskopi bekreftet at ett polypyrrole belegg hadde blitt dannet på den positive LNMO elektroden. Polypyrrol belegget på karbon-LNMO partiklene fremsto også mer uniform enn på LNMO partiklene uten karbon belegg.

Fra galvanostatisk sykling, ble det også observert en elektropolymeriseringsprosess ved den første oppladnings syklusen for cellene som inneholdt pyrrol. Celler uten karbon belagte LNMO partikler hadde en initial utladningskapasitet på 121 mAh/g, mens celler med karbon-LNMO partikler hadde en initial utladningskapasitet mellom 126-131 mAh/g. Polypyrrol belegget skal være elektrokjemisk aktivt, og med polypyrrole sin lavere spesifikke kapasitet (72 mAh/g) sammenlignet med LNMO

(140 mAh/g), var den lavere initiale utladningskapasiteten forventet. Imidlertid, under langvarig sykling (opptil 100 sykluser) ved høye driftsspenninger (4,9 V vs. $Li/Li^+$), førte polypyrrol-laget til forverret sykle stabilitet. En mulig forklaring på den reduserte elektrokjemiske ytelsen kan være at polypyrrol belegget ble overoksidert, noe som kan ha ødelagt dets funksjonelle og elektrokjemiske egenskaper.

For å oppsummere, et karbon belegg førte til forbedret elektrokjemisk ytelse for LNMO-baserte celler. Karbon belegget ser også ut til å bidra til å danne ett mer uniformt polypyrrol belegg. Imidlertid ser det ut til at polypyrrol belegget forverrer cellens ytelse på grunn av dens ustabilitet ved høye driftsspenninger (4.9 V $Li/Li^+$). I fremtidig arbeid bør prioriteringen ligge på å utvikle et mer uniformt karbonbelegg med optimalisert tykkelse. Videre bør det være en høy prioritet å identifisere en funksjonell polymer som kan elektropolymeriseres ved anodisk oksidasjon og som forblir stabil ved høye driftsspenninger.

# Table of Contents

# Chapter 1

# Introduction

## 1.1 Background

For centuries burning of fossil fuels has led to increased greenhouse gas emissions and a global temperature rise [1]. In addition, Russia's invasion of Ukraine in February 2022 emphasized Europe's problematic dependence on Russia's gas supply. This has accelerated the EU's transition to renewable energy sources such as solar cells and wind turbines [1]. However, these sources are intermittent and require efficient energy storage to ensure a reliable and consistent energy supply. One of the actions to reduce global greenhouse gas emissions is the electrification of the transport sector. In order to achieve this, high-performing and energy-dense rechargeable batteries are essential [1].

Among various battery technologies, Lithium-Ion Batteries (LIBs) are the leading battery technology for most consumer electronics and electric vehicles due to their high energy density and long cycle life [2, 3]. Given that the energy stored in the LIBs and the power used to manufacture the battery origin from renewable energy sources, they offer a promising solution for reducing carbon emissions and ensuring efficient storage of excess energy from intermittent energy sources [4].

A conventional LIB consists of three main components; a graphite anode, a Li transition metal oxide cathode, and an electrolyte solution containing a salt dissolved in organic carbonates [5]. The dominant commercialized cathode materials, such as $LiNi_xMn_yCo_{1-x-y}O_2$ (NMC) and $LiNi_xCo_yAl_zO_2$ (NCA), contain a significant amount of the transition metals (TMs) Ni and Co. The cost of these TMs is often high and fluctuates due to their limited availability from geographically concentrated sources. Moreover, Co is toxic and associated with severe ethical controversies. To address these concerns and reduce costs, battery manufacturers have increasingly integrated the Co and Ni- free cathode material $LiFePO_4$ (LFP) into commercial LIBs despite its lower energy density compared to conventional cathode materials. Thus, this shift reflects the battery industry's growing emphasis on finding more ethical, sustainable, and cost-effective cathode material alternatives.

The energy density of a battery is determined by the product of the electrochemical potential difference between the electrodes and their specific capacity [6]. Thus, increasing the electrode's capacity and/or potential could improve the energy density. Therefore, the Co-free spinel $LiNi_{0.5}Mn_{1.5}O_2$ (LNMO) with its notably high operating voltage of 4.7 V (vs. $Li/Li^+$) has received increased interest from researchers and industry players. The LNMO material offers a comparable energy density to conventional cathode materials and a 19 % higher energy density than LFP. In addition, the LNMO structure exhibits a three-dimensional diffusion pathway that allows for fast extraction and insertion of $Li^+$ during the charge and discharge process of the battery, giving LNMO both a high rate capability and power density [7, 8, 9]. Despite these advantages, the LNMO material exhibits several issues that must be solved before it can be introduced to the commercial market. One major concern is the dissolution of Mn and Ni into the electrolyte, which can migrate to the anode and damage the anode's protective solid electrolyte interphase (SEI) layer. In addition, hydrofluoric acid (HF) may form with even trace amounts of water in the electrolyte, which in turn could attack the LNMO surface and accelerate the Mn and Ni dissolution. Furthermore, at operating voltages exceeding 4.3 V (vs. $Li/Li^+$), oxidative electrolyte decomposition of conventional electrolytes is an issue. This could lead to the deposition of unfavorable decomposition products at the LNMO surface and additional HF production causing further deterioration of the LNMO structure. All of these factors contribute to accelerated battery performance degradation

[10].

Several strategies have been proposed to stabilize the LNMO electrode-electrolyte interphase, where passivating surface coatings have been considered a viable approach. Various coating materials have been explored, such as $Al_2O_3$, MnO, ZnO, ZrO, and $SiO_2$. Despite some improvements, these coatings have not yet delivered the necessary cycling stability for practical applications due to non-uniform coatings and insufficient ionic and electronic conductivity [11, 10]. An interesting alternative is to use functional polymers with high ionic and moderate electronic conductivity. One such polymer is the well-known functional polymer polypyrrole (PPy). Gao et al. [12] reported that PPy-coated LNMO particles could suppress the dissolution of TMs and unfavorable electrode-electrolyte reactions. Before casting the electrodes, they chemically polymerized pyrrole (Py) onto the LNMO particles. An alternative approach to minimize production steps could be to use Py as an electrolyte additive and electropolymerize it onto the LNMO surface during the battery's initial charge and discharge cycles. The electropolymerization process of Py is accelerated in acidic solutions via protonation of the polymer chain [13]. Thus, the tendency of acidic solution to promote polymerization raises the possibility of consuming unfavorable HF while forming the PPy layer during cycling. Inhibition of HF could further limit TM dissolution. Moreover, Py is commercially available and easily oxidized [8]. Such an approach was explored during the author's specialization project in the autumn of 2022. The cathode electrode typically contains electrically conductive additives such as Carbon Black (CB), and it was observed that the PPy-layer had a preferential growth in these carbon-rich areas, resulting in a non-uniform coating. The non-uniform polymer growth was ascribed to the CB additive's higher electronic conductivity compared to the LNMO particles. Therefore, in this work, LNMO particles are carbon coated with the aim of creating a uniform PPy-coating. Carbon-coated cathode materials have been extensively researched, but mainly to enhance electron transport across the cathode interface and improve electrochemical performances. LNMO coated with a variety of different carbon materials and coating processes have also been previously researched [14, 15, 16, 17, 18, 19], where the majority of the results consistently demonstrate improved electrochemical properties.

A demonstration of how a carbon and PPy coating might function is presented in Figure 1.1. Realizing such a coating could offer a relatively straightforward solution to solve some of the more pressing issues that hinder LNMO deployment and pave the way for commercial production.

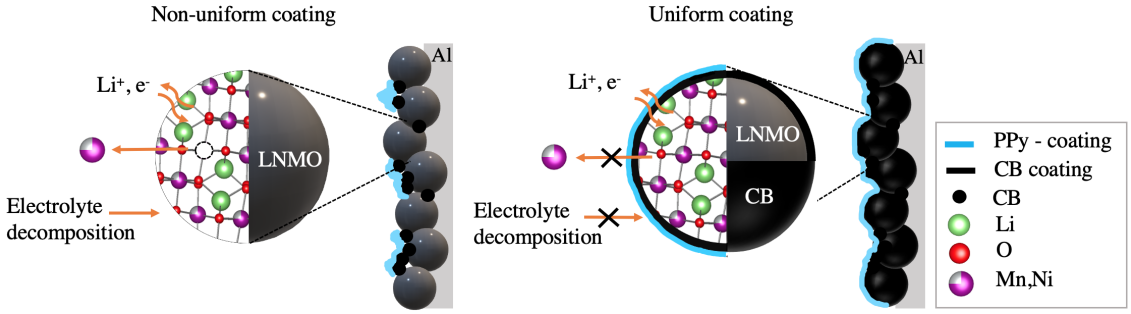


Figure 1.1: An illustration of how a carbon black (CB) coating could facilitate uniform polypyrrole (PPy)- coating on LNMO particles after electropolymerization of pyrrole (Py), where the resulting surface coatings can act as both an electrically and ionically conductive layer and a protective layer that mitigates Mn and Ni dissolution and electrolyte decomposition. Figure inspired by Gao et.al [12] and Østli et.al [11], LNMO structure made in VESTA.

## 1.2 Aim of Work

This project aims to enable the utilization of the environmentally friendly and economical LNMO cathode material in LIBs. The objective is to develop a protective double-layer coating to stabilize the LNMO electrode-electrolyte interface. To accomplish this goal, the LNMO particles are initially coated with carbon using two different techniques; chemical vapor deposition and a dry-coating process using a hybridizer machine. The electrochemical performance of the carbon-coated LNMO particles is investigated through galvanostatic cycling and intermittent current interruption. Once an adequate carbon coating with desirable electrochemical properties is obtained, pyrrole is used as an electrolyte additive and deposited onto the carbon-coated LNMO particles via electropolymerization during the first charge cycles. The electropolymerization process is conducted via cyclic voltammetry and galvanostatic cycling, which is also used to evaluate the carbon/PPy composite's electrochemical characteristics and performance. The surface layer's chemical composition and structural integrity are investigated post-mortem to verify the success of the different coating processes.

# Chapter 2

# Theory

## 2.1 The fundamentals of Lithium-ion batteries

A Lithium-ion Battery (LIB) is an electrochemical cell where electrical energy is stored as chemical energy during charging, which later can be converted back into electrical energy during charging. As illustrated in Figure 2.1, a LIB consists of an electrolyte, a separator, and two electrodes; an anode and a cathode. The electrodes are connected via an external circuit, enabling the flow of electric current. The electrolyte should possess high ionic and low electronic conductivity to direct electrons into the external circuit and effectively transport $Li^+$ between the electrodes. Generally, the electrolyte is a solution of lithium hexafluorophosphate ($LiPF_6$) salt dissolved in organic solvents and some additives to adjust its properties. The separator is made of a porous $Li^+$ permeable polymer material. Its role is to electrically and physically isolate the electrodes to prevent the cell from short-circuiting [5, 7].

The cathode, which serves as the source of $Li^+$, usually consists of a layered transition metal (TM) oxide (e.g., $Li_{1-x}M_yO_z$, where M=Co, Mn, Ni), also referred to as the active material (AM). The AM is typically mixed with the conductive agent carbon black and a polyvinylidene fluoride (PVDF) binder. The cathode material LNMO, which is the material used in this project, exhibit a spinel structure and is exemplified in Figure 2.1. The anode generally consists of graphite ($Li_xC_6$) with a layered structure. To ensure even distribution of electric current to and from the electrodes, the anode and cathode are coated onto current collectors [5].

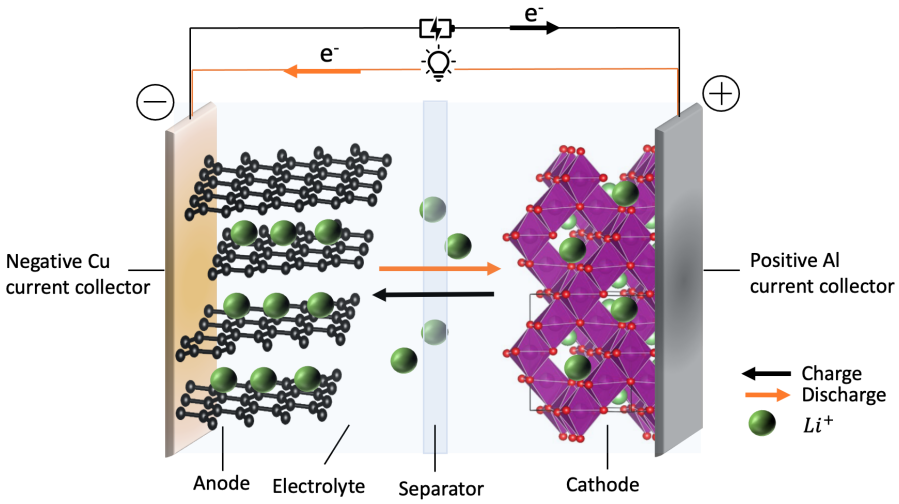


Figure 2.1: Illustration presenting the configuration of a LIB and the direction electrons and $Li^+$ move upon charge and discharge. Anode and cathode represent layered graphite and a spinel LNMO structure, respectively. Figure inspired by Leuthner et al.[5], and graphite and LNMO structure are made in VESTA.

During discharge, the anode undergoes oxidation as $Li^+$ are deintercalated from the graphite

layers, releasing one electron per extracted $Li^+$. The electrons flow into the external load circuit, and the electric current can be used to perform work. The $Li^+$ migrate through the electrolyte and intercalate into the cathode structure, where host TMs are reduced. The battery operates in galvanic mode during discharge, with reactions happening spontaneously. During charging, the battery operates in electrolytic mode, which requires the application of an external voltage to initiate the reverse reaction. The cathode is oxidized, and the $Li^+$ returns to the anode, which is simultaneously reduced. The cathode and anode's ability to undergo both reduction and oxidation makes a LIB rechargeable. Rechargeable batteries are typically referred to as secondary batteries [5, 7]. The electrodes are conventionally named according to their function during discharge. The cathode and anode reactions during charge and discharge are presented in Equations 2.1 and 2.2, with TM representing transition metals like Co, Mn, and/or Ni [20]. The flow of electrons and $Li^+$ is further visualized in Figure 2.1.

$$\text{Cathode reaction} \qquad \mathrm{xLi^+ + Li_{1-x}(TM)_yO_z + xe^- \underset{\text{Charge}}{\overset{\text{Discharge}}{\rightleftharpoons}} Li(TM)_yO_z} \tag{2.1}$$

$$\text{Anode reaction} \qquad \mathrm{Li_xC_6 \underset{\text{Charge}}{\overset{\text{Discharge}}{\rightleftharpoons}} xLi^+ + 6\,C + xe^-} \tag{2.2}$$

$$\text{Total reaction} \qquad \mathrm{Li_{1-x}(TM)_yO_z + Li_xC_6 \underset{\text{Charge}}{\overset{\text{Discharge}}{\rightleftharpoons}} Li(TM)_yO_z + 6\,C} \tag{2.3}$$

### 2.1.1 Terminology and Figures of merit

To enhance the readability of this thesis, this section outlines key terms and parameters used to evaluate battery performance.

The difference in electrochemical potential between the cathode ($\mu_C$) and the anode ($\mu_A$) is defined as the **cell voltage** (V). The cell voltage is the is the driving force behind the redox reactions during (dis)charge. If no current is drawn to/from the battery, the voltage is referred to as the **open circuit voltage**, $V_{OC}$, which is expressed as:

$$V_{OC} = (\mu_C - \mu_A)/e \tag{2.4}$$

Where $e$ is the elementary charge. However, upon charging the battery usually experience internal resistances ($R_i$) requiring an increase in the potential to overcome. These resistances typically arise from; resistance to current flow (ohmic resistance), (de)intercalation of $Li^+$ in the electrode materials (activation overpotential), and $Li^+$-diffusion between the electrodes (concentration overpotential). The total of these overpotentials gives a net polarization ($\eta$), resulting in a decreased output voltage ($V_{dis}$) and increased input voltage ($V_{ch}$), hence a deviation from the ideal $V_{OC}$. The extent to which ($V_{dis}$) and ($V_{ch}$) are affected is dependent on the discharging current ($I_{dis}$) and charging current ($I_{ch}$), and the $R_i$ which is related to the state of charge (q) according to [6]:

$$V_{dis} = V_{OC} - \eta(q, I_{dis}) = V_{OC} - I_{dis}R_i \tag{2.5}$$

$$V_{ch} = V_{OC} + \eta(q, I_{ch}) = V_{OC} + I_{ch}R_i \tag{2.6}$$

Before battery cycling, a **cut-off voltage** is set to avoid side reactions, and thus, enhance safety [6]. It should be noted that the cell voltage is a relative term, and in accordance with most research on LIB's where Li metal is used as the counter electrode in coin half-cells, all voltages presented will herein be referred to versus $Li/Li^+$.

The **capacity** of a battery is the amount of electrical charge the battery can accumulate during charge and deliver over time, and is usually expressed in Ampre hours (Ah). The specific capacity term where capacity is specified as capacity per unit weight AM (mAh/g) is, however, more frequently used in the field of batteries. The theoretic specific capacity ($Q_{s,th}$) of each individual electrode can be determined, as follows [20]:

$$Q_{s,th} = \frac{nF}{M_w} \tag{2.7}$$

Where $n$ is the number of electrons transferred per redox reaction, $M_w$ is the molecular weight of AM and F is the Faraday constant. The total specific capacity of the battery is determined by the specific capacity of the cathode ($Q_A$) and anode ($Q_C$) according to the equation:

$$Q = \frac{Q_A Q_C}{Q_A + Q_C} \tag{2.8}$$

Typically, the specific capacity of the cathode is lower than the anode, making the cathode the limiting electrode for the overall battery performance. In practice, the capacity is also limited by temperature, kinetic limitations of electrochemical reactions, inactive electrode materials (such as separator, binder, current collectors etc.) and cell design. Therefore, the practical specific capacity ($Q_{s,p}$) is usually lower than the theoretical. The $Q_{s,p}$ can be determined from a time-voltage curve obtained experimentally through galvanostatic cycling tests and calculated using the following equation:

$$Q_{s,p} = \frac{iAt_c}{3600M} \tag{2.9}$$

Where $i$ is the current density, $A$ is the electrode area, $t_c$ is the time in seconds until cut-off voltage, and $M_w$ is the molecular weight of AM.

The total amount of **energy** stored in a battery is determined by the product of its capacity (Q) and operating voltage (V), which yields:

$$E(Wh) = QV \tag{2.10}$$

The energy stored is more commonly expressed as energy energy per weight (Wh/kg) or per volume (Wh/L), known as the **energy density**. Developing electrodes with higher operating voltages and/or increased capacities could consequently contribute to improved energy densities.

A battery's **shelf life** is how long it can be stored without usage before it expires or requires recharging [6]. **Cycle life** is the total number of charge/discharge cycles the battery can sustain. The cycle life is referred to by multiple terms including cycling stability, cyclability, capacity retention, and reversibility. The two former are more general, while capacity retention refers to the percentage of initial capacity remaining after a certain amount of cycles. Typically, LIBs in EV's are considered at their end of life when the capacity retention is less than 80%. Reversibility, which is linked to the cyclability, is described by the **Coulombic Efficiency (CE)**, which signifies the proportion of $Li^+$ the LIB can utilize from the previous charge. If CE is less than 100% it implies an **irreversible capacity loss (ICL)**, which is defined as follows: [6]:

$$ICL(\%) = 100\% - CE(\%) = 100\% - \frac{Q_{dis}}{Q_{ch}}100 \tag{2.11}$$

The **C-rate** is the rate at which the battery is charged/discharged. It is calculated by dividing the theoretical capacity by the number of hours to charge or discharge the battery fully. For example, a C-rate of 1C means that the battery will be fully charged in 1 hour and discharged in 1-hour [21]. The **rate capability** is the LIB's ability to deliver a certain capacity at high C-rates.

In the field of batteries, there is always a compromise between the different parameters, and their importance varies based on the intended application area. Portable batteries should prioritize a high energy density and safety, whereas stationary batteries (e.g., energy storage from wind turbines and solar cells) should focus on long cycle life, self-life and efficiency. Common for all battery types, however, is that cost and sustainability aspects should always be considered.

## 2.2 Anode materials

To date, the most widely used anode material in LIBs is graphite, favored for its low working potential vs. $Li/Li^+$, availability, low price, and stable performance. As mentioned in Section 2.1, the graphite anode features a layered structure that enables it to efficiently store and (de)intercalate $Li^+$ during the charge and discharge process (e.g., $6\,C + Li^+ + e^- \rightarrow LiC_6$).

To achieve high energy density, Li-metal is considered the optimal anode material due to its lightweight nature and low electrochemical potential (-3.05 vs SHE), as well as its remarkably high theoretical specific capacity (3869 mAh/g). However, using Li-metal in a full-scale LIB poses serious safety concerns due to the risk of Li-dendrite formation, which could cause the battery to

short-circuit. Despite this, Li-metal is often the preferred anode in research coin cells where safety is less of a concern. These cells are commonly referred to as half cells. Unless stated otherwise, all coin half-cells presented in this thesis are cycled against Li-metal. Using Li-metal instead of graphite minimizes sources of error by providing an "infinite" supply of $Li^+$ [22].

Various alternative anode materials have also been suggested, such as alloys (e.g., Li-Si, Li-Sn, Sn-Co-C), oxides ($TiO_2$, $Li_4Ti_5O_{12}$, intermetallics (e.g., $Cu_6Sn_5$, InSb and CuSb), as well as conversion-type materials (e.g., fluorides, hydrides, nitrides, sulfides, phosphide, and oxides) [22, 23]. Among these materials, Si anodes have received particular interest due to their impressive capacity of about 4000 mAh/g. However, the use of pure Si as an anode material is not possible due to its large volume changes (about 300 %) during charge/discharge. To overcome these challenges, the combination of silicon and graphite composite is regarded as a promising solution.

## 2.3 Cathode materials

As mentioned in Section 2.1.1, the cathode is considered the limiting electrode for the battery performance because of its lower specific capacity compared to the anode. Moreover, the cathode contains expensive TMs, making it the primary cost factor of the LIB. Therefore, extensive research has been conducted over the past three decades, all striving to develop cathode materials that meet the following criteria [2]:

- Reversible (de)intercalation of a large amount of $Li^+$ while the crystal structure remains relatively unchanged.
- High electronic conductivity to ease the addition and removal of electrons.
- High $Li^+$ diffusivity to enable high power density
- High oxidation potentials vs $Li/Li^+$.
- Chemically stable towards other cell components.
- Cost-effective, and environmentally friendly.

It is, however, challenging to find cathode materials that fulfill all requirements, and a compromise is often made based on the intended application area. The cathode materials can be categorized into three primary groups based on their crystal structure, where Table 2.1 presents the most common.

Table 2.1: Properties of the most common cathode materials used in LIBs according to Akhilash et al.[2], Blomgren et al.[24], and Østli et al.[11].

| **Structure** | **Cathode material** | **Specific capacity mAh/g** | | **Average discharge voltage (V) vs $Li/Li^+$** |
|---|---|---|---|---|
| | | **Theoretical** | **Practical** | |
| Layered | $LiCoO_2$ (LCO) | 274 | 140 | 3.9 |
| | $LiNi_{1/3}Mn_{1/3}Co_{1/3}O_2$ (NMC111) | 275 | 160 | 3.8 |
| | $LiNi_{0.8}Mn_{0.1}Co_{0.1}O_2$ (NMC811) | 275 | 200 | 3.8 |
| | $LiNi_{0.8}Co_{0.15}Al_{0.05}O_2$ (NCA) | 280 | 160 | 3.8 |
| Olivine | $LiFePO_4$ (LFP) | 170 | 150 | 3.5 |
| Spinel | $LiMn_2O_4$ (LMO) | 148 | 120 | 3.8 |
| | $LiNi_{0.5}Mn_{1.5}O_2$ (LNMO) | 147 | 130 | 4.75 |

In the early 1990s, the layered $LiCoO_2$ (LCO) became the first cathode material introduced into the commercial LIB market. The structure has a two-dimensional diffusion channel facilitating for a fast $Li^+$ transport. However, the LCO cathode is limited to a voltage window of 3.0 - 4.2 V due to the potential risk of oxygen evolution at voltages exceeding 4.2 V. Within this voltage window, only 50% of the theoretical capacity (140 mAh/g) is accessible as only half of the $Li^+$ can be extracted from the host structure. Furthermore, the high cost and toxicity of Co have led researchers to seek alternative materials, resulting in the development and commercialization of the layered cathode materials $LiNi_xMn_yCo_yO_2$ (NMC) and $LiNi_xCo_xAl_xO_2$ (NCA). The Co content was reduced by partly substituting Co with Ni. However, the Ni amount had to be restricted due to

the risk of cation mixing (disordering between TM sites in the structure) and Ni jumping into the Li-layer, despite Ni being the main electroactive species. Increased structural and thermal stability was achieved by incorporating Mn (in NMC) or Al (in NCA), which are both more abundant and less toxic than Ni and Co. However, limitations on the amount of Mn and Al are necessary as they are electroctrochemically inactive in the form of $Mn^{3+}$ and $Al^{3+}$, thereby constraining the theoretical capacity. Hence, a moderate amount of Mn (in NMC) and Al (in NCA) will diminish cation mixing and enhance structural stability while still maintaining a reasonably high practical capacity [2]. Although NMC and NCA offer an advantageous combination of properties, such as power density, cycle life, and thermal stability, their Ni and Co content is still unfavorable.

Recently, the Co and Ni free olivine type $LiFePO_4$ cathode material has been increasingly used in commercial LIBs despite its lower energy density compared to NCA and NMC. This is primarily due to its desirable safety features, the abundance of Fe, low cost, and stable electrochemical and chemical properties. The main drawback of LFP, except from its low energy density, is its low intrinsic electronic ($10^{-9}$ S/cm) and ionic conductivity [25].

Lastly, the spinel structure of $LiMn_2O_4$ (LMO) exhibits three-dimensional pathways that allow for rapid $Li^+$ diffusion, which gives a high rate capability and power density [8]. However, the energy density of LMO is limited due to its low theoretical capacity and narrow operating voltage window (3-3.8 V). The LMO structure also has serious challenges related to Mn dissolution. The energy density can be significantly enhanced by doping the LMO structure with Ni, where the resulting $Li_{0.5}Mn_{1.5}O_2$ (LNMO) material still maintains the spinel structure and three-dimensional pathways of LMO. This energy gain is primarily attributed to the presence of $Ni^{4+/3+}$ and $Ni^{3+/2+}$ redox couples, which generate high voltage plateaus of about 4.75 V and 4.7 V, respectively [10]. Furthermore, LMNO exhibits a relatively high electronic conductivity (ranging from $10^{-5}$ to $10^{-7}$ S/cm), which makes it a suitable cathode material for high-power applications, such as electric vehicles [26]. However, LNMO suffers from fast capacity fade, especially in full cells and at elevated temperatures, which hinders the commercialization of LNMO-based cells.

### 2.3.1 The crystal structure of LNMO

The LNMO material exhibits two different types of spinel crystal structures, the ordered simple cubic and the disordered face-centered cubic structure represented by the $P4_332$ and the Fd-3m space group, respectively (Figure 2.2). In the ordered structure, the Ni, Mn, and Li cations are located at the 4b, 12d, and 8c sites, respectively. The O anions occupy the 24e and 8c positions. In the disordered phase, the Ni and Mn cations occupy the 16d sites randomly, while the Li cations are located at the 8c site. The O anions are positioned at the 8c and 24e sites [27, 26].

The type of crystal structure depends on the annealing temperature during synthesis. With an annealing temperature $\leq$ 700 °C, the LNMO has been reported to yield the ordered phase. In the ordered phase, during (de)lithiation, the $Ni^{2+/4+}$ redox couple compensates for charge neutrality while the $Mn^{4+}$ remains constant. Hence the $Ni^{4+/3+}$ and $Ni^{3+/2+}$ are the only redox couples contributing to the high voltage plateaus. At temperatures $\geq$ 700 °C, the disordered phase is favored. At these high temperatures, oxygen is lost from the structure, resulting in some $Mn^{4+}$ being reduced to $Mn^{3+}$ to maintain charge neutrality. The $Mn^{4+/3+}$ redox couple introduces an additional voltage plateau at around 4.1 V during (de)lithiation, causing a decrease in energy density as compared to the ordered phase. In addition, temperatures $\geq$ 750 °C lead to further oxygen depletion and the emergence of an electrochemically inactive rock-salt phase. Nevertheless, if the cooling process is sufficiently slow, this phase can be reversibly transformed back to the spinel phase.

Despite the lower energy density, the disordered phase generally possesses better cycling stability and rate capability than the ordered phase. However, the exact cause for this improvement remains uncertain. Kundurachi et al.[28] suggested that electron transfer between $Mn^{3+}$ and $Mn^{4+}$ may be a contributing factor to the higher electronic conductivity observed in the disordered phase, and thus its increased rate capability. Aktekin et al.[10] argued that the improved rate capability and cycle stability were mainly due to higher structural stability of the disordered phase in low lithiation states (i.e. at high voltages). Anyhow, achieving a completely ordered or disordered phase in reality is challenging. Therefore, the LNMO powders presented in the majority of literature are likely to have a certain degree of partial ordering-disordering. This could be an advantage as a partial order-disorder structure could offer a higher capacity due to ordering, and better cycle life and rate capability due to disordering [10].

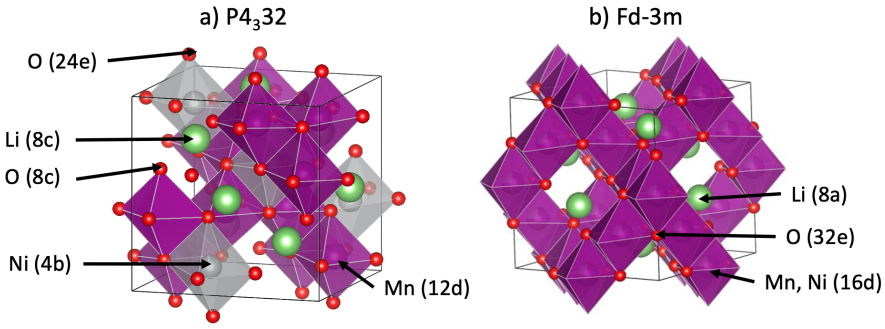


Figure 2.2: LNMO crystal structure with the atom's respective crystal sites for the (a) ordered (b) disordered structure. Figure inspiered by Aktekin et al. [10], LNMO structure made in Vesta.

Østli et al.[11] investigated the electrochemical performance of coin half cells using a partly disordered LNMO cathode, a Li-metal anode, and a 1M LiPF6, 1:1 EC:DEC electrolyte system. By cycling the cells galvanostatically between 3.6 - 4.9 V, they achieved an initial discharge capacity of 136 mAh/g at C/10. After 150 cycles, a capacity retention of 62.5% was reported. They used an average LNMO loading of 5 mg/cm$^2$ and 1C corresponded to 140 mAh/g. The LNMO powder used was supplied by Haldor Topsøe. For comparison, Yang et al.[14] achieved an initial discharge capacity of 115 mAh/g using a non-commercially synthesized partly disordered LNMO material as a cathode, a Li metal anode, and a 1M LiPF6, 1:1 EC:DMC electrolyte system. They used an average LNMO loading of 3 mg/cm$^2$, and the cells were cycled between 3 - 4.95 V.

## 2.4 The electrolyte

The main function of the electrolyte is to serve as a medium for the migration of $Li^+$ between the electrodes. This function is critical because the $Li^+$ mobility determines the rate of electrochemical reactions and, thus, the battery's power output. Various classes of electrolytes exist, including aqueous, nonaqueous, ionic liquid, polymeric, and solid electrolytes. Today, the multi-component system composed of conducting salts, non-aqueous solvents, and additives dominates the LIB market. This work also employs this particular class of electrolyte. As stated by Harting et al.[5], an electrolyte should fulfill the following criteria:

- High ionic conductivity, which is crucial for efficient transport of $Li^+$ between electrodes.
- Should be electrically insulating to force electrons into the external circuit and prevent short circuits.
- Consistent cycling and performance over a a wide temperature range (-40 to 80 °C) and throughout numerous cycles.
- A large electrochemical stability window to prevent electrolyte decomposition.
- Compatible with other battery components in all operating conditions.
- Environmental, safety, and economic concerns should be considered.

The operating voltage of a battery is restricted by the electrochemical window of the electrolyte, which is determined by the energy difference (Eg) between the lowest unoccupied molecular orbital (LUMO) and the highest occupied molecular orbital (HOMO), as illustrated in Figure 2.3. To prevent electrolyte decomposition, the anode ($\mu_A$) and cathode ($\mu_C$) potential should lie below LUMO and above HOMO, respectively; if not, the electrolyte will be reduced on the anode or oxidized on the cathode. This leads to the formation of a passivating solid electrolyte interphase (SEI) film on the electrode surfaces. As the anode in most electrode/electrolyte combinations lies slightly outside the stability window, an SEI layer is typically formed during the first cycles [29]. Given that the SEI layer is not too thick, the layer allows for $Li^+$ transport through the film, thus avoiding polarization. Moreover, the SEI protects the anode from direct contact with the electrolyte and may limit the clustering of electrochemically active species. Although the layer

confers certain benefits, it may also increase internal resistance and consume parts of the $Li^+$ from the cathode, ultimately resulting in reduced capacity and power output [29]. At high operating voltages, typically above 4.5 V, a cathode solid interphase layer (CEI) may form. In contrast to the SEI layer, the CEI layer has yet not received substantial research attention, and its effect on the battery performance is, therefore, not well understood [5].

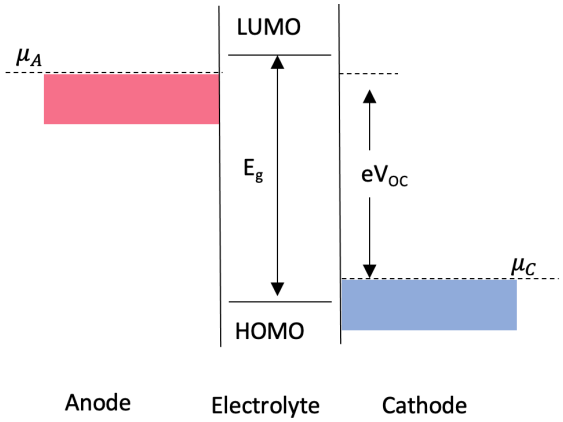


Figure 2.3: Energy diagram presenting the electrochemical window (Eg) of an electrolyte, HOMO and LUMO of the electrolyte and its relative relationship with the cathode ($\mu_C$) and anode ($\mu_A$) potentials. Figure based on Liu et al.[29].

### 2.4.1 Electrolyte components

As mentioned, conventional electrolytes typically consist of conducting salts, non-aqueous solvents, and additives [5].

The primary role of the solvent is to dissolve the salt and provide efficient transportation of $Li^+$ ions. To achieve this, the solvent should possess a high dielectric permittivity to ensure complete solvation of ions and low viscosity for unimpeded transport of ions. In addition, it should be electrochemically inert in all operating conditions and have a high boiling and low melting point to preserve a large liquid range. For a nonaqueous solvent to dissolve lithium salts, it must contain polar groups, and the main family for such solvents is organic esters and ethers. Despite the ether's moderate dielectric constants and low viscosity, they are quite oxidative towards the cathode and generally show poor cycling stability. Esters have proven to show better cycling stability than ethers. Depending on if the esters are cyclic or acyclic, they have a high dielectric permittivity and high viscosity or low dielectric permittivity and low viscosity, respectively. The solvent can thus be balanced by combining cyclic and acyclic esters. Such a combination is the blend of cyclic ethylene carbonate (EC) and acyclic Dimethyl carbonate (DMC) and/or acyclic diethyl carbonate (DEC). Figure 2.4 presents the chemical composition of these compounds [27]. In addition, the high melting temperature of EC ($\sim$ 36 °C) is also balanced by the lower melting temperature of DMC ($\sim$ 4.6 °C) and/or DEC ($\sim$ -73.3 °C). Lastly, the EC is stable towards oxidation on the cathode and it effectively reduces on the anode to form a stable SEI layer [30, 5].

The main function of the lithium salts used in LIBs is to ensure $Li^+$ transport between the electrodes. A requisite property of the salt is that it should be able to dissolve completely in the solvent, and the solvated ions, particularly $Li^+$, should exhibit high mobility in the solvent. Additionally, the anion should possess high electrochemical stability, particularly concerning its ability to withstand oxidation at the cathode, plus chemical stability towards the solvent. Most lithium salts with sufficient solubility are based on complex anions consisting of a simple anion stabilized by a lewis acid. Among several researched salts, the $LiPF_6$ ($F^-$ complexed with $PF_5$) salt has since the beginning of the 1990's, been the indispensable electrolyte salt used in almost all commercialized LiBs. This owes to its well-balanced combination of high ionic mobility and dissociation constant. In addition, at potentials above 3 V, it passivates the Al current collector, thus reducing the risk of corrosion. In standard battery solvents (e.g., EC, DEC, DMC), the $LiPF_6$ is electrochemically and thermally stable up to approximately 4.8 V and 70 °C, respectively. However, the P-F compound is susceptible to hydrolysis and reacts with only a trace amount of

water present to form HF. How this impacts the battery performance of LNMO-based cells, which is the battery type used in this thesis, will be further elaborated on in Section 2.5 [30, 5].

Rather than replacing the main constituents of the electrolyte system, specific targeted functions can be modified by introducing an additive at very small concentrations. In this way, the bulk properties of the electrolyte can be maintained in an effective and cost-effective manner. Dependent on the function targeted, different additives are typically employed to (1) enhance the ion conduction of the bulk electrolyte; (2) modify the electrolyte-electrode interface chemistry; and (3) prevent overcharging of the cells (flame retardants). Additives are often regarded as sacrificial constituents, as they are usually consumed during operation. As mentioned in the Section above, the emphasis of the research on the electrolyte-electrode interphase has been directed toward the SEI layer. Similarly, efforts aimed at identifying appropriate additives have focused on finding additives with high reduction potentials to ensure that these are reduced on the anode before the bulk electrolyte is engaged. Examples of such additives are fluoroethylene carbonate (FEC) and vinylene carbonate (VC). It is worth noting, that for additives of commercial interest, little work has been published in technical journals [30, 5].

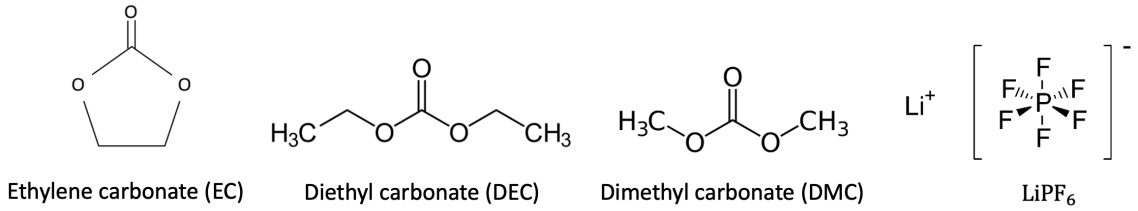


Figure 2.4: The chemical structure of common electrolyte components. Figures inspired by Xu et al. [30].

## 2.5 Failure of LMNO-based cells

The energy density of a battery can be enhanced by increasing the operating voltage, as seen from Equation 2.10. However, with the high operating voltage of LNMO (above 4.3 V) the stability of conventional carbonate-based electrolytes is an issue. Additionally, in an electrode cast, the LNMO particles are not only in contact with the electrolyte but also interact with binders (e.g., PVDF), conductive agents (e.g., CB), and the Al current collector. Any deterioration of these constituents may result in loss of active LNMO or increased impedance. Factors causing loss of available LNMO could be electrode delamination, loss of electronic contact due to particle cracking, ionic contact loss due to pore-clogging, or degradation of the LNMO particle itself. It should, however, be mentioned that these are not only issues concerning the LNMO cathode material exclusively [10].

Given that the LNMO electrode is well-optimized, it has relatively good structural integrity due to a moderate volume expansion (approximately 7%) during (de)lithiation. The anodic stability of binders like PVDF has also been regarded as sufficient. At high potentials, side reactions and some dissolution have been reported for conductive agents like CB and the Al current collector, respectively. These factors are, however, not considered the main causes of the LNMO cell's rapid performance decay. In literature, there is a commonly accepted view that failure is primarily attributed to undesired electrolyte oxidation and dissolution of TMs.

### 2.5.1 Transition metal dissolution

As mentioned in Section 2.3.1, $Mn^{3+}$ may be present on the LNMO particle surface from synthesis. The $Mn^{3+}$ tends to disproportionate to form $Mn^{2+}$ via Reaction 2.12, and when in contact with the electrolyte, results in the dissolution of $Mn^{2+}$ into the electrolyte.

$$2\,Mn^{3+} \longrightarrow Mn^{4+} + Mn^{2+} \tag{2.12}$$

Furthermore, during cycling, an $Mn_3O_4$-like phase tends to form in the vicinity of the surface. This $Mn_3O_4$-like phase contains both $Mn^{3+}$ and $Mn^{2+}$, which are soluble in the electrolyte, thereby causing additional Mn dissolution. Acid attacks by HF (see following section) can accelerate the dissolution of TMs, then including Ni, and further reduce the structural integrity of the LNMO

structure. Additionally, it has been observed that dissolved TMs will migrate toward the graphite anode (cross-talk) and deposit, causing damage to the protective SEI layer. In the damaged areas where the anode is exposed to the electrolyte, cyclable Li will be consumed upon the formation of a new SEI layer. This is especially an issue in full cells with a finite amount of cyclable Li. In a study by Pieczonka et al. [31], they reported an increased amount of TM dissolution with an increased state of charge (SOC), temperature, and storage time. All of these unfortunate effects hasten the battery performance degradation [10, 31].

### 2.5.2 Electrolyte oxidation

At the high operating voltage of LNMO, many electrolyte components are unstable. For example, if the voltage exceeds 4.3 V, EC may be electropolymerized to form a poly(ethylene carbonate) (PEC) film on the electrode surface. Additionally, the precence of $PF_5$ originating from $LiPF_6$ (see Equation 2.13) could catalyze the ring-opening of EC, followed by its polymerization into poly(ethylene oxide) (PEO)-like products. Furthermore, if the electrolyte contains only a small amount of water, HF could be generated via the following reactions [31]:

$$LiPF_6 \longleftrightarrow LiF + PF_5 \tag{2.13}$$

$$PF_5 + H_2O \longrightarrow OPF_3 + 2\,HF \tag{2.14}$$

$$OPF_3 + 3\,H_2O \longleftrightarrow PO_4H_3 + 3\,HF \tag{2.15}$$

Moreover, protic impurities, such as alcohols, may be present in carbonate-based electrolytes and lead to the production of more HF. This process is accelerated by higher temperatures and water impurities. The specific alcohol formed depends on the composition of the electrolyte, where methanol may be formed from DMC, ethanol from DEC, and ethylene glycol from EC [31]. According to Pieczonka et al. [31], Mn oxides may act as a catalyst for the decarboxylation [1] of DEC, leading to the production of ethanol (EtOH), followed by the formation of diethyl ether ($Et_2O$) and water:

$$DEC \longrightarrow EtOH + CO_2 + C_2H_4 \tag{2.16}$$

$$EtOH \longrightarrow Et_2O + H_2O \tag{2.17}$$

The water produced will react with $LiPF_6$, and generate additional HF. Multiple reaction mechanisms have been proposed for the decomposition of DEC. Another alternative, which may occur simultaneously with Equation 2.16 and 2.17 is the attack of $PF_5$ on the carbonyl oxygen in DEC, followed by the generation of HF [31]:

$$DEC + PF_5 \longrightarrow C_2H_5OCOOPF_4 + C_2H_4 + HF \tag{2.18}$$

$$C_2H_5OCOOPF_4 \longrightarrow PF_3 + CO_2 + C_2H_4 + HF \tag{2.19}$$

As already mentioned, the additional HF generated from electrolyte decomposition will accelerate the dissolution of TMs, causing further deterioration of the LNMO structure. In addition, the gaseous products generated ($CO_2$ and $C_2H_4$), could cause cell swelling, which poses a severe safety concern. Other reaction products observed on the LNMO surface due to electrolyte decomposition and Mn and Ni dissolution are LiF, $MnF_2$, and $NiF_2$ [10, 31].

As discussed above, the main challenge faced by LNMO-based cells is undesired reactions between the electrode and electrolyte, which is further aggravated at high operating voltages. These unfortunate outcomes limit the battery's longevity and must be resolved before LNMO-based cells can be viably introduced into the commercial market.

## 2.6 Strategies to stabilize the LNMO-electrolyte interphase

Numerous approaches have been proposed to enhance the stability of the LNMO-electrolyte interface. The most effective solution would be a novel electrolyte system that exhibits high anodic stability at high voltages. Ionic liquids are such an alternative. However, the many difficulties encountered during synthesis and their high cost present a significant barrier to their practical

[1] A chemical reaction in which a carboxyl group is removed and $CO_2$ is liberated.

application at large scale [32]. Another option is a passivating surface coating with either inorganic or organic materials. The primary purpose of such a coating is to establish a physical barrier between the electrode and electrolyte, which also prevents the dissolution of TMs into the electrolyte. To ensure sufficient transport of $Li^+$ and charge transfer, the surface coatings should be $Li^+$ conductive, electrically conductive, uniform, and thin. Additionally, the coating process and the coating itself should not damage the cathode materials' crystal structure [33, 34].

In the past, the surface of LNMO has been coated with various inorganic materials, such as $Al_2O_3$, MnO, ZnO, $ZrO_2$, $SiO_2$, $FePO_4$, and $LiFePO_4$. These coatings have effectively mitigated electrolyte decomposition; however, they still encounter issues related to poor electrical conductivity, leading to poor rate performance. Moreover, it has been proven challenging to create a uniform coating layer [35, 11, 10, 34].

As presented in the introduction, coating with a functional polymer that exhibits high ionic and moderate electronic conductivity could be a promising approach. In addition, due to their flexible nature, they could handle volume changes during cycling better than inorganic materials. Kim et al. [36] conducted a study where LNMO was coated with polyimide using thermal polymerization. Despite the unfavorable interfacial reaction being suppressed, poor compatibility with the electrolyte was observed at elevated temperatures (55 °C). In addition, polyamide has a poor electrical conductivity [37]. Promising results, especially at elevated temperatures, from coating LNMO with other functional polymers, such as polyaniline, polythiophene, and polyacrylonitrile, have been reported [38, 35]. From coating LNMO with polyaniline via oxidative chemical polymerization, Dong et al. [38] reported a capacity of 123 mAh/g with a capacity retention of 99.7% at 0.5C after 200 cycles in the voltage range 3.0 to 4.95V at room temperature. They also reported suppressed undesirable interfacial reactions. In addition, at elevated temperatures (55 °C), the polyaniline-LNMO exhibited better cycling stability than the pristine LNMO. However, as with inorganic materials, achieving an entirely uniform coating with functional polymers remains challenging.

Despite these promising results, it is still worthwhile to explore other functional polymers that can stabilize the LNMO-electrolyte interface. To the author's knowledge, only one previous research by Gao et al. [12] has investigated the possibility of using the functional polymer polypyrrole (PPy) as a coating material for the LNMO electrode.

## 2.7 Polypyrrole as a cathode coating

PPy is polymerized from the heterocyclic aromatic monomer pyrrole (Py) ($C_4H_4NH$). The Py structure is presented in Figure 2.5 step a. The term "heterocyclic" refers to the presence of elements other than carbon and hydrogen in the ring structure of the compound; in the case of Py, this is nitrogen. The nitrogen and carbon atoms are $sp^2$ hybridized and form $\sigma$- bonds with the hydrogen atoms through axial overlapping. The unhybridized orbitals on the carbon contribute with four $\pi$-electrons from its two double bonds, and the nitrogen with two $\pi$-electrons from its lone pair. This gives Py a total of six delocalized $\pi$-electrons in resonance. Combined with Py's planar and cyclic structure, this gives it its aromatic character [39].

The Py monomer is readily oxidized to form PPy via chemical or electrochemical polymerization. It is also commercially available at large scale [13]. As a cathode coating, PPy can function as a medium for hosting the insertion and extraction of the $Li^+$ within the potential range 2.0 V to 4.5 V, providing a theoretical capacity of about 72 mAh/g [40, 41]. Due to PPy's contribution to the specific capacity, a high PPy content could reduce the specific capacity of the cathode composite material. Therefore, aiming for a thin coating in the nanoscale is preferable. The electrical conductivity of PPy, ranging from $10^{-3}$ S/cm to 100 S/cm, largely depends on the nature of the dopant [41]. The doping mechanism is further explained in Section 2.7.1. The PPy has a comparable electrical conductivity to CB, which ranges from 0.1 to 100 S/cm [42]. Hence, a PPy coating could potentially suppress the demand for inactive CB additive in the electrode cast [41].

In a recent review by Chavan et al.[43], a variety of PPy-coated cathode materials were evaluated for their suitability in different battery applications. According to the authors, as of October 2022, most studies have focused on cathode materials for lithium-sulfur batteries. However, the review highlights that incorporating PPy-coating generally enhances the cathode materials' structural stability, electrical conductivity, and electrochemical performance. Similar improved properties were also demonstrated by Gao et al.[12] for an LNMO-PPy composite synthesized via a chemical-

oxidative polymerization process in an aqueous solution, where p-toluenesulfonyl sodium was used as dopant and ferric chloride as an oxidant. The particle size of the synthesized LNMO particles ranged from 200 to 500 nm. In half coin cells, the LNMO-PPy composite was cycled in a 1M $LiPF_6$, EC:DEC (3:7 ratio) electrolyte system at 1C (1C = 140 mAh/g). The cells were cycled between 3.5 and 4.9V. The pristine LNMO cells initially displayed a discharge capacity of 116 mAh/g and retained 76.7% of the capacity after 300 cycles. The LNMO-PPy composite, with a 3 nm thick PPy-coating, achieved a slightly lower initial discharge capacity of 112.9 mAh/g. However, the capacity retention increased to 91 % after 300 cycles. During the first five cycles, the discharge capacity generally increased. Gao and co-workers [12] attributed this increase to the electrolyte wetting of the polymer, which provided an increased supply of anions for improved doping of the coating. The improved electrochemical performance was ascribed to the high conductivity of the PPy-coating. The cells were also cycled at elevated temperatures (55 °C) to increase the HF concentration in the cell, hence accelerating the TM dissolution. Upon the first cycle, a polarization gap was observed for the pristine LNMO, but not for the LNMO-PPy composite, suggesting that the PPy-coating effectively prevented the electrolyte decomposition. However, an increased polarization gap during the first cycle was observed for PPy layers thicker than 3 nm. According to the authors, this was most likely caused by loss of contact between the electrode and the electrolyte. In contrast to the cells containing pristine LNMO, no Mn or Ni was detected on the counter electrode post-mortem cycling for the LNMO-PPy cell, indicating that the PPy layer prevented the dissolution of Mn and Ni. Lastly, an electrochemical impedance spectroscopy (EIS) test done after 300 cycles showed that the charge transfer resistance had decreased from 125 Ω to 73 Ω for the pristine LNMO and LNMO-PPy composite after 300 cycles at room temperature, respectively. This demonstrated that a PPy-coating increased electron transport and improved the electrochemical performance.

Although only one study has investigated PPy as a cathode coating for LNMO electrodes, PPy has been explored as a cathode coating for LMO and LFP cathodes in LIBs. As mentioned in Section 2.3, the spinel structure of LMO has the same issues related Mn dissolution as LNMO. T.Wang et al.[37] synthesized an LMO-PPy composite with a 3 nm thick PPy-layer using a similar synthesis procedure as Gao's group, except that they used ethanol as a solvent, not water. From cycling coin half-cells in a 1 M $LiPF_6$, EC:DMC (1:1 ratio) electrolyte system between 3.0 and 4.3 V at 0.5C, they achieved an initial discharge capacity of 113 mAh/g for the pristine LMO and 123 mAh/g for the LMO-PPy composite, respectively. The increased capacity was attributed to the charges stored in the double layer at the oxidized PPy surfaces making PPy involved in the discharge. After 50 cycles, the LMO-PPy had a capacity retention of 90 %, whereas the pristine LMO had only achieved a capacity retention of 68 %. From an EIS analysis after 30 cycles, the charge transfer resistance of the pristine LMO and the LMO-PPy cell was 750 Ω and 189 Ω, respectively. This demonstrated that the electronic conductivity of the PPy coating had improved the charge transfer through the electrode surface. Despite the authors not investigating if Mn had been deposited on the counter electrode after cycling, the improved cycling performance indicated that the PPy-layer suppressed unfavorable electrode-electrolyte reactions.

In the cases where PPy has been used as a coating material for the LFP cathode, the main goal has been to improve its electrical conductivity and not to stabilize the electrode-electrolyte interface as for the LNMO and LMO electrodes. Using a similar synthesis procedure to both T.Wang's and Gao's groups, G.X Wang et al.[44] synthesized an LFP-PPy composite. Cycling coin half cells between 2.75 and 4.3 V, in a 1 M $LiPF_6$, EC:DMC (1:1 ratio) electrolyte system against a Li-metal counter electrode, they achieved an initial discharge capacity of 112 mAh/g and 130 mAh/g for the pristine LFP and LFP-PPy composite, respectively. Despite PPy having a lower theoretical capacity than LFP, they achieved an increased capacity, which is the opposite of what is theoretically expected. From an EIS analysis, as for both the LNMO-PPy and the LMO-PPy electrodes, the LFP-PPy electrode had a significantly lower charge transfer resistance (75 Ω) than the pristine LMO (840 Ω). The improved initial discharge capacity was therefore ascribed to the electrical conductivity leading to better utilization of the LFP active material.

In a review by Zhu et al.[45], various strategies for stabilizing high-voltage cathode materials for LIBs were examined. They concluded that using electrolyte additives to form in-situ self-formed films on the cathode surface during the initial charge/discharge cycles could be one of the most efficient ways to improve cycling stability. Furthermore, they noted that this approach is also the easiest to implement for large-scale industrial production. The above-presented research coated the cathode materials using a chemical-oxidative polymerization process before cell manufacture. Another option could be to use Py as an electrolyte additive and electropolymerize it onto the

LNMO electrode during the battery's initial charge cycle. As stability issues concerning the CB additive at high operating voltages have been reported, the proposed coating approach could provide an added advantage by coating the entire electrode surface, including the CB particles.

### 2.7.1 Electropolymerization of pyrrole

The formation of PPy from Py is done via anodic oxidation of Py in the presence of an electrolyte solution. Since the voltage is high near the electrode-electrolyte interface, the reaction predominantly takes place there, leading to the deposition of a PPy film on the electrode surface [13]. To ensure that the protective PPy-layer is formed before the electrolyte decomposes, the oxidation potential of Py must be lower than the decomposition potential of the electrolyte. The oxidation potential of Py is about 3.7 V (vs. $Li/Li^+$), while the oxidation potential of a conventional electrolyte is about 4.3 V (vs. $Li/Li^+$) [10]. Electropolymerization can be achieved through various electrochemical techniques, including galvanostatic (constant current) and potentiodynamic (constant potentials, i.e., cyclic voltammetry). Further elaboration on these techniques is provided in Section 2.9 [13].

A critical aspect in achieving a comprehensive understanding and control over the intrinsic properties of the PPy-film is to understand the underlying mechanism and sequential steps involved in the electropolymerization reaction. Several mechanisms have been proposed; however, only one has been universally accepted. The initiation step is the primary discussion area among the proposed mechanisms, as each suggests different ways of starting the reaction. Thus far, the Diaz mechanism, with the reaction steps presented in Figure 2.5, has been the most commonly cited mechanism in literature. Upon applying a positive potential, the Py monomer migrates toward the electrode surface where it undergoes oxidation and a cation radical is generated (*step a*). The concentration of Py cation radicals will be higher near the electrode surface because charge transfer is faster than the supply of Py monomers from the bulk solution. Next, the cation radicals will undergo a dimerization reaction, forming a dihydromer dication upon reacting with other cation radicals (*step b*). The dihydromer dication is now deprotonated to form a stable aromatic dimer, a polymer with few repetitive units (*step c*). The process of polymer chain propagation occurs via the same oxidation, coupling, and deprotonation steps as described. The aromatic dimer is oxidized to form a dication radical (*step d*), which reacts with a cation radical to produce a trimer dication (*step e*) to finally form a stable aromatic trimer through deprotonation (*step f*).

The resulting polymer has a positive charge every 3 to 4 units. Hence, anionic species are concurrently incorporated into the polymer during polymerization to maintain charge neutrality, as illustrated in Figure 2.6. In a LIB, the doping anion is $LiPF_6{}^-$ originating from the $LiPF_6$ salt. The polymer typically consists of approximately 35 wt% anions and 65 wt% polymers. Its inherent electrical conductivity arises from its extended conjugated system, composed of double and single bonds with unhybridized orbitals along the polymer chain. These delocalized electrons (from the unhybridized orbitals) are free to move or roam across the chain, thus giving rise to PPy's electrical conductivity [44, 13].

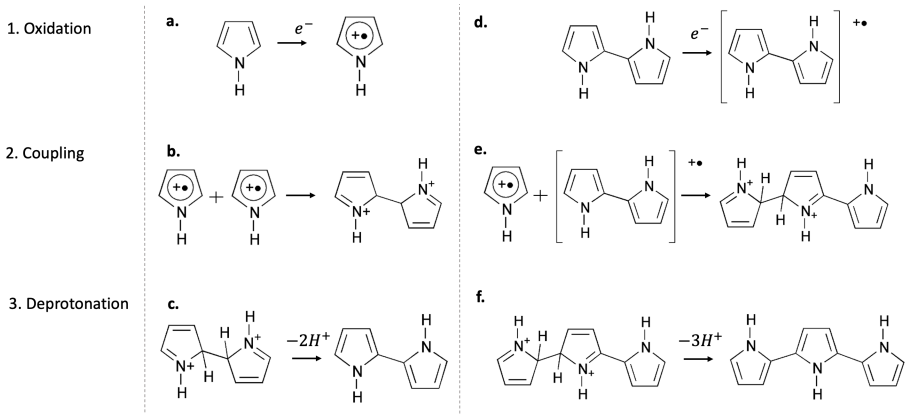


Figure 2.5: A stepwise illustration of the electropolymerization process Py via the Diaz mechanism. The figure is inspired by Sadki et al. [13] and reused from the Specialization project.

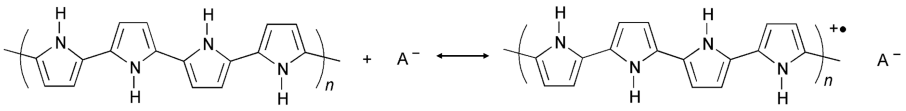

Figure 2.6: Illustration of the aniondoping of polypyrrole. The figure is inspired by Sadki et al. [13] and reused from the Specialization project.

The formed PPy layer is electrochemically active during charging and discharging of the battery, and thus, it contributes to the electrode's specific capacity. Upon charging, the PPy is oxidized, and a $PF_6{}^-$ anion from the electrolyte solution intercalates the PPy chain to ensure charge balance [44]. This process can be described according to the following reaction [41]:

$$\mathrm{PPy} + \mathrm{xPF_6{}^-} \longleftrightarrow [(\mathrm{PPy})^{x+}\,(\mathrm{PF_6{}^-})_x] + \mathrm{xe^-} \tag{2.20}$$

During discharging, the PPy is reduced, and the $PF_6{}^-$ anion de-intercalates from the PPy chain. The $PF_6{}^-$ anion enters the electrolyte and, to maintain charge neutrality, $Li^+$ intercalates the PPy [44]. The process can be described by the following reaction [41]:

$$[(\mathrm{PPy})(\mathrm{PF_6{}^-})_x(\mathrm{Li^+})_x] \longleftrightarrow [(\mathrm{PPy})^{x+}\,(\mathrm{PF_6{}^-})_x] + \mathrm{xLi^+} + \mathrm{xe^-} \tag{2.21}$$

When charged and discharged, conducting polymers do tend to deteriorate. Krische et al. [46] suggested that the primary reason for this degradation is the overoxidation of the polymers, as the oxidation of the Py monomers occurs at a higher potential than the redox process of the polymer.

### 2.7.2 Factors affecting the properties of the polypyrrole film

The properties of the PPy film are strongly dependent on the type of dopant, solvent, and applied potential [13].

The roughness of the PPy-surface usually increases as the thickness of the PPy layer increases. When the thickness exceeds 1000 nm, for chloride and perchloride doped films the morphology of the layer typically displays a 'cauliflower-like' structure, whereas, for thicknesses below 1000 nm, it commonly appears with a globular shape. The microstructure and porosity of the polymer are influenced by the size of the anion, which affects the polymer's ability to facilitate the diffusion of dopants during the redox process. In other words, larger anions tend to result in a more permeable structure that enables easier dopant diffusion [13]. The basicity of the anion affects the conductivity of the polymer; the higher the basicity, the lower the conductivity due to increased interaction between the positive charge of the polymer and anions. Hence, anion acidity leads to increased conductivity in PPy [13]. The $PF_6{}^-$ anion is a non-coordinating anion, meaning that it exhibits weak reactivity with cations, which is preferable in the context of improved conductivity of the PPy polymer.

Aprotic solvents have been found to be the most effective solvents for the electropolymerization of Py. All the solvents commonly used in LiBs, namely EC, DEC, and DMC, are aprotic solvents. The presence of water could lead to an attack by water molecules during the electropolymerization reaction, resulting in an uneven PPy structure and decreased functional properties. Moreover, the occurrence of surface defects in the PPy polymer has been linked to the generation of oxygen during the process of water oxidation [13].

Although the monomer oxidation potential remains unaffected by pH, the reactivity and stability of the resulting PPy at the electrode can be influenced by it. As mentioned in Section 2.7.1 the polymer chain is protonated during the electropolymerization process of Py acidic solutions. This results in improved electronic conductivity of the polymer. Conversely, the opposite is observed in basic solutions. The polymer chain is deprotonated, leading to decreased electronic conductivity. However, at very a very low pH, partly conjugated PPy with poor conductivity may form [13]. The pH could also influence the electrochemical activity of the polymer, where the insertion and extraction of the dopant are promoted in acid solutions. In a basic solution, the anion may be replaced by hydroxyl group from the solution [13]. The tendency of acidic solutions to promote polymerization raises the possibility of consuming unfavorable HF during the initial charge and discharge cycles of a LIB during the electropolymerization process of Py.

Typically, PPy films formed at low temperatures (-20 °C) have a more regular structure, hence a higher conductivity than the films formed at higher temperatures (20 °C). However, higher

temperatures have been shown to form a better adhesion to the electrode where the PPy is being deposited. By optimizing the polymerization potential and temperature, good films could still be prepared at higher temperatures [13].

## 2.8 Carbon as a cathode coating

Considerable research has been conducted on the application of carbon-coated cathode materials in LiBs, with the aim to enhance electron transport across the cathode interface and, consequently, achieve improved electrochemical performances [9, 47, 3, 48].

Carbon-based materials offer several advantages that make them highly suitable for various cathode coatings. They exhibit good electrochemical stability, owing to their inherent resistance to oxidation and great tolerance to acidic electrolytes, which in turn results in high resistance towards corrosion. Additionally, carbon-based materials display excellent electrical conductivity and have a large surface area, strong heat resistance, and high structural integrity, all of which promote the performance of LiBs. Moreover, sources of carbon are abundant, inexpensive, and their fabrication is relatively simple [48]. The lightweight nature and compatibility of carbon compounds further enhance the utilization of electrode space in LiBs [49]. As discussed in Section 2.6, which holds true for carbon coatings as well, is that they can mitigate unfavorable reactions between the cathode and electrolyte and could potentially suppress TM dissolution [48]. Carbon compounds exist in various structures, such as graphene, graphite, graphene oxide, reduced graphene oxide, carbon nanotubes, and carbon black, each with distinct physical and chemical properties, offering a broad spectrum of possibilities for electrode stabilization [49, 48, 50]. Carbon black has an amorphous structure with graphitic-like domains, where the graphite domains consist of carbon atoms arranged in hexagonal planes. If the LIB is operating at working potentials  4.5 V vs. $Li/Li^+$, there is a risk of anion intercalation into these graphitic domains at the cathode, which could degrade the carbon black [51].

Due to the low electronic conductivity of LFP, numerous studies have investigated the impact of various carbon coatings on the electrochemical properties of LFP [52, 53, 36, 54, 55, 56, 57, 58]. The results consistently demonstrate substantial enhancements, which can be attributed to the increased electronic conductivity provided by these coatings, and improved contact between the carbon-coated LFP particles and the current collector. The higher electronic conductivity facilitates improved utilization of the active materials, leading to better electrochemical performance. The studies also demonstrate that too thick coatings may obstruct the transport of $Li^+$ ions. Typically a coating thickness ranging from 1 to 10 nm is sufficient to ensure stable $Li^+$ transport across the coating and electrode interface [49].

While the majority of studies have focused on carbon coatings for LFP electrodes, researchers have also started to explore the use of various coating methods and carbon materials for LNMO electrodes, see Table 2.2. For instance, Yang et al. [14] used a wet chemical method involving sucrose carbonization to coat LNMO particles with a carbon layer of 20 nm thickness. The researchers tested half-coin cells by cycling them between 3.0 and 4.9 V in a 1 M $LiPF_6$, EC:DMC (1:1) electrolyte system. Results showed that the bare LNMO and C/LNMO cell exhibited a relatively similar initial discharge capacity of 128 and 131 mAh/g at 0.2 C, respectively. However, after 100 cycles at 0.2C, the C/LNMO cells achieved capacity retention of 92 % while the bare LNMO cells experienced a rapid capacity fade after only 70 cycles until the capacity faded completely after 100 cycles. Moreover, the C/LNMO cells had a significantly better rate capability, with a capacity of 114 mAh/g at 5C, which was almost double that of the bare LNMO.

Zhang et al. [15] achieved comparable results to Yang et al. [14] using a similar cell configuration, but instead of sucrose carbonization, they used carbon black as the coating material with a coating thickness of 70 nm. The bare LNMO and the C/LNMO had the same initial discharge capacity of about 125 mAh/g at 0.2 C. Despite having a non-uniform carbon coating, the C/LNMO cells exhibited a capacity retention of 94% after 100 cycles at 1C, which was significantly better than the 84% capacity retention of the bare LNMO cells. In addition, the C/LNMO cells in Zhang et al.'s study demonstrated better rate capability than the bare LNMO cells. At 5C, the C/LNMO cells had a capacity of 111 mAh/g, while the bare LNMO cells had a much lower capacity of only 70 mAh/g.

Carbon nanotubes have also been applied to coat the LNMO cathode material. With a mechanofusion technique, Hwang et al. [19] coated the LNMO particles with oxidized carbon nanotubes

with a coating thickness between 10-15 nm. Similarly to both Yang et al.[14] and Zhang et al.[15], the initial discharge capacity was the same for the bare LNMO and the C/LNMO. However, they achieved a significantly higher initial discharge capacity of 137 mAh/g at 0.1C compared to Yang et al.[14] and Zhang et al.[15]. After 80 cycles at 1C, the C/LNMO sample exhibited a capacity retention of 95.5%, while the pristine LNMO retained only around 85% of its initial capacity. At higher C-rates, the C/LNMO exhibited discharge capacities of about 130 at 4C and 93 mAh/g at 8C. In comparison, the bare LNMO delivered a discharge capacity of only 109 and 70 at the same C-rates.

Ku et al. [59] carbon-coated LNMO particles by applying an Atmospheric microwave plasma torch where they used acetylene gas as the carbon source. The resulting carbon coating had an average thickness of about 10 nm. Using a similar cell configuration as the abovementioned research, they achieved an initial discharge capacity of around 120 mAh/g at 0.5 C for both the bare LNMO and the C/LNMO cells. However, after 100 cycles at 0.5 C, the C/LNMO cells showed significantly higher capacity retention of 96 % compared to the bare LNMO, which only retained 28 % of its capacity. At elevated temperatures (50 °C), the C/LNMO also displayed a better rate capability than the bare LNMO. When they increased the C-rate from 0.1 to 10 C, the capacity of the C/LNMO dropped from 124-104 mAh/g, while the bare LNMO dropped from 123-0.15 mAh/g.

It is important to note that in the literature, there are differences in the specific capacities reported for the bare LNMO and the C/LNMO, which could be due to various active material loadings and variations in the quality of the LNMO powder used. However, a consistent observation across all the studies is that the initial discharge capacity of the C/LNMO and bare LNMO cells is similar, indicating that the carbon coating is electrochemically inactive and does not contribute to the capacity [14, 15, 19, 59]. Furthermore, all C/LNMO cells showed improved capacity retention after prolonged cycling and improved rate capability at higher C-rates than the bare LNMO cells. The improved electrochemical properties of the C/LNMO cells was ascribed to the improved electronic conductivity. From EIS measurements after 50 cycles with a charging rate of 0.2 C and discharge rate of 1C, Yang et al. [14] had a surface resistance (Rs) of 198 Ω and 59 Ω for the bare LNMO and C/LNMO, respectively. The charge transfer resistance (Rct) for the bare LNMO was 199 Ω, while it was only 19 Ω for the C/LNMO. From similar EIS measurements after 100 cycles at 0.2C charge rate and 1C discharge rate, Zhang et al. [15] found the Rs of the bare LNMO to be 120 Ω, while it was only 47 Ω for the C/LNMO. The Rct for the C/LNMO of 55.4 Ω was also significantly lower than the bare LNMO with an Rct of 114 Ω. According to Zhang et al. [15] and Yang et al. [14], the reduced Rs observed in the C/LNMO cell compared to the pristine LNMO, is likely due to suppression of surface resistance caused by side reactions between the electrolyte and LNMO electrode. Furthermore, since the charge transfer kinetics of the electrode materials are known to be inversely proportional to surface resistance, they proposed that the reduction in Rct observed in the C/LNMO could be attributed to the suppression of Rs, as well as the enhanced electronic conductivity. This improvement in electronic conductivity allowed for better utilization of the active material's capacity at higher discharge rates [15]. As a result, the significant enhancements in cycling stability and rate capability were ascribed to both the suppression of surface resistance and the enhanced electronic conductivity, including the carbon coating protective effect against the dissolution of TMs [14, 15, 19, 59]. As for the specific capacity, the differences in impedance reported in the literature could be due to various active material loading used.

Table 2.2: Electrochemical performance of LNMO electrodes coated with different carbon types and coating methods.

| Carbon coating material | Coding method | Initial discharge capacity | Rate capability | Ref. | Year of publication |
|---|---|---|---|---|---|
| Carbonization of sucrose | Wet chemical | 131 mAh/g at 0.2C | 92% after 100 cycles at 0.2C | [14] | 2010 |
| Carbon black | Wet chemical | 125 mAh/g at 0.2C | 94% after 100 cycles at 1C | [15] | 2010 |
| Graphene oxide | Wet chemical | 115 mAh/g at 0.5C | 71% after 1000 cycles at 0.5C | [16] | 2013 |
| Reduced graphene oxide | Wet chemical | 120 mAh/g at 0.3C | 83 % after 100 cycles at 1C | [17] | 2014 |
| Carbon nanotube | Mechano-fusion | 137 mAh/g at 0.1C | 47.2% after 80 cycles at 1C | [19] | 2016 |
| Oxidized carbon nanotube | Mechano-fusion | 137 mAh/g at 0.1C | 95.5% after 80 cycles at 1C | [19] | 2016 |
| Acetylene | Atmospheric microwave plasma torch | 120 mAh/g at 0.5C | 96% after 100 cycles at 0.5C | [59] | 2018 |
| Reduced graphene oxide | Wet chemical | 127 mAh/g at 0.1C | 93 % after 100 cycles at 1C | [18] | 2019 |

### 2.8.1 Carbon coating by a CVD process

As previously discussed, several methods exist to create a carbon layer. One of the most common techniques for producing a uniform thin film coating is the chemical vapor deposition (CVD) technique. This technique involves exposing the host material, i.e., the material to be coated, to volatile precursors. The precursors then react or decompose to form a thin film on the host material. This way, larger particles can be coated with nanoscale particles [48].

Yu et al. [60] successfully carbon-coated silicon nanoparticles using a rotational CVD carbon coating machine. To achieve this, the temperature was first raised from room temperature to 300 °C in a pure argon atmosphere, with a heating rate of 15 °C/min. Following this, an acetylene precursor gas ($C_2H_2$) plus argon was introduced. The temperature was then increased to 800 °C where it was held for 1.5 h. Finally, the oven was gradually cooled down. This process resulted in carbon-coated Si particles with a uniform coating thickness of about 15 nm, where the coating had an amorphous carbon structure.

As demonstrated by Ku et.al [59], using acetylene as a carbon source to coat LNMO particles via the atmospheric microwave plasma torch method, resulted in enhanced cycling stability and rate capability compared to bare LNMO. Acetylene is also readily available in the market and cost-effective [59]. Hence, using the CVD method with acetylene as the carbon source may present a promising strategy for the carbon coating of LNMO particles.

### 2.8.2 Carbon Black coating via the application of a hybridizer machine

As demonstrated by Zhang et al. [15], CB-coated LNMO cathodes could deliver both an improved rate capability and cycling stability compared to bare LNMO cathodes. In addition, CB is readily available and is already used as an electrode additive to improve the electrical conductivity of the cathode. By utilizing CB as a coating material for the LNMO cathode, it may be possible to decrease the quantity of CB additive needed for the cathode cast. However, it's worth noting that the coating obtained through the wet-chemical method used by Zhang and colleagues was not entirely uniform. Additionally, such a coating method typically requires complex synthesis processes and involves solvents and binders, which will be cost-ineffective for commercial-scale production [61]. Another option is dry-coating, and unlike wet-coating, this process does not require additional binders or solvents. Moreover, there is no need for any energy-intensive drying steps for the particulate products obtained through this method. [62]. As demonstrated by Hwang et al. [19] using the dry-coating mechano-fusion technique where the LNMO particles were coated with oxidized carbon nanotubes, they achieved a relatively uniform coating and improved rate capability and cycling stability. Thus, employing a dry-coating method with CB as the coating material is a promising approach to obtaining uniform and cost-effective carbon-coated LNMO particles [61].

In a dry coating process, through the application of mechanical forces, submicron-sized guest particles are coated onto micron-sized host particles, as illustrated in Figure 2.7. Due to the small size of the guest particles, Van der Wals forces are sufficiently strong to adhere to the host particles,

meaning that the adhesion force is greater than the weight of the smaller particles. Depending on the operating conditions, such as weight fractions and processing time, the guest particles could form a discrete or continuous coating. The continuous coating may comprise a porous (monolayer or multilayer) or a non-porous film. It is easier to create a continuous layer with a narrow size distribution of the host particles. If the particles are very cohesive, they tend to form agglomerates, which requires mixing to break them apart. Also, to prevent segregation of the host and guest particles, their size should differ by more than one or two orders of magnitude. Thus, the dry coating process can be divided into three stages: (1) deagglomeration of the primary particles into their primary particle, (2) attachment of the guest particles onto the host particles, and (3) redistribution of the guest particles among the host particles to achieve a random distribution [62].

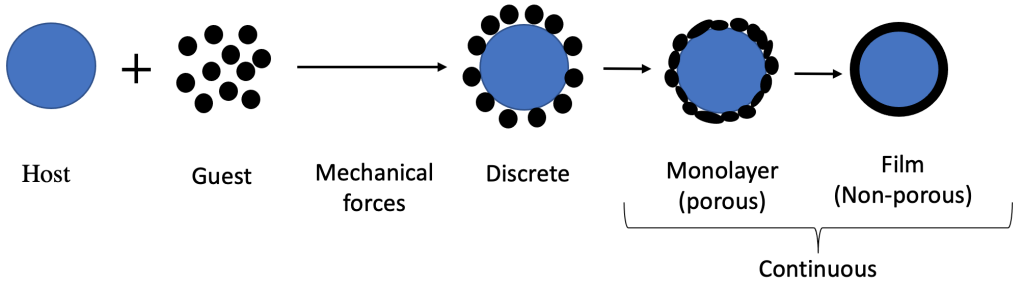


Figure 2.7: A schematic illustrating a dry-coating process. Figure inspired by Pfeffer et al. [62].

Various machines exist for dry particle coating, such as mechanofusion, where the particles are coated in a rotating vessel at a frequency ranging from 200 - 1600 rpm. To reduce coating time, the high-energy intensive hybridizer machine is a promising alternative. The hybridizer, as illustrated in Figure 2.8, features a powerful rotor with six blades that can rotate at speeds ranging from 5000 to 16 000 rmp. This high-speed rotation results in violent collisions between the host and guest particles (powder sample) within the processing chamber, facilitating the de-agglomeration and promoting powder coating. In addition, the hybridizer is equipped with a circulation tube that continuously moves the particles in and out of the chamber and onto the rotor blades. Due to the intense forces generated by the high-speed rotation, there is a temperature buildup, contributing to an even more effective coating of the guest particles onto the host particles. The processing time required to create a sufficient coating is notably shorter for hybridizers compared to other coating machines, as well as the CVD method. This could potentially reduce production time, and costs [62].

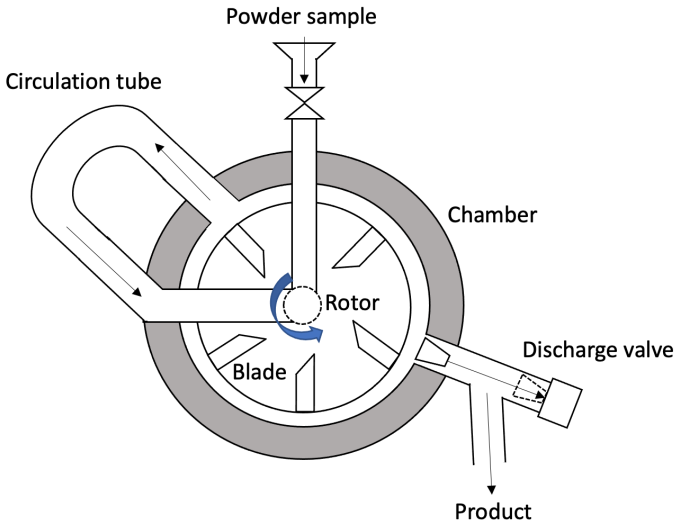


Figure 2.8: A schematic of the hybridizer process. Figure inspired by Kawaguchi et al. [63].

## 2.9 Electrochemical characterization techniques

### 2.9.1 Cyclic voltammetry

Cyclic voltammetry is a widely used technique to investigate the electrochemical processes of molecular species and chemical reactions initiated by electron transfer. The working principle of CV is based on a linear cyclic potential sweep of the working electrode (WE) at a constant rate (mV/s), as illustrated in Figure 2.9a. The WE is polarized by incrementally raising and lowering the potential between a predefined maximum and minimum while simultaneously recording the resulting current. The WE is oxidized during the positive potential sweep and reduced during the negative potential sweep. The output is a current versus potential diagram, which is known as a cyclic voltammogram [20, 64].

To investigate the redox reactions taking place in an electrode, a low scan rate is typically chosen to prevent mass transport limitations of reactants to the electrode surface [36]. Based on Yang et al. [65] studies, a voltammogram is exemplified in Figure 2.9b for an LNMO electrode cycled in a $LiPF_6$, EC:DEC (1:1) electrolyte system with low scan rate of 0.05 mV/s. Here the peaks from the positive sweep at 4.2, 4.7, and 4.75 V represent the oxidation of the $Mn^{4+/3+}$, $Ni^{3+/2+}$ and $Ni^{4+/3+}$ redox couples, respectively. The peaks at the negative sweep represent the reduction potential of the same redox couples.

Figure 2.9c demonstrates a typical voltammogram for the electropolymerization of Py. The voltammogram displays a single onset oxidation wave, followed by a wide plateau, a sharp oxidation wave, and a weaker reduction wave during the reverse scan. To detect the intermediate species (radical cations), which indicates that Py is being oxidized, a high scan rate of 100 mV/s is typically employed. The shapes of the voltammograms may vary depending on the type of solute, solvents, temperature, and other conditions.

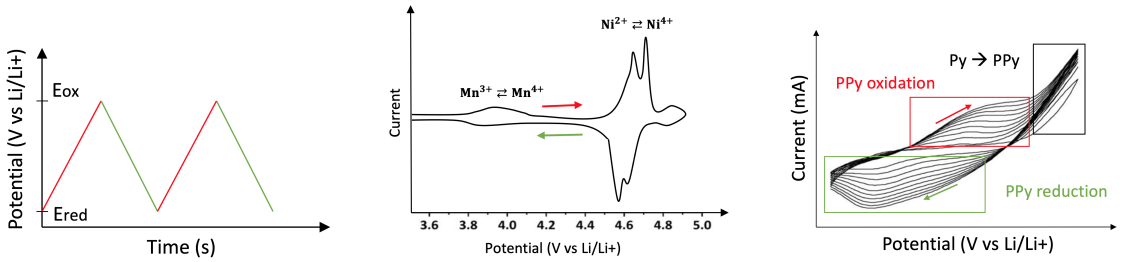


(a) (b) (c)

Figure 2.9: Working principle of cyclic voltammetry, where (a) displays the linearly applied potential against time, and (b) and (c) shows the resulting current from the applied potential for an LNMO electrode and during the electropolymerization of pyrrole (Py) to form polypyrrole (PPy), respectively. The red color represent oxidation and the green represent reduction. Figure (a) is adapted from the specialization project, (b) is adapted from Yang et al. [65], and Figure (c) is inspired by Zhou et al. [66].

### 2.9.2 Galvanostatic cycling

Galvanostatic cycling (GC) is a technique utilized to asses battery performance, as it enables the determination of key parameters such as capacity and coulombic efficiency. The test entails the application of a constant current (i.e., galvanostatically) for a specified duration while recording the resulting potential. As demonstrated in Figure 2.10a, a positive current is applied during charging, while a negative current is applied upon discharge. Figure 2.10b displays the corresponding potential response to the applied current. The amount of current applied depends on a set C-rate, which is determined by the expected theoretical capacity. To exemplify, an LNMO-based cell with 10 mg of AM and an expected theoretical capacity of 140 mAh/g being charged at C/10, requires an applied current of 0.14 mA to be fully charged in 10 hours. To avoid overcharging, the potential response is restricted by predetermined upper and lower cut-off voltages. For an LNMO based cell, the lower and upper cut-off voltage is typically about 3.0 V and 4.9 V, respectively. The cycling data is usually presented in a charge-discharge plot, where the electrode's specific capacity is plotted against the voltage. The capacity parameters can be derived from Equation 2.9. Figure

2.10c illustrates a standard charge-discharge profile for the LNMO electrode, which displays distinct plateaus at 4.75 V, 4.7 V, and 4.2 V corresponding to the redox couples of $Ni^{4+/3+}$, $Ni^{3+/2+}$, and $Mn^{4+/3+}$, respectively [10].

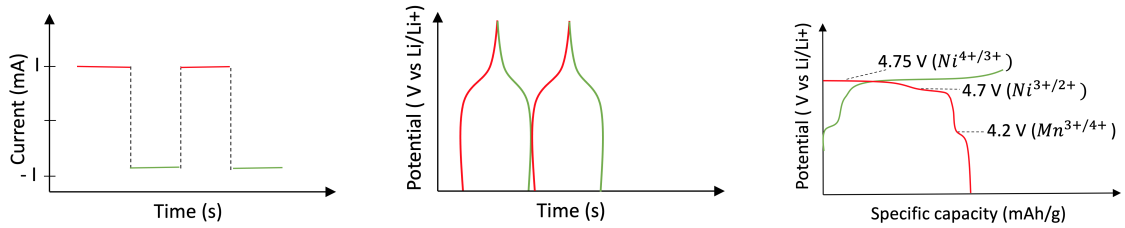


(a) (b) (c)

Figure 2.10: Working principle of a galvanostatic cycling test, where (a) illustrates the applied current as a function of time, (b) shows the corresponding voltage from the applied current as a function of time, and (c) illustrates the charge-discharge profile where the potential (V vs $Li/Li^+$) is plotted against specific capacity (mAh/g). The red and green colors represent oxidation and reduction, respectively. Figure reused from Specialization project.

### 2.9.3 Intermittent Current Interruption

The Intermittent current interruption (ICI) is an electrochemical technique used to track the battery's resistive properties across its entire state of charge (SOC). The battery is charged and discharged with a relatively low current rate (C/5 or C/10), and the current is regularly interrupted for short periods (e.g., every 5 min with 5 s interruption). At low current rates, the battery is closer to its equilibrium state during cycling, and more precise results can be obtained. Following every interruption during charge, there is a rapid drop in voltage followed by a decline with a linear correlation to the square root of time. As different electrochemical processes in a battery occur at different time scales, the resulting time constant for each voltage response is related to different processes. An illustration of the voltage response during charge is presented in Figure 2.11 [67].

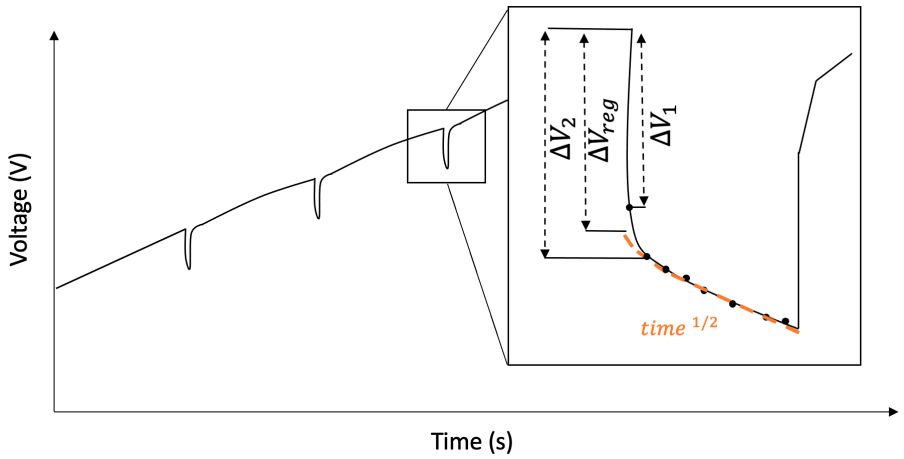


Figure 2.11: Illustration of the Intermittent current interruption (ICI) method where the current is interrupted for a short period after a longer period of charging. Including a section of the voltage response at various time constants during the current interruption. Figure inspired by Geng et al. [67].

The abrupt decline in voltage ($\Delta V_1$), which takes place within the millisecond timeframe, is associated with the bulk electrolyte's ionic resistance and the electronic resistance of the electrodes and current collectors. This voltage drop is independent of the battery SOC and is a pure resistive parameter. After about 1s ($\Delta V_2$), charge transfer reactions appear. As time passes, the voltage drops are mainly governed by diffusion ($\Delta V_2$), as diffusion in the solid is the slowest of the three

processes. These time constants are somewhat arbitrary and reliant on the battery-specific materials used. It is also challenging to obtain precise time constants due to often noisy environments or poor sampling rates. Rather than tracking the resistance at a particular time, the various time scales can be removed by extrapolating the voltage response to t=0 using linear regression [67]. The resulting resistance ($\Delta V_{reg}$) can then be estimated using Ohm's law:

$$R_{reg} = -\frac{\Delta V_{reg}}{I} \tag{2.22}$$

where I is the current prior to the interruption.

The ICI technique requires a system that is controlled by diffusion, and where V is directly proportional to the square root of time. Furthermore, due to the simplification of the system, certain processes cannot be distinguished directly. Electrochemical Impedance Spectroscopy (EIS) can differentiate the voltage drops contributions from ohmic losses, SEI and CEI layers, charge transfer, and concentration polarization. This is accomplished by employing an alternating signal (current to potential) with a particular amplitude over a frequency range spanning from MHz to mHz. Nevertheless, each EIS measurement must be carried out at a fixed SOC and does not permit the continuous evaluation of battery resistance [67].

The ICI method can also provide a diffusion-related parameter. This parameter characterizes the diffusion behavior of both the anode and cathode, as it is not possible to differentiate their individual impacts. It is, however, possible to correlate the diffusion parameter obtained from the ICI with a diffusion parameter obtained from the Warburg impedance in an EIS measurement [67]. This thesis will mainly focus on the resistive behavior of the LIB.

## 2.10 Raman spectroscopy

Raman spectroscopy is a chemical analysis technique used to obtain detailed information about chemical structure and molecular interactions. By sending monochromatic light, usually from a laser in the visible range (e.g., 530 nm ), into the sample of interest, a small fraction of photons will gain or lose energy through the interaction with molecular vibrations, resulting in inelastic scattering. The inelastic scattering is known as Raman scattering, and the energy shift provides information about the unique molecule vibrations of the system. Detection of the inelastically scattered photons is used to generate a Raman spectrum, where the intensity of the scattered photos is plotted against the Raman shift (1/cm). The resulting spectrum can be viewed as a structural fingerprint by which different molecules can be identified. The peak intensity is proportional to the concentration of the respective species, and the peak intensity ratio between different Raman signature peaks can provide information about the material's crystallinity, phase transition, and structural disorder. This is a surface-sensitive technique with a few hundred nanometers of probing depth [10].

Molecules relevant to LNMO, CB and PPy, which are the molecules of interest for the Raman analysis performed in this thesis, are presented in Table 2.3. For the LNMO structure, peaks around 166 and 410 $cm^{-1}$ are related to the ordering of its spinel structure [68]. Highly crystalline graphite exhibits a single Raman peak at 1582 $cm^{-1}$ originating from in-plane vibration of carbon atoms in a graphite layer. However, in the amorphous structure of carbon black with graphitic-like crystals, an additional peak appears around 1350 $cm^{-1}$ due to the structural disorder near the edge of the graphite-like part that disrupts the symmetry of graphite [69].

For the PPy, the peak at 1600 $cm^{-1}$, which is ascribed to a C=C stretching vibration of the PPy backbone, usually has a high intensity compared to the other peaks. If this peak is shifted toward a higher frequency, it may suggest a higher degree of oxidized species [70, 71]. In addition, a complicated morphology could introduce more strain on the C=C bond, which may also result in a peak shift towards a higher frequency [71]. From the double peaks at 1050 and 1080 $cm^{-1}$ and 1320 and 1380 $cm^{-1}$, the 1080 and 1380 $cm^{-1}$ results from the oxidation of PPy. The peaks at 940 and 990 $cm^{-1}$, which are attributed to ring deformation, are linked to di-cations and radical cations, respectively [71]. Varade et al. [71] galvanostatically electropolymerized Py onto a platinum plate where Tetrabutylammonium hexafluorophosphate ($TBAPF_6$) served as both the solvent and the dopant ($PF_6{}^-$). From Raman analysis, they observed a peak at 1240 $cm^{-1}$ where the explicit assignment of the band is uncertain. However, they argued that it might be assigned to the C=C stretching. According to Valtera [70], the 1240 $cm^{-1}$ origins from antisymmetric C-H deformation vibrations.

Table 2.3: Raman characteristic peaks for an LNMO, Carbon Black (CB) and polypyrrole (PPy) spectrum according to Boulet-Roblin et.al [72], Pawlyta et al. [69], and Varade et.al [71], respectively. $\nu$ correspond to stretching mode, and $\delta$ to the bending modes.

| **Frequency ($cm^{-1}$)** | **Assignment** |
|---|---|
| LNMO | |
| 642 | Li-O ($\delta$), Mn-O-Li ($\delta$) |
| 599 | Li-O ($\nu$), O-Mn-O ($\delta$) |
| 509 | O-Li ($\nu$) |
| 166, 410 | Ni-O |
| CB | |
| 1582 | In-plane vibration in the graphite layer |
| 1350 | Disorder near the edge of the graphitic-like domain. |
| PPy | |
| 1600 | Symmetric C=C ring stretching |
| 1380, 1320 | Ring stretching vibration |
| 1080, 1050 | C-H in-plane deformation |
| 990 | Ring deformation vibration of di-cation units |
| 940 | Ring deformation of radical cations |

# Chapter 3

# Experimental methods

The experimental part of this work can be divided into three different parts, where Figure 3.1 presents an overview of the different tests conducted in each part.

In part A, the LNMO particles were carbon-coated using a chemical vapor deposition (CVD) method and a hybridizer machine, and the resulting powders were characterized using Scanning Electron Microscopy (SEM), Energy-dispersive X-ray spectroscopy (EDX) and X-ray diffraction (XRD). Thin LNMO electrodes were cast from the hybridizer-coated powder and assembled into coin half-cells, which were electrochemically characterized through galvanostatic cycling (GC) and intermittent current interruption (ICI). In the second part B of the project, once a carbon coating with sufficient electrochemical properties was achieved, three-electrode cells were assembled using Al and carbon-coated Al-foil (C-Al) as positive electrodes. The Py additive was then electropolymerized onto the Al and C-Al foil via cyclic voltammetry (CV). The PPy-layer on the positive Al and C-Al electrodes was investigated post-mortem through SEM analysis and Raman spectroscopy. Lastly, in part C, three-electrode cells and half coin cells with LNMO and carbon-coated LNMO electrodes were assembled and electrochemically characterized through CV and GC, respectively. Finally, the three-electrode cells were disassembled, and the LNMO electrodes were characterized using SEM analysis and Raman spectroscopy to investigate whether a PPy-layer had formed on the electrode surface.

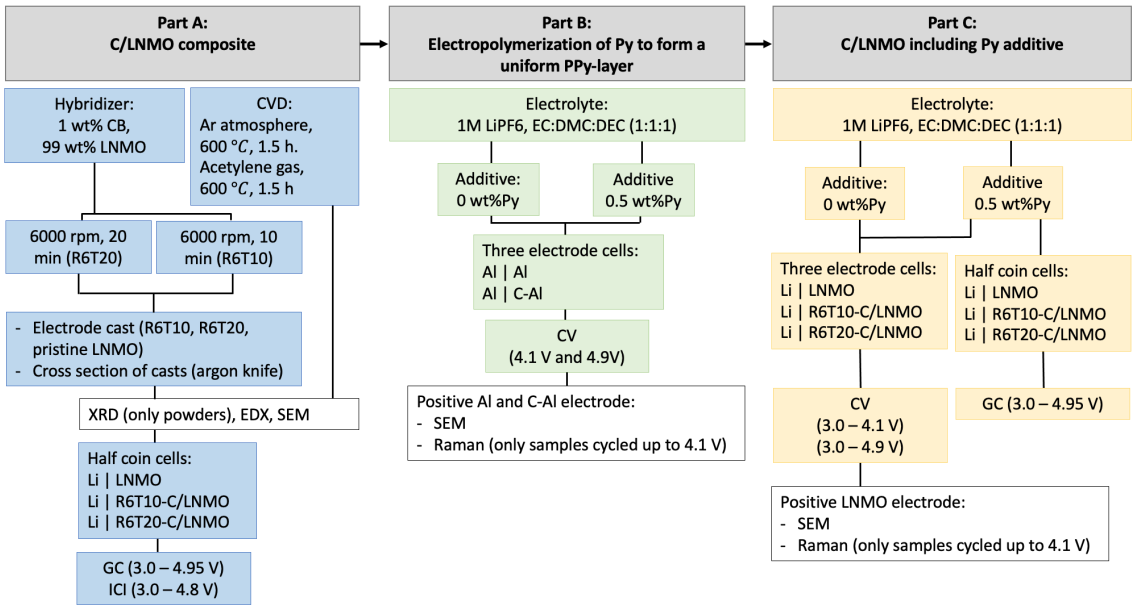


Figure 3.1: A flowchart presenting the different tests done at the different stages of the experimental work.

## 3.1 Preperation of C/LNMO composite

### 3.1.1 CVD

The $LiNi_{0.5}Mn_{1.5}O_2$ (LNMO) powder to be carbon coated was supplied by Haldor Topsøpe and had a particle size ranging from 6.0 to 10.0 $\mu$m in diameter. The carbon-coating was done using the chemical vapor deposition (CVD) method in a Nabertherm tube furnace.

To begin with, 2.0 g of pristine LMNO powder was placed in a ceramic crucible at the center of the tube furnace. The temperature was then increased from room temperature to 300 °C under a pure argon atmosphere at a heating rate of 300 °C/h. After reaching 300 °C, the furnace was evacuated, and acetylene was introduced as the precursor gas. The temperature was then raised from 300 to 600 °C, and held constant for 1.5 hours before being cooled at a rate of 480 °C/h until reaching room temperature (20 °C). The LNMO particles coated with acetylene as a carbon source are named C/LNMO-ac.

To later investigate if the crystal structure of LNMO changed during heat treatment, pristine LNMO powder was heated according to the same procedure as described above. However, no acetylene gas was introduced, and the powder was only exposed to argon gas.

### 3.1.2 Hybridizer

The energy-intensive hybridization method was the second method used to carbon coat the LNMO particles. LMNO was the host material, and Carbon Black (CB, super C65, IMERYS) was the guest material with its significantly smaller particle size (nanoscale) compared to the LNMO (microscale) First, a mix of 1 wt% CB and 99 wt% LNMO was prepared by adding 0.1 g of CB to 10 g of LNMO. To ensure a well-dispersed mix without any agglomerations, the CB:LNMO powder mix was dry-mixed using the Thinky mixer ARE-250. It was mixed for 5 minutes at a speed of 500 rpm and then for 5 minutes at 1000 rpm. This was repeated four times, with 10 minutes between each time, allowing the powder to cool down. The sample name of the powders hybridized at 6000 rpm for 10 minutes and 6000 rpm for 20 minutes are named R6T10 and R6T20, respectively.

After pre-mixing, the CB:LNMO powder was hybridized using the NARA hybridizer system. The first test was done at a speed of 6000 rpm for 10 minutes, and a second test was done at the same rpm but for 20 minutes. The increased hybridizer time was done to investigate if a longer hybridizing time would affect the carbon coating.

### 3.1.3 C/LNMO composite characterization

The LNMO's carbon coating morphology and uniformity on all prepared powders were investigated using the JEOL JSM-7900F SEM. First, the powders were collected and evenly dispersed onto carbon tape on an SEM stub. To examine the surface characteristics, a low acceleration voltage of 5 kV and a working distance of 10 mm was set. The chemical composition of the carbon-coated LNMO powders was also investigated using the SEM-integrated EDS from Oxford Instrument AZtec. The working distance was kept at 10 mm, but the acceleration voltage was increased to 10 kV.

The crystallinity of the powders was determined using the Bruker D2 Phaser XRD with Cu$K_\alpha$ radiation (1.5406 Å). The measurement was done using a coupled $2\theta/\theta$ scan type with a continious measurment starting from 10° to 80°, a step size of 0.02 °, a sample rotation speed of 30 000 1/min and a fixed slit mode. The Cu$K_2, \alpha$ was stripped, and the background was removed for all measurements. The total scan time was set to 1 hour.

## 3.2 Cell manufacture

### 3.2.1 Slurry preparation and tape casting

To prepare a slurry mix, the active material (AM), the conductive agent carbon black (CB, super C65, IMERYS)), and the polyvinylidene fluoride (PVDF) binder were mixed in a ratio of 90:5:5 wt% (AM:CB:PVDF). First, the PVDF binder was dissolved in an N-methyl-2-pyrrolidone (Sigma-Aldrich, NMP, anhydrous, purity $\geq$ 99.9 %) solvent with a ratio of 1:20 (PVDF: NMP) and stirred by a magnetic stirrer overnight. The mixing process began by adding the AM and CB powders to

a small container, followed by adding the PVDF:NMP solution. Lastly, extra NMP was added to reach a powder-to-solvent ratio of 1:2. The slurry was mixed using the Thinky mixer ARE-250. It was mixed for 5 minutes at a speed of 1500 rpm and then for an additional 10 minutes at 2000 rpm.

The prepared slurry mix was coated onto an Al-foil using the tape caster Hohsen-MC20 with a vacuum to prevent the Al-foil from moving. Wrinkles on the Al-foil were removed before coating by smoothing the Al-foil using a tissue moistened with isopropanol. A thin and straight line of the slurry was poured in front of the doctor blade (Hohsen Corp.), which had a raised cap of 150 $\mu$m. The raised cap corresponds to the desired wet film thickness of the electrode. The slurry was coated with a shear rate of 2.0 $s^{-1}$.

The casted electrodes were dried overnight at 120 °C (in a Nabertherm oven) and then for 3 hours in a vacuum at the same temperature. After drying, the electrodes were cut into 15 mm discs using an electrode cutter (Hohsen Corp.). The electrode discs were weighted and then placed in a vacuum for 30 minutes to remove residual oxygen and moisture before being introduced into the glove box. The AM mass was determined by subtracting the current collector mass from the total electrode mass and then multiplying it with the weight percentage of AM.

A total of three casts were prepared, where pristine LNMO, R6T10-C/LNMO, and R6T20-C/LNMO were used as the AM.

### 3.2.2 Characterization of manufactured electrode casts

To investigate the integrity and morphology of the carbon coating after electrode manufacture, the electrode surface and a cross-section of the electrodes (including the non-carbon-coated LNMO casts) were characterized using SEM and EDX. The SEM and EDX analysis settings was the same as described in Section 3.1.3. The cross-sections were made using the cooling cross Section Polisher IB-19520CCP from Jeol. A small piece of about 0.5x0.5 $cm^2$ was cut out from the electrode cast and placed in the sample holder so that the Al-foil faced the Argon ion beam. The polishing time was set to 1 hour with an ion beam acceleration voltage of 6kV, followed by 15 minutes of fine polishing with an acceleration voltage of 4kV. The temperature was set to -20 °C, and liquid nitrogen gas was used for cooling. The thickness of the carbon coating was measured using the ImageJ software.

### 3.2.3 Three-electrode cell and half coin-cell assembly

In this project, a conventional electrolyte system consisting of 1 M lithium hexafluorophosphate ($LiPF_6$) and ethylene carbonate (EC), diethyl carbonate (DEC), and Dimethyl carbonate (DMC) in a 1:1:1 wt% ratio (Solvionic, anhydrous, purity $\geq$ 99.9 %) were used. Herein referred to as the reference electrolyte. An electrolyte solution containing pyrrole (Py)(Acros Organics, anhydrous, purity $\geq$ 99.9 %) as an additive was prepared by adding 0.5 wt%Py to 1.0 g of reference electrolyte, and the solution was stirred for 3 hours using a magnetic stirrer. The weight percentage of Py was selected based on the results obtained in the specialization project.

The flowchart in Figure 3.1 provides an overview of the electrolytes, counter electrodes, and working electrodes used for the three-electrode and half-coin cells. Before assembling the cells, polypropylene separators (Celgaard 2400) were punched into 21 mm and 18 mm diameter discs for three-electrode cells and coin cells, respectively. All working (positive) electrodes were cut into 15 mm discs using an electrode cutter. Any potential oxide or nitride layers were also brushed away from pre-cut 15.6 mm Li-metal discs for the cells using Li-metal as the counter electrode.

The three-electrode cells (RedoxMe) were assembled as described in Figure 3.2. To prepare the reference electrode (step 10), the reference electrode tip was carefully pushed onto the Li-metal so that a small piece of Li filled its hole.

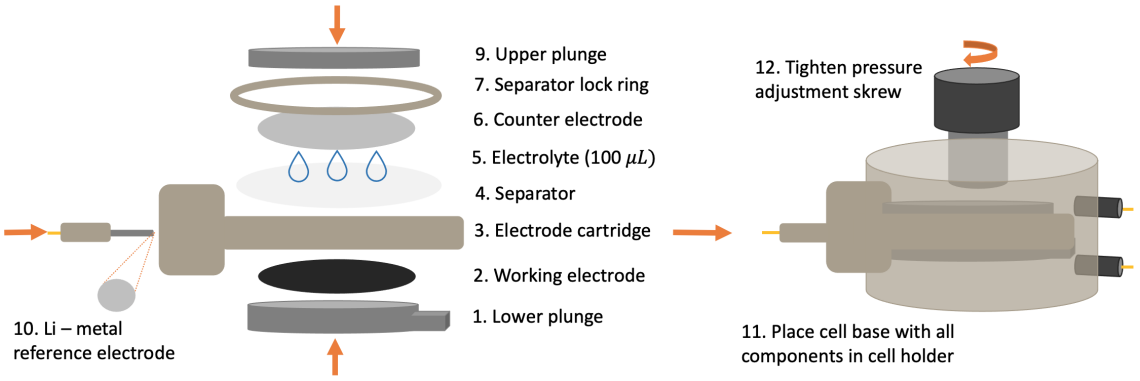


Figure 3.2: Three-electrode cell components and the corresponding assembly procedure. The figure is adapted from the Specialization project.

The assembly of the coin cells (2030, Hohsen Corp.) was carried out according to the procedure illustrated in Figure 3.3, and then sealed using a manual coin cell crimper (Hohsen Corp).

All work related to cell assembly, except for the preparation of separators and cutting of electrodes, was executed in an Argon-filled glovebox (MBRAUN) with an $H_2O$ and $O_2$ content below 0.1 ppm.

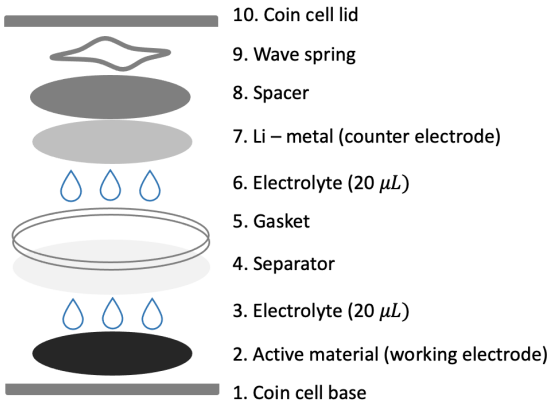


Figure 3.3: Half coin-cell assembling procedure. Figure inspired by Bryntensen et al. [73].

## 3.3 Electrochemical characterization

### 3.3.1 Cyclic voltammetry

Cyclic voltammetry (CV) was employed for the electropolymerization of Py onto the working electrode and to investigate at which potential electropolymerization occurred. The CV was conducted on three-electrode cells, utilizing a Biologic SP-300 battery cycler.

Figure 3.1 and Table 3.1 presents the various cell configurations tested, where two tests were performed on each configuration. For all tests, the scan rate was set to 1 mV/s. In the first test, the potential was swept from 0 V vs. $V_{OC}$ to 4.1 V vs. $Li/Li^+$, followed by a reversed sweep to 0 V vs. $V_{OC}$. This constitutes one cycle. In the second test, the potential was swept from 0 V vs. $V_{OC}$ to 4.9 vs. $Li/Li^+$, and then back to 0 V vs. $V_{OC}$. A total of 4 cycles were conducted for each test.

Table 3.1: Overview of the different three-electrode cells tested. All cells use Li metal as the reference electrode and a 1 M $LiPF_6$, EC:DMC:DEC 1:1:1 electrolyte system. The cell is named based on the working electrode used and the weight percentage (wt%) of the pyrrole (Py) electrolyte additive used.

| Cell name | Counter electrode | Working electrode |
|---|---|---|
| Al | Al | Al |
| Al, 0.5 wt%Py | Al | Al |
| C-Al | Al | C-Al |
| C-Al, 0.5 wt%Py | Al | C-Al |
| Pristine LNMO | Li | Pristine LNMO |
| Pristine LNMO, 0.5 wt%Py | Li | Pristine LNMO |
| R6T10-C/LNMO | Li | R6T10-C/LNMO |
| R6T10-C/LNMO, 0.5 wt%Py | Li | R6T10-C/LNMO |

### 3.3.2 Galvanostatic cycling

Using an Arbin BT2000 battery cycler, the galvanostatic cycling (GC) technique was used to evaluate the long-term cycling performance and rate capability of half coin cells.

After cell assembly, the cells were put to rest for 12 hours to ensure sufficient electrolyte wetting of the separator and electrodes. As the cells were initially in a discharged state, all cycles started with a charging step. To preserve the integrity of the LNMO crystal structure, a cut-off voltage of 4.9 V and 3.0 V was set during the charge and discharge processes, respectively. The AM mass of each cell was also added to the program to enable a continuous calculation of the specific capacity. Furthermore, a C-rate of 1C was defined as the current required to completely discharge or charge the cell within an hour, given a theoretical capacity of 140 mAh/g. In order to facilitate the formation of a protective SEI, CEI and PPy layer (for cells containing Py electrolyte additive), a relatively low C-rate of C/20 was set during the first five cycles (formation cycles). The C-rate was set to C/10 for the subsequent 100 cycles for long-term cycling. To examine the cell's rate capability, a stepped approach was employed whereby the C-rate was incrementally increased every fifth cycle, yielding five cycles at rates of C/20, C/10, C/5, C/2, 1C, and 2C, and then ultimately returning to C/10. The cells were put to rest for 15 minutes between each half-cycle for the long-term cycling and the rate test.

A total of 18 half coin-cells were tested in long-term cycling, and the rate test was conducted on six cells. An overview of the different cell configurations is presented in Table 3.2.

Table 3.2: Overview of the different half coin-cells tested, and their respective active material (AM) loading. All cells have Li metal as the counter electrode and a 1 M $LiPF_6$, EC:DMC:DEC 1:1:1 electrolyte system. The cell is named based on the working electrode/AM used and the weight percentage (wt%) of the pyrrole (Py) electrolyte additive. For the samples with carbon-coated LNMO (R6TX - C/LNMO), the AM loading includes the carbon.

| Cell name | cell number | AM loading ($mg/cm^2$) |
|---|---|---|
| Long-term cycling | | |
| Pristine LNMO | 1 | 4.13 |
| Pristine LNMO | 2 | 6.38 |
| Pristine LNMO | 3 | 6.04 |
| | | |
| R6T10-C/LNMO | 1 | 7.21 |
| R6T10-C/LNMO | 2 | 7.81 |
| R6T10-C/LNMO | 3 | 7.59 |
| | | |
| R6T20-C/LNMO | 1 | 4.36 |
| R6T20-C/LNMO | 2 | 6.02 |
| R6T20-C/LNMO | 3 | 6.19 |
| | | |
| Pristine LNMO, 0.5 wt%Py | 1 | 5.94 |
| Pristine LNMO, 0.5 wt%Py | 2 | 6.41 |
| Pristine LNMO, 0.5 wt%Py | 3 | 4.14 |
| | | |
| R6T10-C/LNMO, 0.5 wt%Py | 1 | 7.55 |
| R6T10-C/LNMO, 0.5 wt%Py | 2 | 5.10 |
| R6T10-C/LNMO, 0.5 wt%Py | 3 | 5.71 |
| | | |
| R6T20-C/LNMO, 0.5 wt%Py | 1 | 4.55 |
| R6T20-C/LNMO, 0.5 wt%Py | 2 | 6.53 |
| R6T20-C/LNMO, 0.5 wt%Py | 3 | 6.60 |
| | | |
| Rate tests | | |
| Pristine LNMO | 1 | 4.13 |
| Pristine LNMO | 2 | 6.38 |
| Pristine LNMO | 3 | 6.04 |
| | | |
| R6T10-C/LNMO | 1 | 5.73 |
| R6T10-C/LNMO | 2 | 5.68 |
| R6T10-C/LNMO | 3 | 5.38 |

### 3.3.3 Intermittent Current Interruption

The Biologic SP-300 battery cycler was utilized to investigate how the cell resistance changes with state-of-charge (SoC) using the Intermittent Current Interruption (ICI) technique. Half coin-cells were cycled between 3.0 and 4.8 V at a constant charge/discharge current rate of C/10. Every 5 minutes, the charge/discharge process was stopped for 5 s while recording the potential drop every 0.2 s. A total of three cycles were completed for each cell.

Three cycles were completed for each cell with LNMO, R6T10-C/LNMO, and R6T20-C/LNMO as working electrodes.

## 3.4 Post-mortem characterization

After CV, the three-electrode cells were disassembled under a fume hood. To remove any remaining electrolyte while preventing damage to any potential PPy-layer (for the samples containing Py), the working electrode surface was carefully cleaned using polyester cleanroom wipes followed by overnight drying at 50 °C. The electrodes were analyzed using SEM using the same settings as

described in Section 3.1.3. To investigate the presence of a PPy-layer, elemental analysis was performed using Raman spectroscopy for the cells cycled up to 4.1 V. The spectroscopy was conducted with a WITec Alpha 300R spectrometer using a 530 nm Laser, 600 line/mm grating, 50X lens magnification, and 0.2 % laser power with a 10.0 s integration time and 6 accumulations.

# Chapter 4

# Results and discussion

## 4.1 Carbon coating of LNMO particles

### 4.1.1 CVD process

To verify that the LNMO particles were carbon coated during the chemical vapor deposition (CVD) process, its surface morphology was investigated. Figure 4.1 shows the morphology of the pristine LNMO powder, which is recognized from its spherical shape. Figure 4.2 shows the LNMO powder after exposure to acetylene gas for 1.5 h at 600 °C (C/LNMO-ac). The SEM images show a significant change in the surface morphology, where the surface of the C/LNMO-ac appears more porous than the pristine LNMO.

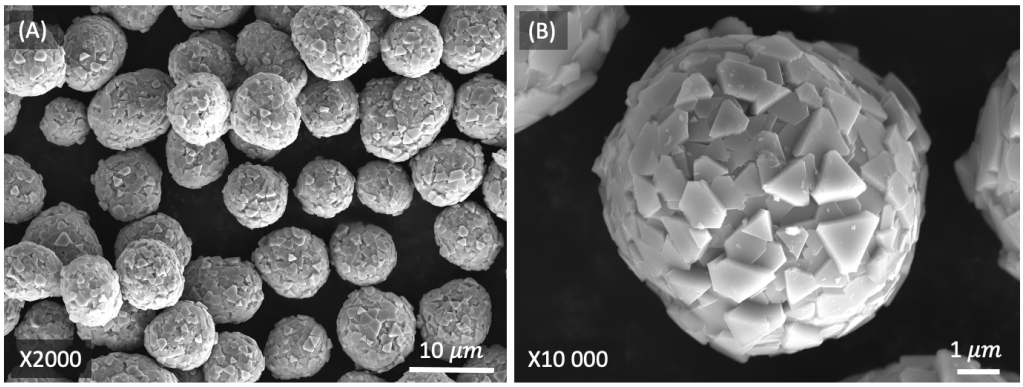


Figure 4.1: SEM images of pristine LNMO powder. Working distance 10 mm, acceleration voltage 5 kV, and a magnification of (A) x2000 and (B) x10000.

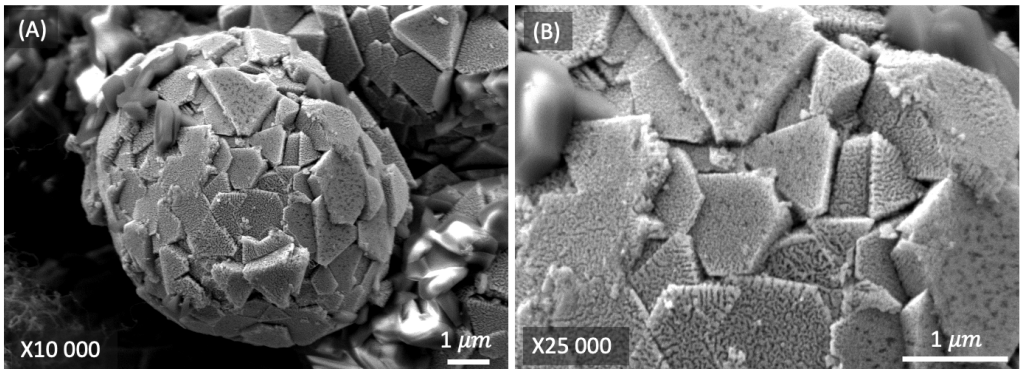


Figure 4.2: SEM images of the C/LNMO-ac powder, where the LNMO powder has been exposed to acetylene gas for 1.5 h at 600 °C in a chemical vapor deposition (CVD) process. Working distance 10 mm, acceleration voltage 5 kV, and a magnification of (A) x10000 and (B) x25000.

To further investigate the reason behind the observed variation in surface morphology, an XRD analysis was conducted to determine if the change was due to a carbon coating, the heat treatment, or changes in LNMO's crystal structure upon acetylene exposure. The XRD results for the pristine LNMO, C/LNMO-ac, and heat-treated LNMO exposed to the same conditions as the C/LNMO-ac but without acetylene gas are presented in Figure 4.3. The pristine and heat-treated LNMO powders were found to display the characteristic peaks of the LNMO structure, denoted with black bars. Hence the heat treatment did not affect the crystal structure. These results were expected as the LNMO structure should be stable below 700 °C as discussed in Section 2.3.1. However, the crystal structure of the C/LNMO-ac powder significantly changed after exposure to acetylene. A search and mapping analysis of the C/LNMO-ac peaks revealed the presence of Ni-metal (blue stars), lithium carbonate ($Li_2CO_3$) (orange stars), and manganese oxide (MnO) (red stars). A possible explanation for these results could be that the decomposition of acetylene created a hydrogen-rich reducing atmosphere, where the Ni in the LNMO structure was reduced to metallic Ni. In addition, the carbon from the acetylene may have reacted with Li and oxygen in the LNMO structure, forming a lithium carbonate ($Li_2CO_3$) at the particle surface and leaving behind manganese oxide (MnO) in the bulk of the particle.

Due to the decomposition of the LNMO structure, which was most likely caused by a reducing atmosphere when using acetylene as the carbon source in the CVD method, the LNMO particles to be investigated as cathodes were coated with carbon black (CB) using a hybridizer machine.

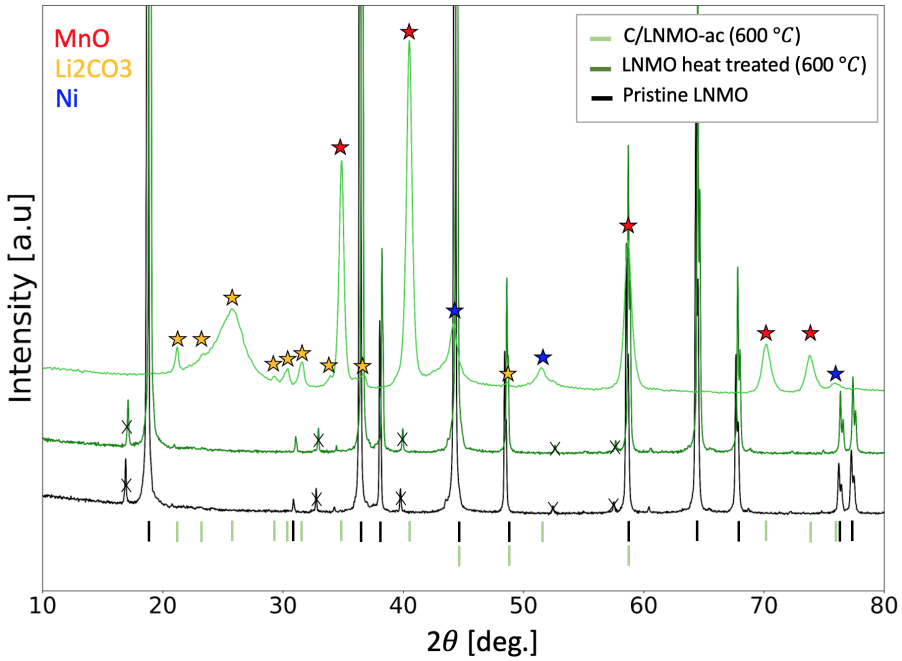


Figure 4.3: XRD diffractogram of pristine LNMO, heat-treated LNMNO, and LNMO powders exposed to acetylene gas for 1.5 h at 600 °C. The peaks marked with a black cross are beta-peaks which were not filtered out during the test. The black bars refer to an LNMO phase. Red, Yellow, and blue starts refer to a MnO, a $Li_2CO_3$, and a Ni metal phase, respectively.

### 4.1.2 Carbon Black coating by the application of a hybridizer machine

The surface morphology of the particles and the cross-sections of casted electrodes were investigated to evaluate whether a carbon coating was formed on the LNMO particles during the dry-coating process using a hybridizer machine.

LNMO particles hybridized at 6000 rpm for 10 and 20 minutes are displayed in Figure 4.4a and Figure 4.4b, respectively. A distinct difference in surface morphology is observed between the pristine LNMO particles in Figure 4.1 and the hybridized ones in Figure 4.4, where the relatively smaller CB particles seem to have formed a coarse surface layer on the larger LNMO particles during the coating process. From the overview SEM image in Figure 4.4a and 4.4b at a magnification of x2000, the particles hybridized for 20 minutes (R6T20-C/LNMO) seem to have a more evenly

dispersed, dense, and uniform carbon coating compared to the particles hybridized for 10 minutes (R6T10-C/LNMO). Despite the more uniform coating obtained from an increased hybridizing time, partially coated LNMO particles are observed in both samples.

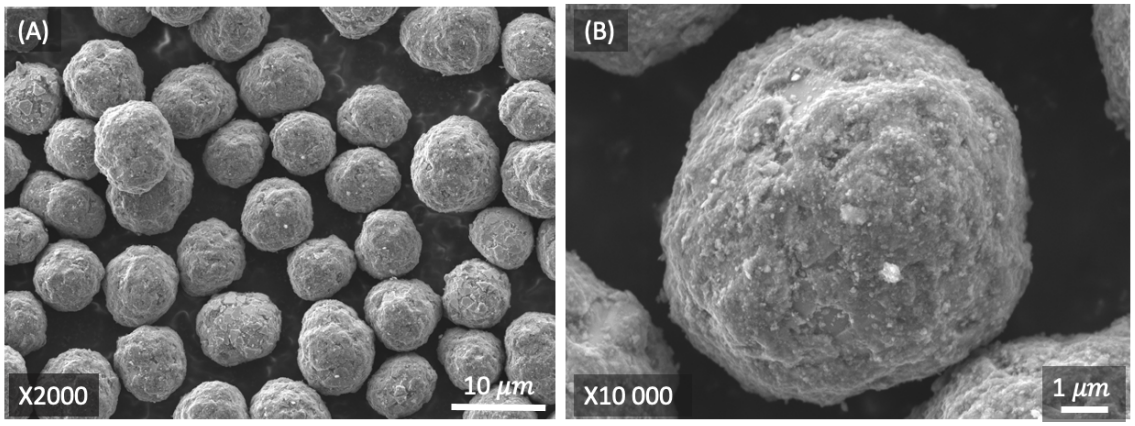


(a) R6T10-C/LNMO powder

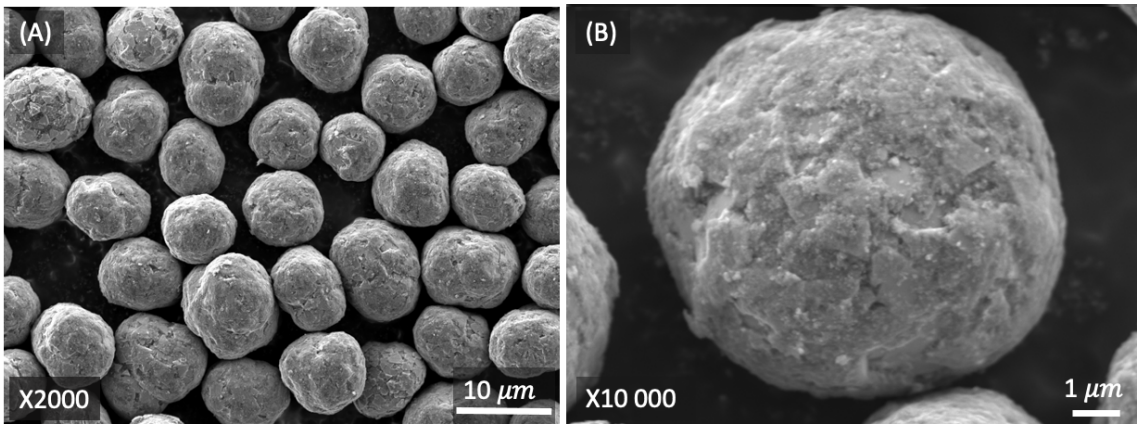


(b) R6T20-C/LNMO powder

Figure 4.4: SEM images of LNMO powder carbon coated in a hybridizer machine with 99 wt% LNMO and 1.0 wt% CB particles at 6000 rpm for (a) 10 minutes, and (b) 20 minutes. Working distance 10 mm and acceleration voltage 5kV.

Figures 4.5a, 4.5b and 4.5c shows cross-sections of a pristine LNMO, R6T10-C/LNMO, and R6T20-C/LNMO electrode cast, respectively. The LNMO particles are recognized from their spherical shape, while the material between the particles is the PVDF binder and CB additive. The yellow bars in Figure 4.5a show the depth of valleys observed on the surface of the LNMO particles, while the yellow bars in Figures 4.5b and 4.5c shows the thickness of a layer that is assumed to be the carbon coating. The reason for this assumption is that such a layer is not present on the pristine LNMO particles, and the surface morphology of the R6T10-C/LNMO and R6T20-C/LNMO is similar to what was observed in Figure 4.4a and Figure 4.4b. ImageJ software was used to measure the depth of valleys and the coating thickness.

The depth between the valleys on the surface of the pristine LNMO particle varied between 58 - 406 nm. Meanwhile, the carbon coating thickness on the R6T10-C/LNMO ranged from no coating to a coating thickness of 1.2 $\mu$m, and it had an average coating thickness of about 492 nm from ten measurements, not including the non-coated areas. For the R6T20-C/LNMO particles, the carbon coating thickness ranged from no coating to 350 nm, with an average coating thickness of about 164 nm from nine measurements, also excluding the non-coated areas. Thus, the presumed carbon coatings' thickness varied significantly.

In Figure 4.4a and 4.4b, some CB seems to be present between the valleys of the partly coated LNMO particles. However, in these areas, the valleys were likely too deep for the CB to build up a thickness larger than 406 nm, resulting in some particles only being partially coated. A larger

weight percentage of CB could have been used to fill in the gaps. However, this could have led to a very thick coating thickness. According to previous research [15], to ensure stable $Li^+$ transport across the coating and electrode interface, the best results were obtained with a coating thickness below 70 nm. Thus, the coating achieved for both the R6T10-C/LNMO and R6T20-C/LNMO is higher than what is recommended in previous research. Notably, a longer hybridizing time did result in a generally thinner coating.

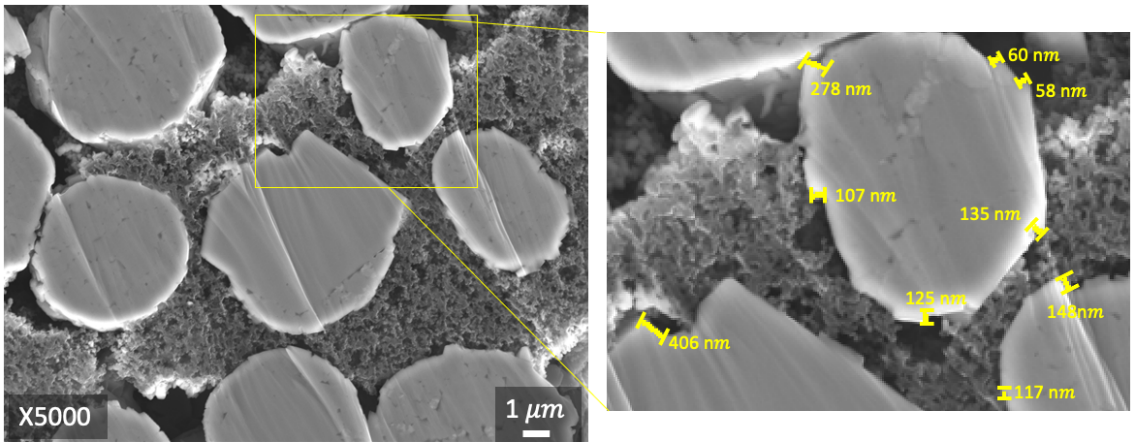


(a) Pristine LNMO cast

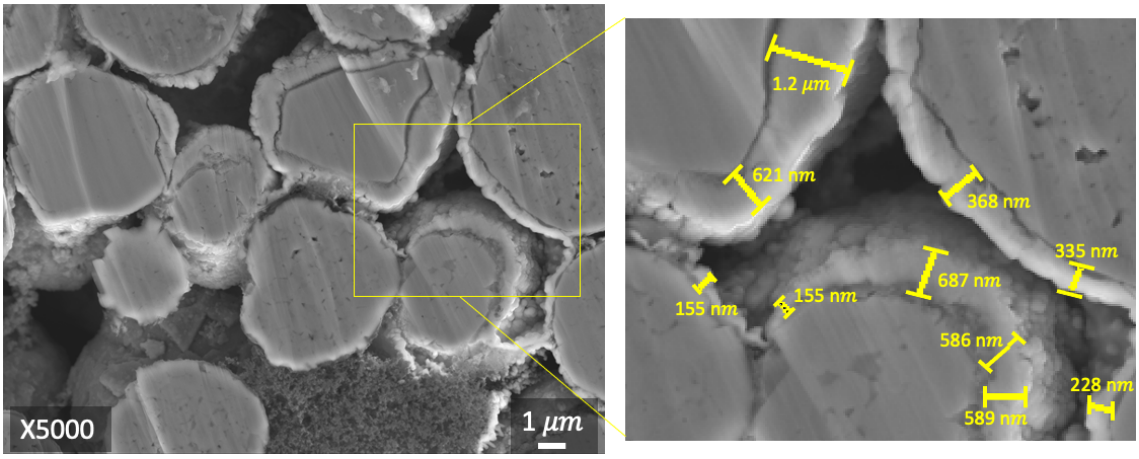


(b) R6T10-C/LNMO cast

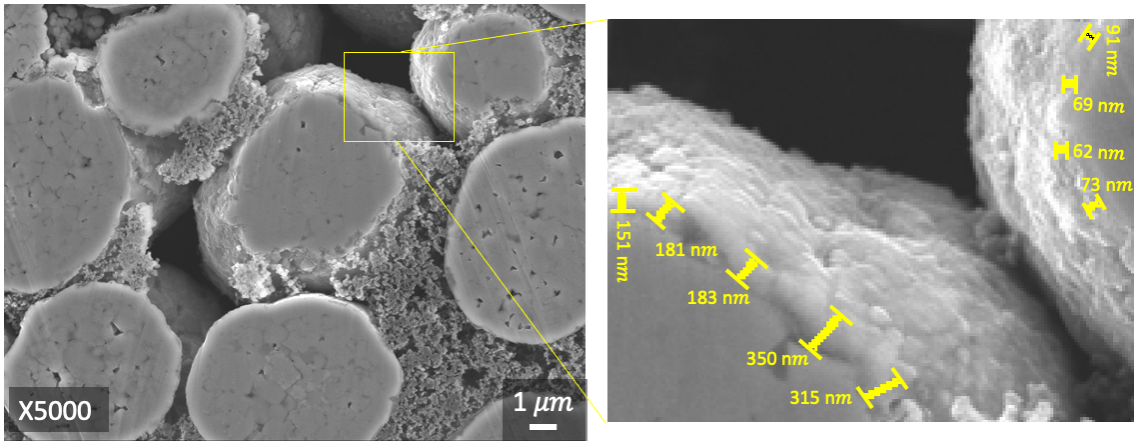


(c) R6T20-C/LNMO cast

Figure 4.5: Cross-section of electrode casts with (a) Pristine LNMO, and particles hybridized with 99 wt% LNMO and 1.0 wt% CB powders at 6000 rpm for (b) 10 minutes (R6T20-C/LNMO), and (b) 20 minutes (R6T20-C/LNMO). Working distance 10 mm and acceleration voltage 5 kV.

Figure 4.6 presents the results obtained from an EDX mapping to investigate the chemical composition of the pristine LNMO, R6T10-C/LNMO, and R6T10-C/LNMO powders. A strong O (green), Mn (yellow), and Ni (turquoise) were detected for all samples, confirming that this is the LNMO particle. No carbon (red) was detected on the pristine LNMO samples. For the R6T10-C/LNMO and R6T20-C/LNMO particles, on the other hand, a relatively uniformly dispersed carbon signal was detected in the same area the as the LNMO particle was confirmed. This confirmed that a carbon layer had been formed during the hybridizing process and that it was relatively evenly dispersed on the LNMO particles.

Despite the relatively even dispersion of carbon on the surface of the LNMO particle, creating a completely uniform coating remains challenging due to the uneven surface of the LNMO particle, as seen from the carbon-coated particles and cross-section SEM images.

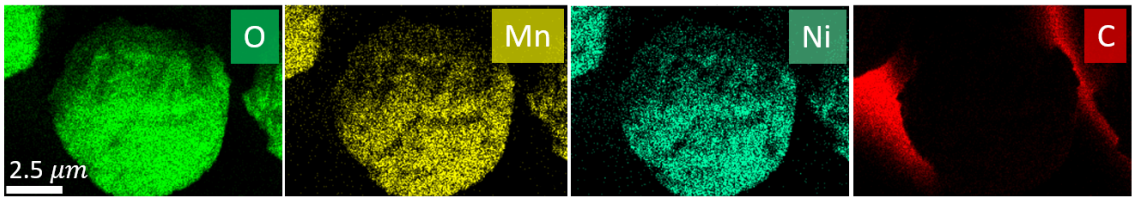


(a) Pristine LNMO

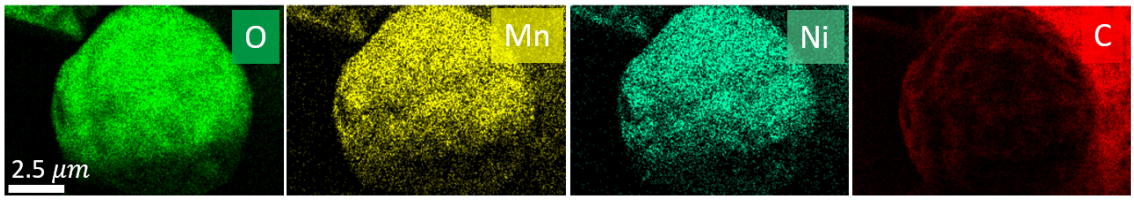


(b) R6T10-C/LNMO

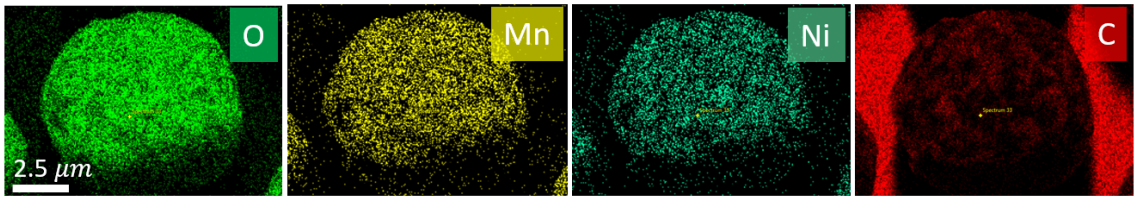


(c) R6T20-C/LNMO

Figure 4.6: EDX mapping of the (a) pristine LNMO particle, and particles hybridized with 99 wt% LNMO and 1.0 wt% CB powders at 6000 rpm for (b) 10 minutes (R6T20-C/LNMO), and (b) 20 minutes (R6T20-C/LNMO). Working distance 10 mm and acceleration voltage of 10 kV.

An XRD analysis was conducted to examine if the LMNO crystal structure was affected by the hybridizing process and/or the carbon coating. The results obtained from the XRD analysis for the pristine LNMO, R6T10-C/LNMO, and R6T20-C/LNMO are shown in Figure 4.7. All powder samples consistently displayed the characteristic peaks of the LNMO structure (denoted with black bars). This indicates that the crystal structure of LNMO was not affected by either the hybridizing process or the carbon coating.

Despite the carbon coating not being entirely uniform, and relatively thick, and that some LNMO particles were only party coated, the carbon-coated LNMO particles were regarded as sufficient for initial proof-of-concept studies. Thus, further examination of the electrochemical properties of these particles was conducted, and the obtained results are presented in the following section.

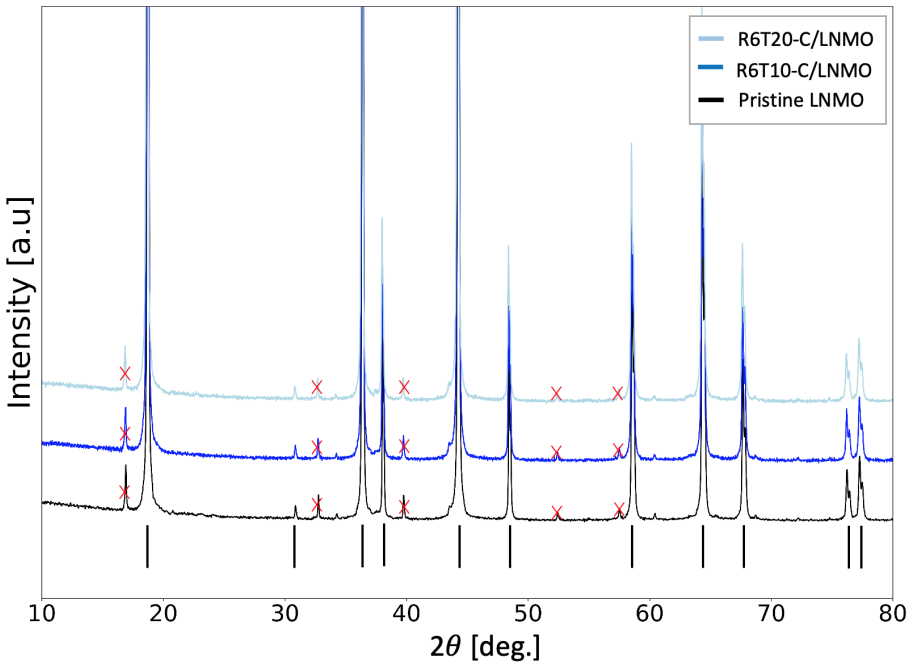


Figure 4.7: XRD diffractogram of pristine LNMO and LNMO powders carbon coated in a hybridized machine with 99 wt% LNMO and 1 wt%CB particle at 6000 rpm for 10 minutes (R6T10-C/LNMO) and 20 minutes (R6T20-C/LNMO). The black bars refer to an LNMO phase. The peaks marked with a red cross are beta-peaks which were not filtered out during the test.

### 4.1.3 Effect of carbon coating on LNMO's electrochemical performance.

The effect of the carbon coating on the electrochemical performance of LNMO was investigated through galvanostatic cycling. Figure 4.8, presents the charge-discharge profiles obtained from cycling coin half-cells between 3.0-4.95 V with LNMO, R6T10-C/LNMO, and R6T20-C/LNMO electrodes in a 1M $LiPF_6$, EC:DMC:DEC (1:1:1) electrolyte system. All cells exhibit the characteristic behavior of a disordered LNMO material, with distinctive plateaus at around 4.75 V, 4.7 V, and 4.2 V, corresponding to the $Ni^{4+/3+}$, $Ni^{3+/2+}$ and $Mn^{4+/3+}$ redox couples, respectively. Charge-discharge plots of the presented cells parallels can be found in Appendix A.

The mean initial discharge capacity and the capacity retention after 60, 80, and 100 cycles of three parallels for each the pristine LNMO, R6T10-C/LNMO, and R6T20-C/LNMO cells, are presented in Table 4.1. All cells had a similar initial discharge capacity ranging from 131-134 mAh/g. As expected, the CB in the electrodes did not contribute to the capacity, resulting in similar initial capacities across all cells. These results align with previous studies, such as Zhang et al.[15], who also observed comparable initial discharge capacities for pristine LNMO cells and carbon-coated LNMO cells. The initial discharge capacity results are also comparable to those obtained by Østli et al.[11], who used a similar LNMO powder from Haldor Topsøe. They achieved an initial discharge capacity of 136 mAh/g at C/10 for their pristine LNMO cells. Thus, in terms of initial capacity, the cells seem to function as intended.

Table 4.1: Mean initial discharge capacity and capacity retention from long-term galvanostatic cycling (GC) from three-parallel coin half-cells with pristine and carbon-coated LNMO electrodes (R6T10-C/LNMO and R6T20-C/LNMO).

| Cell. | Initial discharge cap. (mAh/g) | Cap. retention (%) 60 cycles | Cap. retention (%) 80 cycles | Cap. retention (%) 100 cycles |
|---|---|---|---|---|
| Pristine LNMO | 131 (± 1.7) | 82 | 78 | 69 |
| R6T10-C/LNMO | 134 (± 1.3) | 89 | 72 | 29 |
| R6T20-C/LNMO | 134 (± 0.7) | 88 | 81 | 66 |

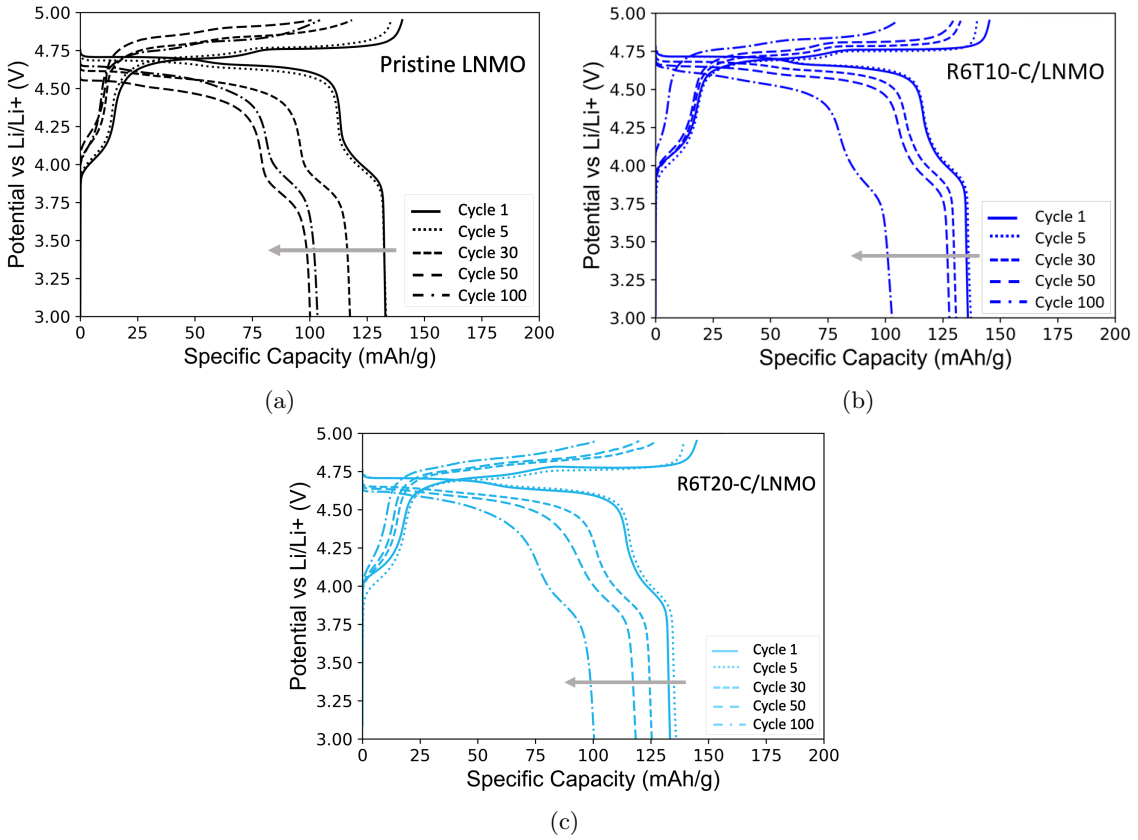


Figure 4.8: Charge-discharge plot of coin half-cells with pristine and carbon-coated LNMO electrodes (R6T10-C/LNMO and R6T20-C/LNMO). The specific capacity (mAh/g) is plotted as a function of voltage (V vs. $Li/Li^+$) for cycles 1-5 at C/20 and cycles 5-100 at C/10.

After the formation cycles, when looking at the development of an increasing number of charge-discharge cycles, all cells experienced a varying degree of capacity fade, as seen in Figure 4.9. The figure presents the mean discharge capacity of three parallel cells for each pristine LNMO, R6T10-C/LNMO, and R6T20-C/LNMO cells. When the C-rate was raised from C/20 to C/10 after the first five formation cycles, the pristine LNMO cells experienced an instant capacity fade of about 8 mAh/g. Such a capacity fade was not observed for cells with carbon-coated LNMO (R6T10-C/LNMO and R6T20-C/LNMO).

After 60 cycles, the R6T10-C/LNMO and R6T20-C/LNMO cells had capacity retention of 89% and 88%, respectively, and generally displayed better cycling stability compared to the pristine LNMO cell, which had capacity retention of 82% after 60 cycles. Differences in polarization could explain the enhanced cycling stability up to 60 cycles. A comparison of how polarization changes from the $1^{st}$ - $6^{st}$ cycle and the $1^{st}$ - $60^{th}$ cycle of the pristine LNMO, R6T10-C/LNMO, and R6T20-C/LNMO cells is presented in Figure 4.10. The arrows indicate the varying degree of polarization for the different cells. The figure shows that the pristine LNMO cell experiences a larger polarization than cells with carbon-coated LNMO particles after 6 and 60 cycles during charging and discharging. This means that a higher voltage is required for the pristine LNMO to extract and insert $Li^+$ during charge and discharge to deliver/receive a constant current. Hence, the cut-off voltage is reached earlier for the pristine LNMO cells compared to the R6T10-C/LNMO and R6T20-C/LNMO, which causes capacity losses, resulting in lower capacity retention. All cells experience an increasing degree of polarization. This is expected due to the formation of decomposition products on the electrode surface during cycling, which will cause increased surface resistance for the transport of $Li^+$ through the electrolyte-electrode interface.

After 100 cycles, the pristine LNMO, R6T10-C/LNMO, and R6T20-C/LNMO had a capacity retention of 69, 29, and 66 %, respectively. Hence, the R6T10-C/LNMO showed significantly worse cycling stability than the pristine LNMO and R6T20-C/LNMO. However, it should be mentioned that after 80 cycles, all cells showed a relatively unstable cycling performance. This is evident from the large deviation between the three parallels, as shown in Figure A.3 in Appendix A. It is also

worth noting that after 80 cycles, all cells had lost over 80 % of their initial capacity. This level of degradation is typically considered the end of life for a LIB in EVs. One possible reason for the large variety in cycling stability after 80 cycles may be the carbon coatings' large variation in coating coverage and thickness, as presented and discussed in Section 4.1.2. Another reason may be too high mass loadings or generally poor casting quality, as these factors were not the primary focus to optimize in this project.

The cycling stability of all cells presented in Figure 4.9, is generally lower than previously reported in the literature. For example, Zhang et al.[15] reported a capacity retention of 84 % and 94 % after 100 cycles at 1C for their pristine LNMO and CB-coated LNMO cells, respectively (synthesized via wet chemical method). However, before 60 cycles, the LNMO particles carbon coated with CB in the dry-coating hybridizer process still exhibits a generally improved cycling stability compared to the pristine LNMO. The R6T20-C/LNMO showed the best cycling stability of all cells up to about 90 cycles. Hence, despite the lower capacity retention, the results are consistent with previous research, indicating that carbon-coated LNMO could offer enhanced cycling stability [14, 15, 19, 59].

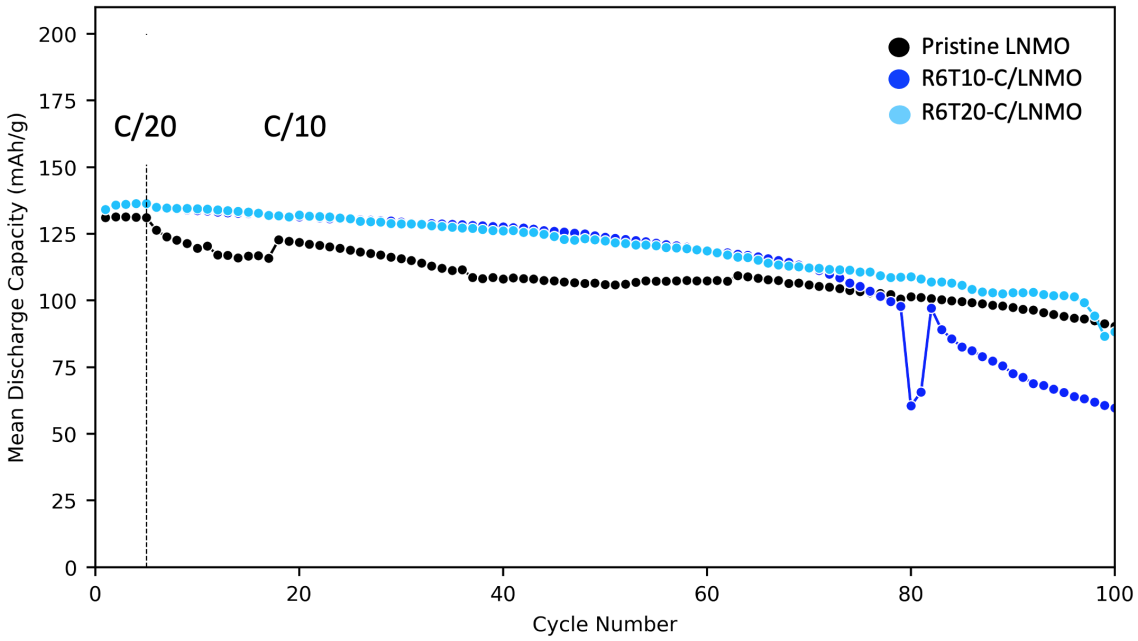


Figure 4.9: Mean specific discharge capacity as a function of cycle index of LNMO coin half-cells based on three parallels of the pristine LNMO and carbon coated LNMO electrodes (R6T10-C/LNMO and R6T20-C/LNMO). Cycles 1-5 have a C-rate of C/20, while cycles 5-100 have a C-rate of C/10.

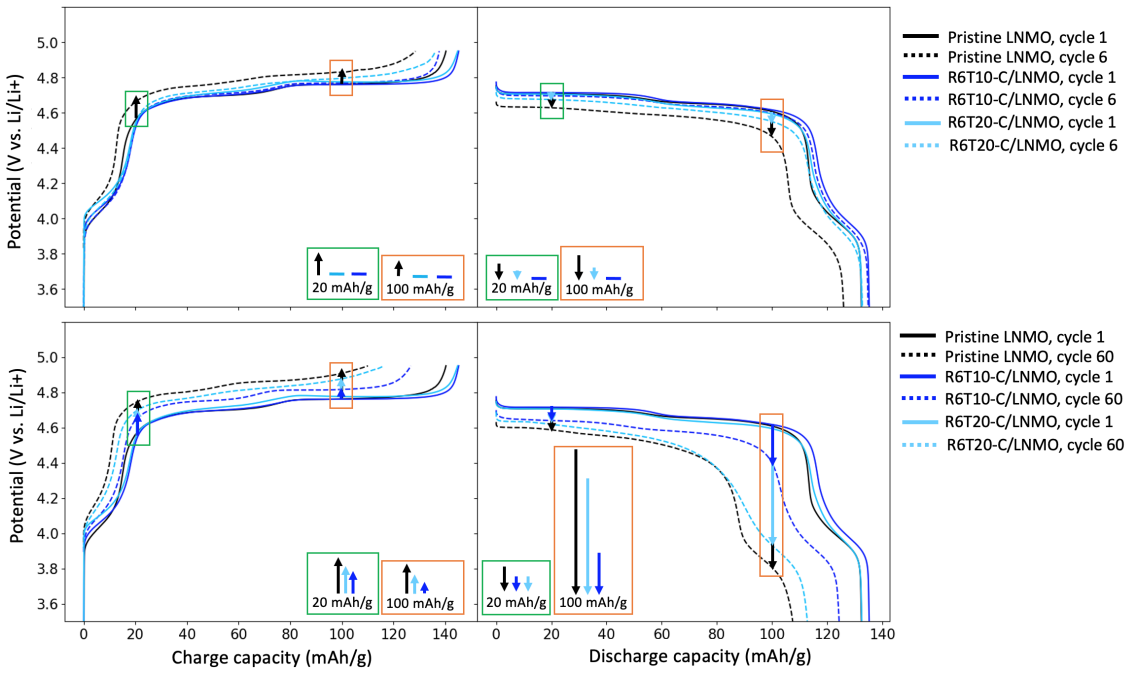


Figure 4.10: A comparison of the change in polarization between the 1st - 6st cycle and the 1st - 60th cycle of the pristine LNMO and cells with carbon-coated LNMO electrodes (R6T10-C/LNMO and R6T20-C/LNMO). The arrows present the varying degree of polarization for the different cells relative to each other at 20 and 100 mAh/g. Cycles 1 have a C-rate of C/20, while cycles 6 and 60 have a C-rate of C/10.

Looking at the mean coulombic efficiencies presented in Table 4.2, they are relatively similar for the pristine LNMO, R6T10-C/LNMO, and R6T20-C/LNMO after the formation cycles (cycle 5), and up to 100 cycles with stable values ranging from 98.6 - 99.9 %. The coulombic efficiency is slightly lower in the 1st cycle with a coulombic efficiency of 94.5, 93.5, and 92.7 % for the pristine LNMO, R6T10-C/LNMO and R6T20-C/LNMO, respectively. The lower initial coulombic efficiency may indicate that side reactions have consumed $Li^+$ during the formation of solid interphase layers (SEI and CEI), leaving less of $Li^+$ available for cycling. The slightly lower initial coulombic efficiency of the cells with a carbon-coating may indicate that a carbon coating leads to additional CEI formation. In addition, the coulombic efficiency of R6T10-C/LNMO is slightly higher than for the R6T20-C/LNMO. As discussed and presented in Section 4.1.2, a larger fraction of LNMO particles was carbon coated in R6T20-C/LNMO compared to the R6T10-C/LNMO. Hence, given that a carbon coating leads to additional CEI formation, it would be expected that cells with a larger fraction of carbon-coated LNMO particles have a lower initial coulombic efficiency. The stable colombic efficiency after the formation cycles, however, indicates that the potentially formed solid interphase layers are stable for all cells.

Table 4.2: Mean coulombic efficiency from long-term galvanostatic cycling (GC) from three-parallel coin half-cells with pristine and carbon-coated LNMO electrodes (R6T10-C/LNMO and R6T20-C/LNMO). Cycles 1-5 had a C-rate of C/20, while cycles 5-100 had a C-rate of C/10.

| Cell | Pristine LNMO | R6T10-C/LNMO | R6T20-C/LNMO |
|---|---|---|---|
| Cycle nr. | C.E (%) | C.E (%) | C.E (%) |
| 1 | 94.5 | 93.5 | 92.7 |
| 5 | 98.4 | 98.1 | 97.3 |
| 30 | 99.2 | 98.6 | 98.6 |
| 50 | 99.3 | 98.6 | 98.7 |
| 100 | 99.7 | 99.9 | 99.2 |

From long-term cycling, the cells with carbon-coated LMNO particles showed an improved rate capability when the C-rate was increased from C/20 to C/10 compared to pristine LNMO cells.

Therefore, a rate test was conducted to further investigate the carbon coating's effect on rate capability. Figure 4.11 presents the mean discharge capacity of three parallel cells for each of the pristine LNMO and R6T10-C/LNMO cell when the C-rate was incrementally increased from C/20 to 2C, and then returned to C/10.

During the first 15 cycles, the pristine LNMO and R6T10-C/LNMO displayed a similar mean discharge capacity of 135, 134, and 130 mAh/g at C-rates of C/20, C/10, and C/5, respectively. However, when the C-rate was increased, all cells experienced a significant capacity loss, where the pristine LNMO had a mean discharge capacity of 100.1 mAh/g (C/2), 26.1 mAh/g (1C), and 1.9 mAh/g (2C). The R6T10-C/LNMO cell displayed a slightly higher mean discharge capacity of 123.2 mAh/g (C/2), 30.7 mAh/g (1C), and 7.9 mAh/g (2C) compared to the pristine LNMO cell. After 30 cycles, when the C-rate returned to C/10, all cells restored most of their initial capacity. The generally improved rate capability for the cells with carbon-coated LNMO particles compared to pristine LNMO at higher C-rates coincide with the previous research. For instance, Zhang et al.[15] achieved a discharge capacity of 111 mAh/g and 70 mAh/g for their CB-coated and pristine LNMO cells at 5C, respectively. Similarly, Hwang et al.[19] reported a discharge capacity of 130 mAh/g at 4C for carbon nanotube-coated LNMO, using a comparable dry-coating mechano-fusion method to the hybridizer method used in this project. Their non-carbon-coated LNMO cells had a significantly lower discharge capacity of 109 mAh/g at 4C than their carbon-coated LNMO cells.

It's worth noting that the carbon coating thickness in our study varied significantly, ranging from no coating to 1.2 $\mu$m, which is significantly higher than the suggested coating thickness of 70 nm [15]. Still, the trends observed regarding cycling stability and rate capability align with previous research, suggesting the beneficial effect of carbon coating on the LNMO electrode material's performance [14, 15, 19, 59].

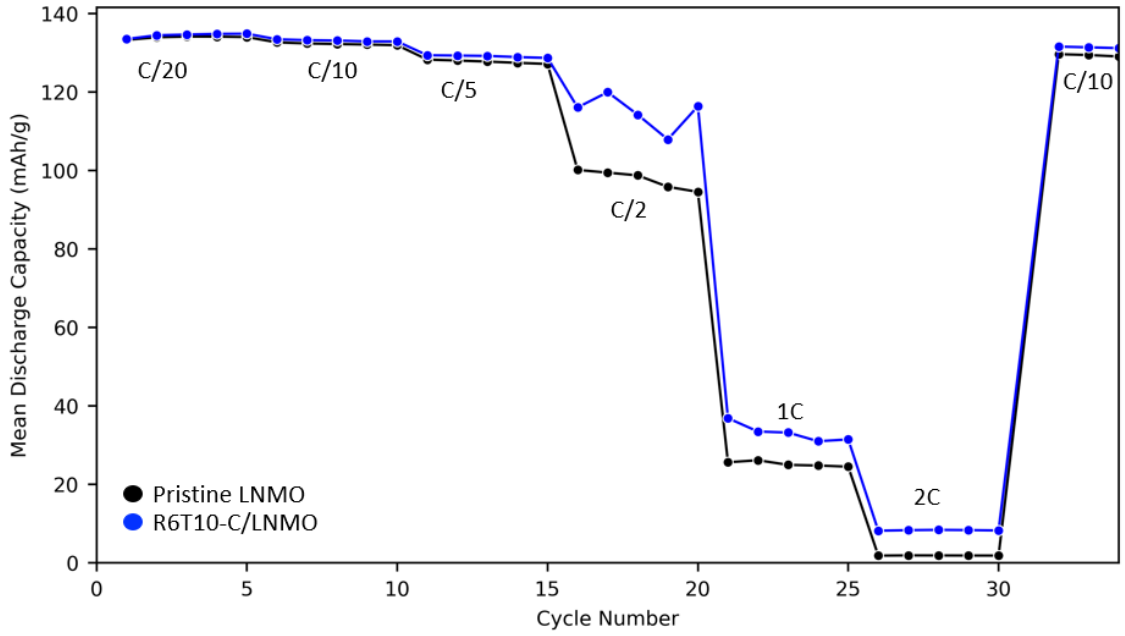


Figure 4.11: Mean specific discharge capacity of three-parallel coin half-cells with pristine and carbon-coated LNMO electrodes (R6T10-C/LNMO). The C-rate was incrementally increased from C/20 to 2C and then returned to C/10.

The reason behind the improved cycle stability and rate capability could be enhanced electrical conductivity, and/or suppression of side reactions with the electrolyte. Therefore, to examine whether the carbon coating resulted in an improved electrical conductivity of the LNMO electrode, an ICI test was conducted to measure how the resistance varied with the state of charge (SOC). Figures B.3, 4.13, and 4.14 present the changes in voltage upon charge and discharge, along with the corresponding change in total resistance as a function of SOC for the pristine LNMO, R6T10-C/LNMO, and R6T20-C/LNMO cells, respectively. Parallels of the presented cells can be found in Appendix B.

At a SOC between 35 and 95 %, both the pristine LNMO, R6T10-C/LNMO, and R6T20-

C/LNMO display a relatively stable and similar resistance ranging from 55 - 85 Ω. At the beginning of the charge and end of the discharge, between 5 and 35 % SOC, the resistance generally drops with an increasing number of cycles for all cells. In the pristine LNMO cell, the resistance drops from around 300-200 Ω at the beginning of charge and 200-160 Ω at the end of discharge. In addition, the resistance is very unstable. The carbon-coated LNMO cells, on the other hand, exhibit a lower and more stable resistance in the same SOC range. Specifically, the R6T10-C/LNMO cell has a resistance of about 135-70 Ω at the beginning of charge and 100-70 Ω at the end of discharge, while the R6T20-C/LNMO cell has a resistance of about 155-110 Ω at the beginning of charge and discharge. Since the bulk electrolyte's ionic resistance and the resistance of current collectors and separators should be independent of the SOC, it is reasonable to assume that the observed resistances are due to the transport of $Li^+$ through the electrode-electrolyte interface and charge transfer. Unless other chemical reactions are occurring at the pristine LNMO, the carbon coating should result in an increased resistance upon intercalation. Therefore, if resistance related to the transport of $Li^+$ through the electrode-electrolyte interface were the main contributor to the resistances observed, the LNMO with carbon coating should display a higher resistance than the pristine LNMO. Therefore, the lower and more stable resistance of the coated LNMO particles compared to the pristine LNMO between 5 and 35 % SOC may indicate that the carbon coating has led to enhanced electronic conductivity. In addition, the carbon coating may also have led to better electrical contact between the LNMO particles and the current collector, which as discussed in Section 2.8, is commonly observed for carbon-coated LFP electrodes. Thus, the improved rate capability and cycling stability of the carbon-coated LNMO cells may be attributed to improved electronic conductivity, allowing for better utilization of the AM capacity at higher C-rates and faster charge transfer between the current collector and the LNMO particles. Zhang et al. [15] reported similar trends regarding enhanced electronic conductivity for a carbon black-coated LNMO material from an EIS measurement after 100 cycles at 0.2C charge rate and 1C discharge rate. They achieved a charge transfer resistance of 114 Ω for their pristine LNMO cells, which was substantially reduced to 55.4 Ω for the cell containing carbon-coated LNMO. However, it is important to note that a direct comparison of resistance values from our and Zhang et al. [15] studies may be misleading due to potential differences in material loading. In addition, they conducted an EIS measurement and not an ICI test. Nevertheless, the observed trends regarding charge transfer resistance are still valid for comparison. Furthermore, as the charge transfer is strongly connected to the surface resistance [15, 14], the carbon coating may have suppressed surface resistance caused by side reactions between the electrolyte and the LNMO electrode. However, the carbon coatings' protective effect against the dissolution of TMs remains unclear as the cycling stability was relatively unstable above 80 cycles for all cells. If the dissolution of TMs had been suppressed, improved cycling stability would have been expected for the carbon-coated LNMO cells. Therefore, further investigation is necessary to determine the extent of TM dissolution. For example, the deposition of Ni and Mn on the counter electrode should be examined.

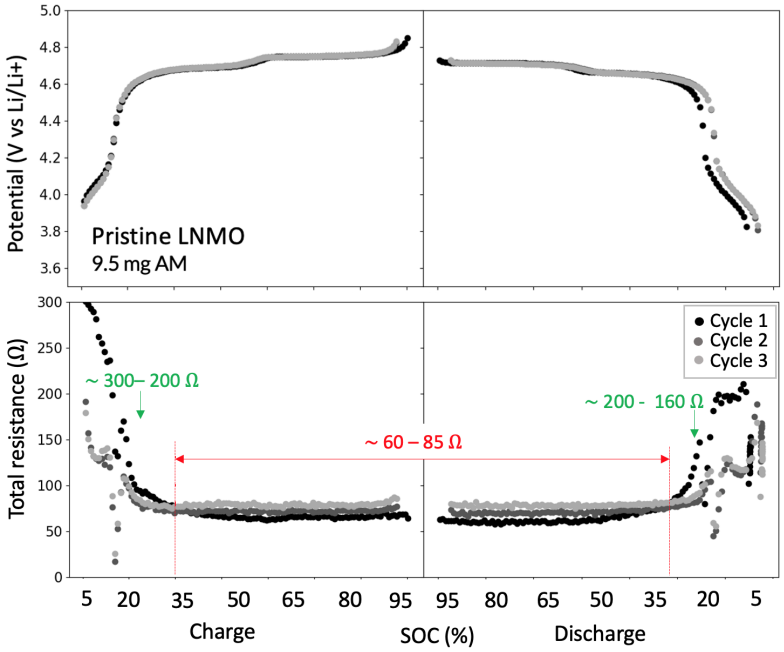


Figure 4.12: The change in voltage with the corresponding change in total resistance as a function of the state of charge (SOC) from intermittent current interruption (ICI) tests of coin half-cells with a pristine LNMO electrode.

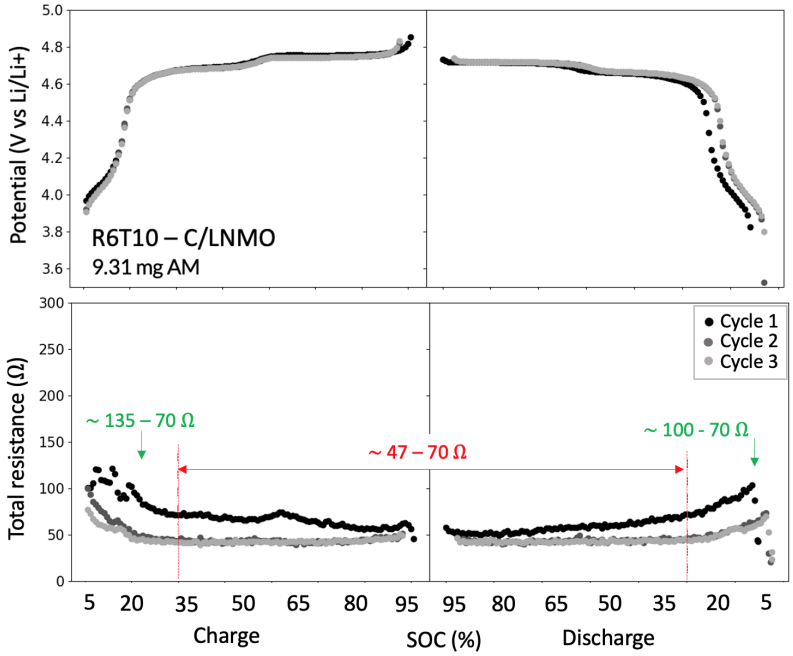


Figure 4.13: The change in voltage with the corresponding change in total resistance as a function of the state of charge (SOC) from intermittent current interruption (ICI) tests of coin half-cells with a carbon-coated LNMO electrode (R6T10-C/LNMO).

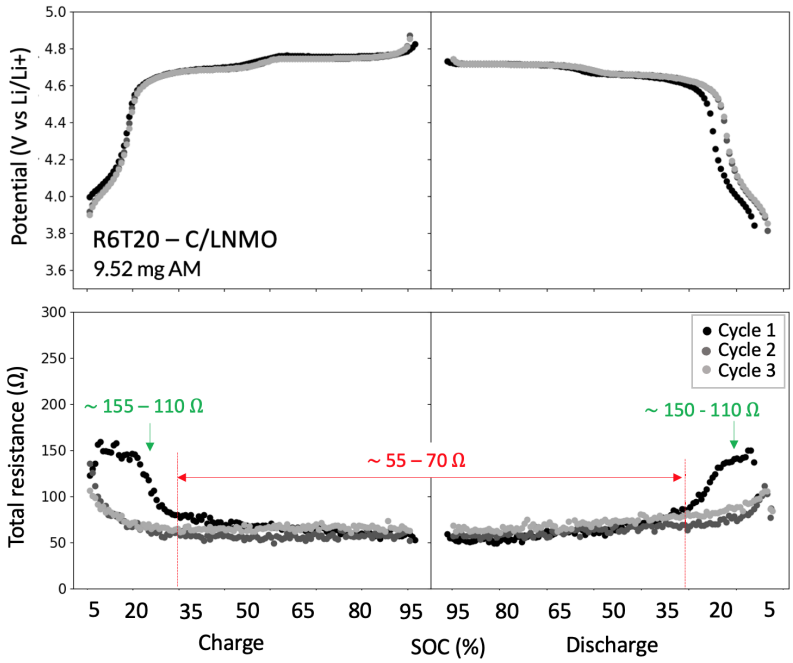


Figure 4.14: The change in voltage with the corresponding change in total resistance as a function of the state of charge (SOC) from intermittent current interruption (ICI) tests of coin half-cells with a carbon-coated LNMO electrode (R6T20-C/LNMO).

To summarize, despite the relatively thick and non-uniform carbon coating, improved cycling stability compared to the non-coated LNMO particles was observed up to 60 cycles. This observation indicates that the carbon coating may have facilitated better utilization of AM, improved the electrical contact between the LNMO particles and the current collector, and/or acted as a protective barrier toward the electrolyte. The improved electrochemical performance despite the non-optimized carbon coating suggests that further optimization, particularly in terms of coating thickness and uniformity, could lead to even better results. However, as a proof of concept, the electrochemical performance of the carbon-coated LNMO particles was regarded as sufficient. The next part of the project investigates whether the carbon-coated LNMO particles could help create a more uniform PPy layer on the LNMO electrode during an in-situ electropolymerization of Py.

## 4.2 In-situ formation of a PPy coating via CV

### 4.2.1 Al and C-Al electrodes

To gain an understanding of PPy layer formation without interference from LNMO particles, Py was first electropolymerized onto an Al electrode via CV. Figure 4.15 presents the voltammograms obtained from cycling three-electrode cells in a 1M $LiPF_6$, EC:DEC:DMC (1:1:1) electrolyte system without and with 0.5 wt% Py additive. Upon the positive scan, the potential was swept to 4.1 V to avoid disturbance from any possible electrolyte decomposition on the final PPy-layer, which may occur if the potential exceeds 4.3 V. During the positive scan, the Al cell containing 0.5 wt%Py electrolyte additive experienced a significant current increase at about 3.8 V for all cycles. This potential corresponds to the expected electropolymerization potential of Py, which was previously confirmed in work done by the author, see Appendix C. In the $1^{st}$ cycle, the current continued to increase until it reached a current density of about 1.0 $mAh/cm^2$ at around 4.0 V. For the subsequent cycles, the current density corresponding to the oxidation peaks gradually decreased with an increasing number of cycles. This may indicate that more and more Py had been consumed during each cycle. The cell without the Py additive did not experience such a current increase, which further indicates that the Py has been electropolymerized to form PPy on the Al working electrode in the cell containing Py additive. The CV curves for the cell containing 0.5 wt%Py electrolyte additive are rough, and small current drops are observed in each cycle. These drops may imply that the cell experiences many small partial short circuits. One possible explanation

for these drops is that the polymer grows through the separator's pores and touches the anode, resulting in a current drop that is subsequently restored. Given that a PPy-layer has been deposited on the Al working electrode, a reduction peak should be present during the reverse scan as the PPy layer should be electrochemically active. However, the noisy CV curves make it challenging to determine whether this reduction peak is present. Therefore, the electrochemical reversibility of the PPy layer remains uncertain.

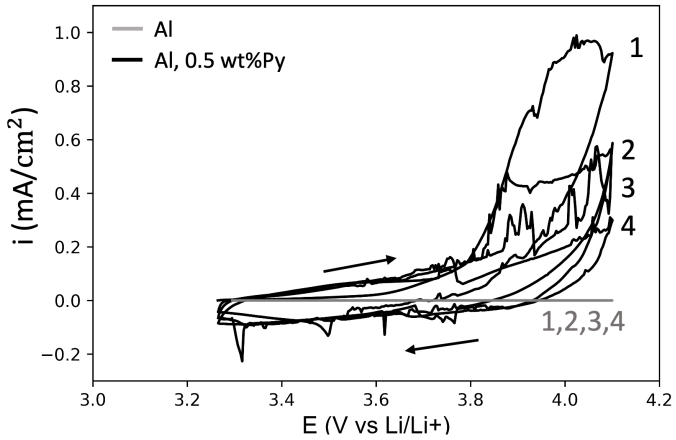


Figure 4.15: Voltammograms of three-electrode cells with Al as counter and working electrode and Li as reference electrode, with a 1M $LiPF_6$ EC:DMC:DEC (1:1:1) electrolyte system, both without (grey curve) and with 0.5 wt%Py additive (black curve). The cells were swept from 0 V vs. OCV to 4.1 V vs. $Li/Li^+$, followed by a reverse sweep to 0 V vs. OCV, for a total of four cycles.

To investigate whether a PPy layer formed on the electrode surface during CV, the surface morphology of the Al working electrode from the three-electrode cell containing 0.5 %Py additive was examined, as shown in Figure 4.16. The electrode surface had several areas where PPy seemed to have been deposited, as seen from the overview SEM image at a magnification of x160. The observed layer displays the characteristic PPy cauliflower-like structure (magnification of x5000), which is typical if the coating thickness exceeds 1000 nm [13]. These findings strongly indicate that a PPy layer formed during the CV process. However, the layer was not uniform, which may be due to the cleanliness of the Al surface and/or variation in the surface energy due to the polycrystallinity of the Al electrode. It is also possible that some polymer peeled off when the separator was removed during cell disassembly.

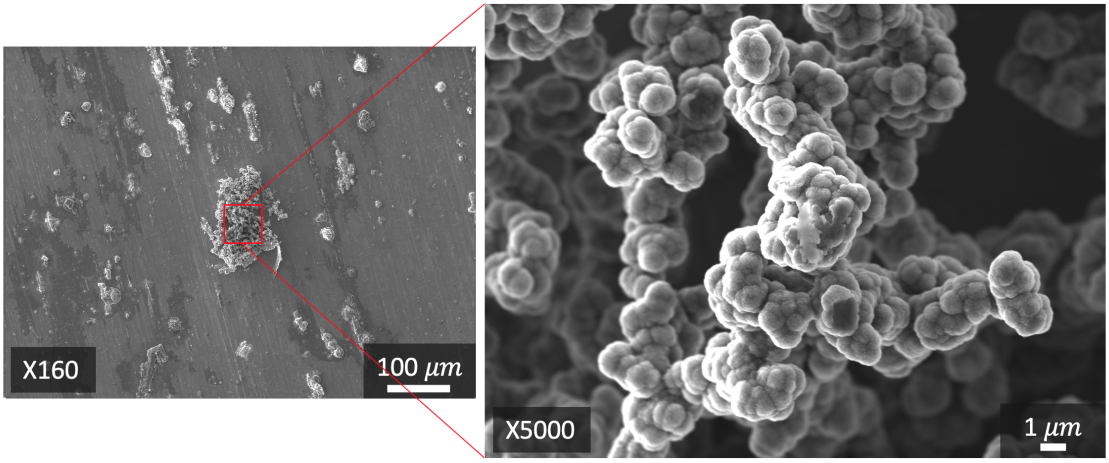


Figure 4.16: SEM images of an Al working electrode from a three-electrode cell containing 0.5 %Py electrolyte additive post mortem cyclic voltammetry where the cell was swept from 0 V vs. OCV to 4.1 V vs. $Li/Li^+$, followed by a reverse sweep to 0 V vs. OCV, for a total of four cycles. Working distance of 10 mm and an acceleration voltage 5 kV.

As the CV of three-electrode cells using Al as both the working and counter electrode strongly indicated the formation of a PPy-layer on the working electrode with a cauliflower-like structure, a carbon-coated Al electrode was implemented as the working electrode with the aim to create a more uniform PPy-layer. The voltammograms obtained from cycling three-electrode cells in the same electrolyte system as for the Al-Al three-electrode cells are presented in Figure 4.17. In addition to doing a positive potential sweep to 4.1 V (Figure 4.17a), the cells were also swept to 4.9 V (Figure 4.17b), which is the operating voltage of LNMO-based cells. This was done to investigate if there were any distinct differences in the PPy layer formed below and above the decomposition voltage of the electrolyte (4.3 V).

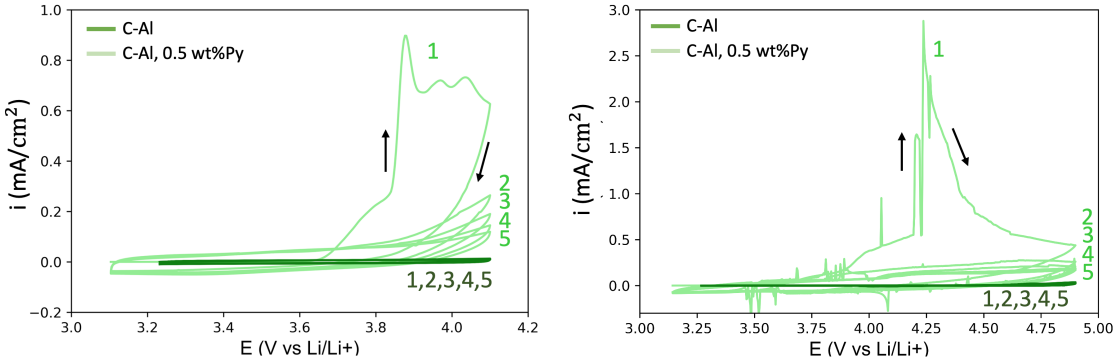


Figure 4.17: Voltammograms of three-electrode cells with Li as reference electrode, Al as counter electrode and carbon-coated Al (C-Al) as the working electrode, with a 1M $LiPF_6$ EC:DMC:DEC (1:1:1) electrolyte system without (dark green curve) and with 0.5 wt%Py additive (light green curve). The cells were swept from 0 V vs. OCV to (a) 4.1 V vs. $Li/Li^+$ and (b) 4.9 V vs. $Li/Li^+$, followed by a reverse sweep to 0 V vs. OCV, for a total of four cycles.

From Figure 4.17a in the 1$^{st}$ cycle for the cell containing 0.5 wt %Py, the current significantly increases when reaching a potential of about 3.7-3.8 V and continues to rise until it reaches a current density of about 0.9 mA/cm$^2$ around 3.9 V. This trend is not observed in the subsequent cycles, indicating that all Py additive may have been consumed during the 1$^{st}$ cycle. No oxidation peaks are observed in the cell without Py additive, which further strengthens the indication of Py being electropolymerized in the cell containing the Py additive. A similar trend is observed in Figure 4.17b until the potential reaches about 4.1 V during the positive potential scan. When the potential is further increased past 4.1 V, the current increases, resulting in an oxidation peak at around 4.3 V with a corresponding current density of about 3.0 mA/cm$^2$. Although this peak might have been attributed to electrolyte decomposition, the fact that it is absent in the sample without Py makes this explanation unlikely. Therefore, it is plausible that this peak is a result of either ongoing PPy growth or overoxidation of the PPy layer. No distinct PPy reduction peaks are observed in any of the voltammograms (Figure 4.17), and the electrochemical reversibility of the suspected PPy layer formed remains uncertain.

To investigate whether a uniform PPy layer had formed on the C-Al working electrode surface during CV, and to identify differences in surface morphology of the cells swept to 4.1 V and 4.9 V, the working electrodes of the cells presented in Figure 4.17 were examined post-mortem. Figure 4.18 shows the SEM images of the C-Al electrodes.

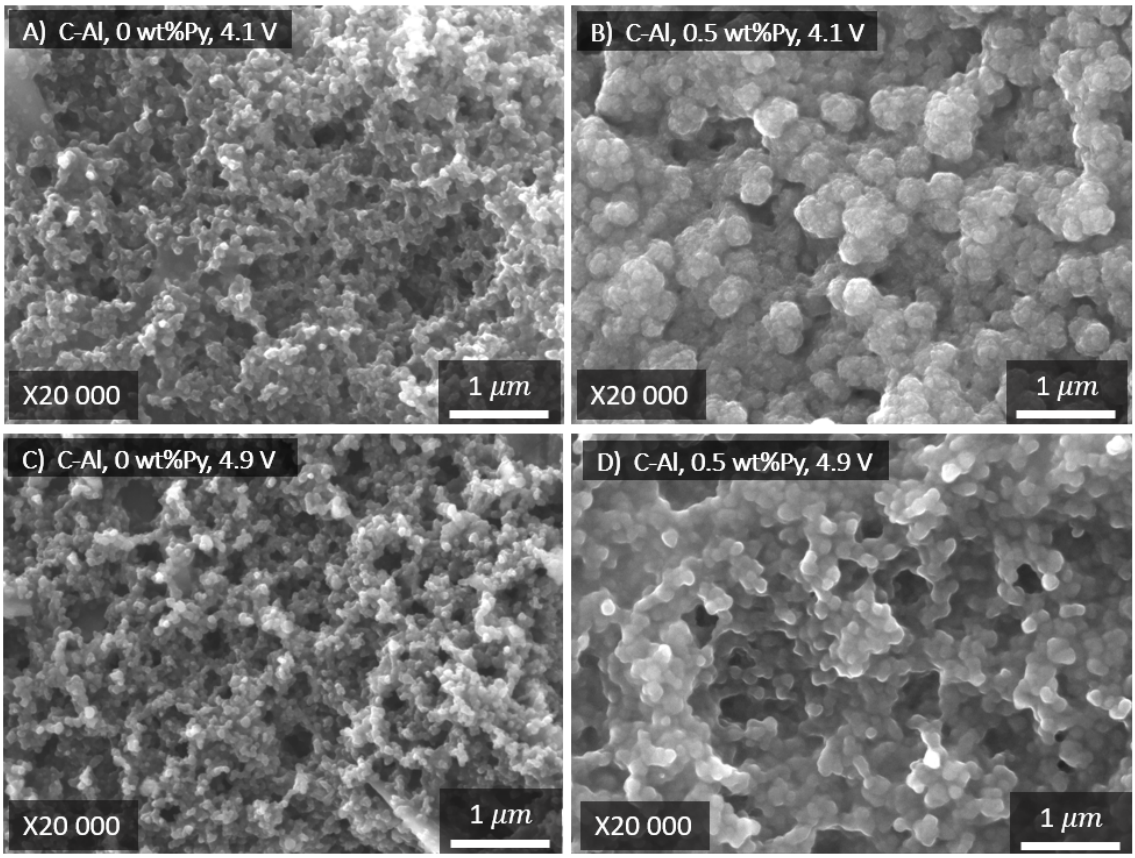


Figure 4.18: SEM images of C-Al working electrodes from three-electrode cells post-mortem cyclic voltammetry, where the cells were swept from 0 V vs. OCV to (A) 4.1 V vs. $Li/Li^+$ without Py additive, (B) 4.1 V vs. $Li/Li^+$ with 0.5 wt% Py additive, (C) 4.9 V vs. $Li/Li^+$ without Py additive, and (D) 4.9 V vs. $Li/Li^+$ with 0.5 wt% Py, for a total of four cycles. Working distance of 10 mm and an acceleration voltage of 5 kV.

A distinct difference in surface morphology between the C-Al electrodes swept to 4.1 without and with Py can be observed. Specifically, the C-Al electrode with 0.5 wt% Py displays a cauliflower-like structure similar to that found when electropolymerizing Py onto the Al-electrode, as shown in Figure 4.16. However, unlike the PPy layer on the Al-electrode, the PPy layer on the C-Al electrode appears to be uniform, as no areas similar to those observed on the C-Al electrode without the Py additive are visible. This suggests that a carbon coating might help in creating a more uniform PPy-layer. There is also a clear difference in the surface morphology between the C-Al electrodes swept to 4.9 without and with Py. However, the surface morphology of the C-Al with Py appears different from that with Py swept to 4.1 V, as the characteristic cauliflower-like structure is not observed. Still, chains seem to have formed between the carbon particles together with a generally increased particle size compared to the C-Al without Py swept to 4.9 V, indicating that a PPy-layer is formed. The layer also appears uniform. Comparing the C-Al electrodes swept to 4.1 V and 4.9 V without the Py additive, a slight difference in their surface can also be observed. This may suggest that the electrolyte decomposition products have deposited on the C-Al electrode or that the carbon reacted with the electrolyte when the potential was swept to 4.9 V. Thus, the differences between the C-Al with Py swept to 4.1 V and 4.9 V may be due decomposition products of the electrolyte, and/or the PPy-layer itself being overoxidized or decomposed. How this change affects the electrochemical properties of the PPy-layer is uncertain.

A Raman analysis was conducted to verify the presence of the PPy-layer and to obtain information about its chemical composition. The Raman spectra of the Al and C-Al electrode surfaces after CV for the cells swept to 4.1 V are presented in Figure 4.19, including their corresponding location on the sample denoted by a red cross. For the C-Al sample (dark green curve) without the Py additive, two peaks were detected at a frequency of about 1600 and 1350 $cm^{-1}$. The peak at 1600 $cm^{-1}$ may be attributed to the vibration of carbon atoms in a graphite layer [69], while

the peak at 1350 $cm^{-1}$ confirms that the carbon has an amorphous structure as this peak can be ascribed to structural disorder near the edge of graphite-like domains. The characteristic peaks of PPy, as presented in Table 2.3, were detected on both electrodes containing the Py additive (black and light green curve) as denoted in the spectra. The peak at 1600 $cm^{-1}$, may be attributed to the stretching of C=C in the PPy backbone. This peak has the highest intensity compared to the other peaks, which aligns with previously reported literature [70, 71]. From the double peaks at 1050, 1080 $cm^{-1}$ and 1320,1380 $cm^{-1}$, the peaks at 1080 and 1380 indicate that PPy has been oxidized. The peak at 1080 $cm^{-1}$ can be ascribed to ring stretching vibration, while the peak at 1380 $cm^{-1}$ can be attributed to C-H in-plane deformation. Furthermore, the peaks at 940 and 990 $cm^{-1}$ may be linked to ring deformation associated with di-cations and radical cations, respectively. Lastly, Varde et.al [71] electropolymerized Py onto a platinum plate, where they used Tetrabutylammonium hexafluorophosphate (TBAPF6) as both the solvent and the dopant ($PF_6$), and from Raman analysis, they argued that the peak observed at 1240 $cm^{-1}$ might be attributed C=C stretching. As a similar anion dopant was used in this project (originating from the $LiPF_6$ salt), the peak observed at 1240 $cm^{-1}$ might also be attributed to C=C stretching.

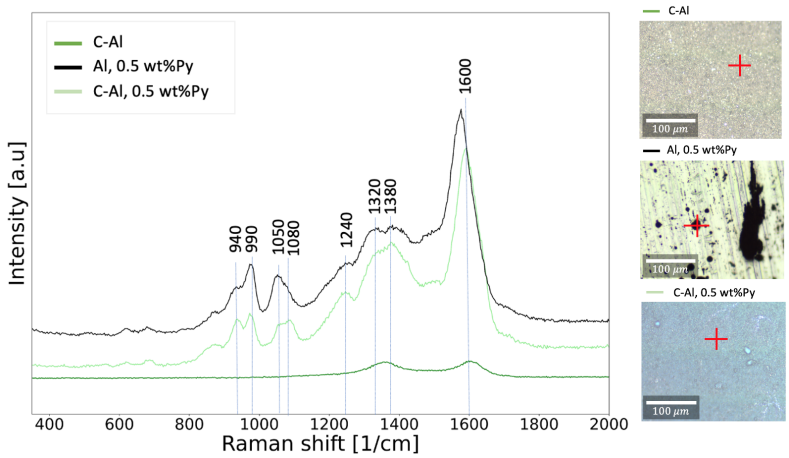


Figure 4.19: Raman spectra of Al and C-Al electrode surfaces post-mortem CV with and without Py, where the three-electrode cells had been swept from 0 V vs OCV to 4.1 V vs $Li/Li^+$, followed by a reverse scan back 0 V vs OCV, for a total of four cycles. The microscope images present the corresponding testing sites denoted by a red cross.

As all expected PPy peaks were detected in the Raman spectra from the Raman analysis, this strongly suggests the presence of a PPy-layer on the surface of the electrodes in Figures 4.16 and 4.18 from the cells containing Py additive. The SEM images of the C-Al electrode (Figure 4.18), also provide evidence that a carbon coating may result in a more uniform PPy coating. Furthermore, it appears that the PPy layer changes at high operating voltages (4.9 V), but its effect on the PPy coating's electrochemical properties is still uncertain. The following section investigates whether similar trends can be observed when using carbon-coated LNMO electrodes.

### 4.2.2 LNMO electrodes

Building on the strong indications of a PPy-layer being formed on the Al and C-Al electrode surfaces in the above presented and discussed results, pristine LNMO and carbon-coated LNMO was now implemented as the working electrode. Figure 4.20 shows the voltammograms obtained from cycling three-electrode cells in the same electrolyte system and with similar potential scans as for the C-Al three-electrodes in Figure 4.17.

From the zoomed-in section (black curves) of the pristine LNMO electrodes without Py (Figure 4.20a), when the potential was swept in a positive direction, oxidation peaks can be seen at about 4.2 V and 4.7 V with corresponding current densities of about 0.5 $mA/cm^2$ and 1 $mA/cm^2$, respectively. From the reverse potential scan, reduction peaks can be observed at about 4.4 V and 3.7 V. The 4.2 V and 3.7 V peaks can be ascribed to the $Mn^{4+/3+}$ redox couple. As shown in Figure 2.9b, in a disordered LNMO structure it is expected to see two oxidation peaks at 4.7 V and 4.75 V and two reduction peaks at 4.5 V and 4.4 V which can be ascribed to the $Ni^{4+/3+}$

and $Ni^{3+/2+}$ redox couples. Therefore, in the oxidation peak at 4.7 V and in the reduction peak at 4.4 V, there is most likely an overlap between the peaks attributed to the $Ni^{4+/3+}$ and the $Ni^{3+/2+}$ redox couples. For the R6T10-C/LNMO cell without Py (Figure 4.20b), oxidation peaks are observed at about 4.2 V and 4.7 V, and reduction peaks are observed at about 4.4 V and 3.7 V with current densities similar to those of the pristine LNMO cell. The peak at 4.2 V is less distinct than for the pristine LNMO cell, indicating that the carbon coating may have some influence on the oxidation of $Mn^{4+/3+}$. However, its reduction peak at about 3.7 V is still present and the carbon-coating does not seem to have influenced the reversibility of the cell.

When the potential was swept to 4.1 V a distinct electropolymerization peak is observed around 3.7-3.8 V in all cells containing the Py additive (Figure 4.20). This peak was not observed in any of the cells without Py or in subsequent cycles, which indicates that Py has been electropolymerized to form PPy and that all Py was consumed during the 1st cycle. This behavior aligns with the previously observed results in the C-Al cell presented in Figure 4.17. When the potential was further increased from 4.1 to 4.9 V in the pristine LNMO cell with the Py additive (Figure 4.20a), the current continued to increase, reaching a current density of 12 $mA/cm^2$ at the upper limit. At a similar potential increase in the R6T10-C/LNMO cell with Py additive (Figure 4.20b, a similar current increase was observed as for the pristine LNMO cell in Figure 4.20a. However, it had a maximum current density of 1.1 $mA/cm^2$ when reaching about 4.5 V. After the 1st cycle both cells seem to short-circuit. One possible explanation for this may be that the PPy has grown through the separator leading to an electrical contact between the anode and the cathode, which resulted in a short-circuit. Regarding the contribution from the LNMO redox reaction for the cells containing Py, it is challenging to distinguish the $Mn^{4+/3+}$ and $Ni^{4+/3+}$ red-ox couple peaks due to the simultaneous electropolymerization process of Py.

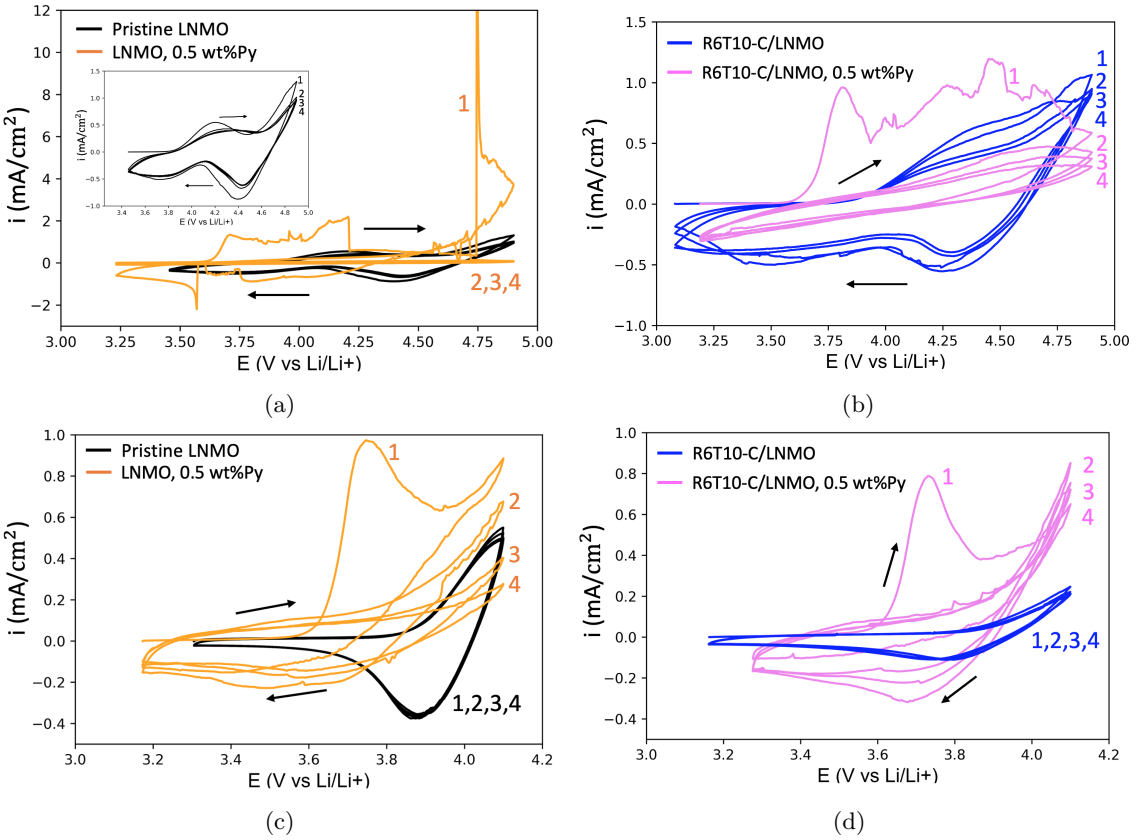


Figure 4.20: Voltammograms of three-electrode cells with a 1M $LiPF_6$ EC:DMC:DEC (1:1:1) electrolyte system with and without 0.5 wt%Py additive. The cells were swept from 0 V vs. OCV to (a) 4.9 V vs. $Li/Li^+$ with a pristine LNMO electrode, (b) 4.9 V vs. $Li/Li^+$ with a carbon-coated LNMO electrode, (c) 4.1 V vs. $Li/Li^+$ with a pristine LNMO electrode, and (d) 4.9 V vs. $Li/Li^+$ with a carbon-coated LNMO electrode, followed by a reverse sweep to 0 V vs. OCV, for a total of four cycles.

In order to determine whether a uniform PPy layer had formed on the carbon-coated LNMO electrode after the positive potential scan to 4.1 V, the LNMO electrodes from the cells presented in Figure 4.20c and 4.20d were examined post-mortem. The resulting SEM images, including SEM images of uncycled electrode casts, are presented in Figure 4.21. The LNMO particles can be recognized from their spherical shape, and the smaller particles on top and surrounding the LNMO particle are the binder and the CB additive. When comparing the pristine LNMO without (black bar) and with the Py (yellow bar), the surface morphology of the LNMO particle itself appears relatively similar. However, in the areas containing CB in the pristine LNMO electrode with Py, chains seem to have formed between the particles, resulting in "clusters" of connected particles with increased particle size. This may suggest that PPy had a preferential growth in carbon-rich areas leading to a non-uniform coating, which was expected based on previous work in the Specialization project during the fall of 2022. Comparing the uncycled R6T10-C/LNMO with the R6T10-C/LNMO electrode (blue bar), their surface morphology appears different. It may look like the electrolyte has reacted with the carbon-coating on the surface of the LNMO particle. The results from the galvanostatic cycling test in Section 4.1.3, also suggested that a side reaction may take place between the carbon-coating and the electrolyte due to the lower initial coulombic efficiency in the cells with carbon-coated LNMO compared to the cells with pristine LNMO. However, in future work, further investigation on the chemical composition of the electrode surface should be investigated via X-ray photoelectron spectroscopy (XPS) to confirm this. A distinct difference is observed between the R6T10-C/LNMO electrode containing Py (pink bar) and the R6T10-C/LNMO electrode without Py (blue bar). A relatively smooth and uniform layer, which is assumed to be the PPy-layer, seems to have formed on top of LNMO particles with carbon coating. Such a layer is not observed on the pristine LNMO electrode with Py. Similar to the pristine LNMO electrode without Py, the PPy-layer on the R6T10-C/LNMO electrode also appears to have deposited on the CB additive in between the LNMO particles. Given that this is the case, this may indicate that an in-situ electropolymerization of Py onto carbon-coated LNMO could allow for a uniform PPy-coating on both the CB additive and the LNMO particles, which was the initial idea behind this project as illustrated in Figure 1.1. However, the suspected PPy-layer on the R6T10-C/LNMO electrode (pink bar) does not display the characteristic cauliflower-like structure previously observed on the C-Al electrode in Figure 4.18B. As the operating conditions during the CV scan were identical, the reason for the difference in surface morphology is unclear. A possible explanation may be that the morphology of the carbon coating on the Al electrode and the carbon coating on the LNMO particle was different and that the PPy-layer partly adapts the structure of the underlying coating.

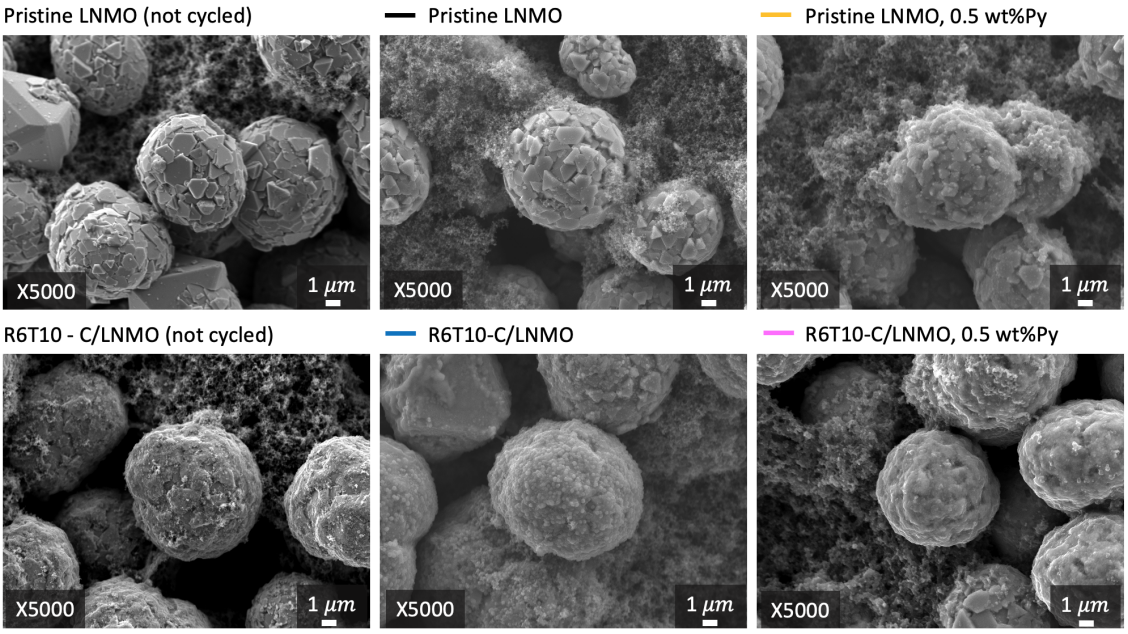


Figure 4.21: SEM images of uncycled electrode casts and pristine LNMO electrodes and carbon-coated electrodes (R6T10-C/LNMO) with and without Py additive, where the three-electrode cells had been swept from 0 V vs. OCV to 4.1 V vs. $Li/Li^+$, followed by a reverse scan back 0 V vs. OCV, for a total of four cycles.

To confirm the presence of the PPy layer and investigate any potential effects of the LNMO and carbon-coated LNMO on its chemical composition, a Raman analysis was conducted. Figure 4.22 displays the Raman spectra obtained from the surfaces of the pristine LNMO and carbon-coated LNMO electrodes post-mortem CV from cells swept to 4.1 V. In Figure 4.22a, the measurement was taken on top of the LNMO particles, while in Figure 4.22b the test was taken in between the LNMO particles. The corresponding testing site for each electrode sample is presented in Figure 4.23, where the red cross refers to testing site 1 (Figure 4.22a) and the black cross refers to testing site 2 (Figure 4.22b).

In Figure 4.22b, five peaks are detected at a frequency of about 166, 410, 500, 600, and 650 $cm^{-1}$. These peaks correspond to the disordered LNMO structure (see Table 2.3), confirming that the Raman analysis was conducted on top of the LNMO particles. The R6T10-C/LNMO electrode (blue curve) exhibited the characteristic CB peaks at around 1600 and 1350 $cm^{-1}$, indicating the presence of a CB coating on the LNMO particles. The presence of a CB coating was further confirmed as the CB peaks were not detected on the pristine LNMO electrode surface. Additionally, for all electrodes containing Py the characteristic PPy peaks presented in Table 2.3 are detected, suggesting that a PPy layer has formed on top of the LNMO particles. The attribution of the different characteristic PPy peaks has already been discussed in Section 4.2.1. However, these results do not reveal any information about the uniformity of the layer, as the PPy layer was found on both the pristine and carbon-coated LNMO particles' surfaces. Nevertheless, the SEM images suggest that the PPy layer is more uniformly distributed on the carbon-coated LNMO particles compared to the pristine LNMO particles. In Figure 4.22b, only the characteristic CB peaks at about 1600 and 1350 $cm^{-1}$ were detected on the pristine LNMO and R6T10-C/LNMO electrode surface. For the electrodes containing Py, on the other hand, the characteristic PPy peaks were detected. This may confirm that a PPy-layer has been deposited on the CB additive as suggested from the SEM images in Figure 4.21. As no LNMO peaks were detected, it can be assumed that the Raman analysis was conducted in an area in between the LNMO particles.

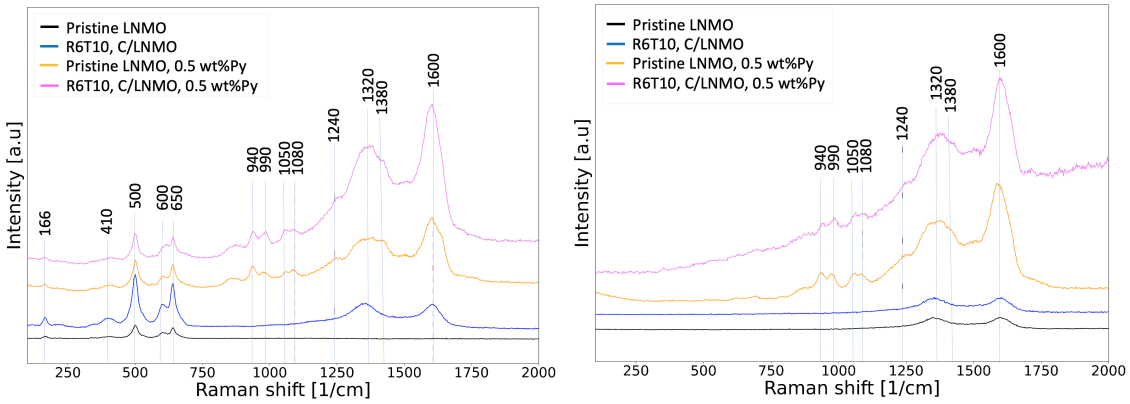


(a) site 1

(b) site 2

Figure 4.22: Raman spectra of pristine and carbon coated LNMO electrodes (R6T10-C/LNMO) post-mortem cyclic with and without Py, where the three-electrode cells had been swept from 0 V vs OCV to 4.1 V vs Li/Li$^+$, followed by a reverse scan back 0 V vs. OCV, for a total of four cycles. The test was taken in (a) on top of an LNMO particle and (b) between the LNMO particles.

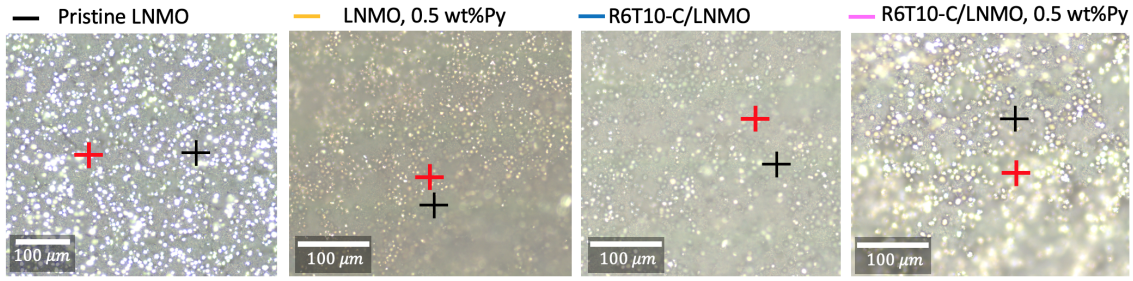


Figure 4.23: Microscope images presenting the testing site corresponding to the Raman spectras in Figure 4.22. The red cross corresponds to testing site 1, where the raman analysis was conducted on top of an LNMO particle. The black cross corresponds to testing site 2, where the Raman analysis was conducted between the LNMO particles.

To summarize, when Py was electropolymerized via a positive potential sweep to 4.1 V, a carbon-coating seemed to improve the uniformity of the resulting PPy-layer on the LNMO electrode compared to the LNMO electrodes without carbon-coating. Nevertheless, the surface morphology of the PPy layer changed when the potential was swept to 4.9 V, which is the operating voltage of LNMO-based cells. As the chemical composition of this layer was not further investigated, future studies should conduct an X-ray photoelectron spectroscopy (XPS) analysis to identify its chemical composition. The next part of the project focuses on studying the combined effect of a PPy coating and a carbon coating on the electrochemical properties of LNMO-based cells.

### 4.2.3 Effect of PPy-layer on the electrochemical performance of LNMO

The effect of an in-situ formed PPy-layer on the electrochemical performance of pristine and carbon-coated LNMO particles was examined using galvanostatic cycling (GC). Figure 4.24 presents the charge-discharge profiles obtained from cycling half-coin cells between 3.0 - 4.95 V with pristine LNMO, R6T10-C/LNMO, and R6T20-C/LNMO electrodes in a 1M $LiPF_6$, EC:DMC:DEC (1:1:1) electrolyte system with 0.5 wt%Py additive. All cells display the characteristic behavior of a disordered LNMO electrode material, exhibiting distinct plateaus at about 4.75 V ($Ni^{4+/3+}$), 4.7 V ($Ni^{4+/3+}$) and 4.2 ($Mn^{3+/2+}$). Charge-discharge plots of the presented cells parallels are attached in Figure A.2 in Appendix A.

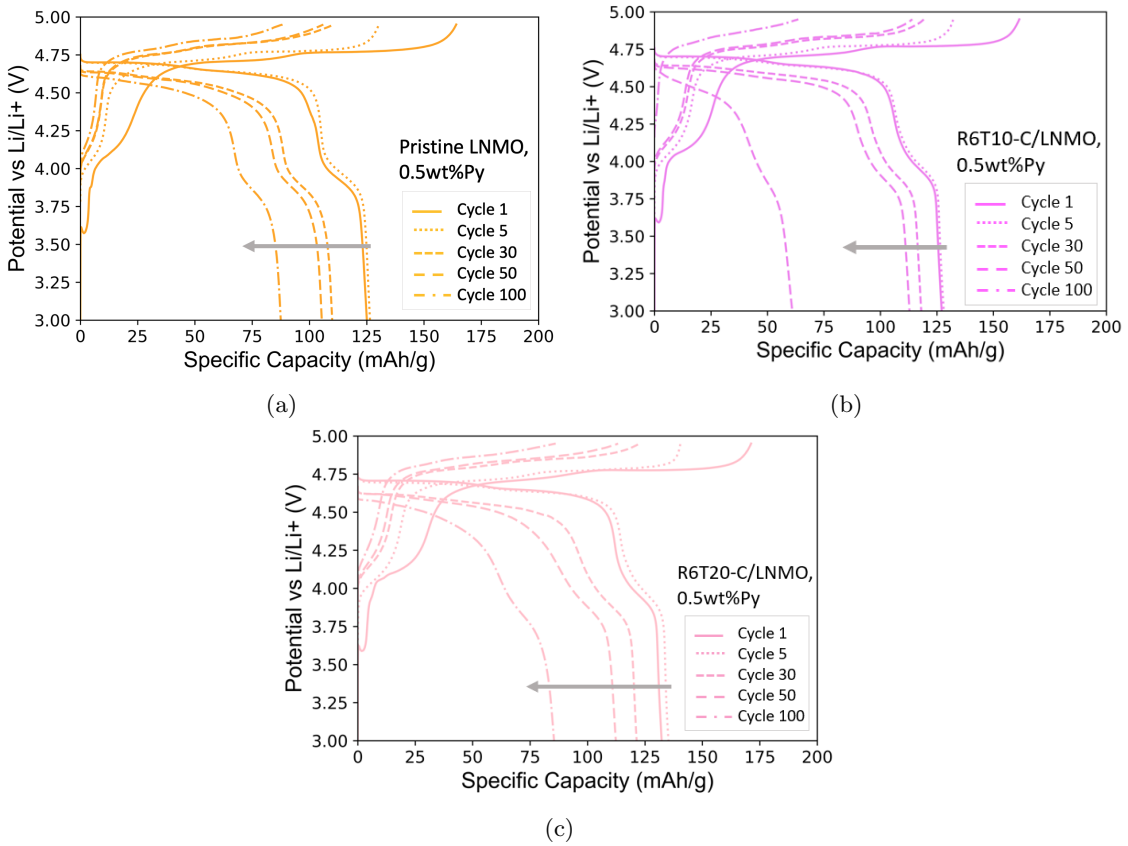


Figure 4.24: Charge-discharge plot of coin half-cells with pristine and carbon-coated LNMO electrodes (R6T10-C/LNMO and R6T20-C/LNMO) with 0.5 %Py electrolyte additive. The specific capacity (mAh/g) is plotted as a function of voltage (V vs. $Li/Li^+$) for cycles 1-5 at C/20 and cycles 5-100 at C/10.

The 1st and 2nd cycle of the above-presented cells with Py and the cells presented in Figure 4.8 without Py, including a section of the beginning of charge is shown in Figure 4.25. Independent of whether the cells are coated with carbon or contain the Py additive, the charge-discharge profiles of all cells are relatively similar. However, as apparent from the zoomed-in section of the 1st cycle, when reaching about 3.6 V, the cells containing Py experience a voltage drop accompanied by an earlier contribution to capacity compared to the cells without Py. This may suggest that a portion of the current is used to oxidize Py, thus initiating an electropolymerization process. This behavior is not observed in the 2nd cycle, implying that all Py has been consumed during the 1st cycle. This observation is consistent with the previously presented voltammograms in Figure 4.20, where an oxidation peak at about 3.7 V was exclusively observed during the initial cycle when the potential was swept in a positive direction for the cells containing Py. Despite the oxidation peak at 3.7 V from CV being slightly higher than the voltage drop occurring at 3.6 V from GC, these voltages are assumed to correspond to the same electropolymerization process.

The mean coulombic efficiency (CE) of the cells with the Py additive from the cells displayed in Figure 4.24 are presented in Table 4.4. Following the formation cycles (5 cycles), all cells demonstrated a stable CE of 98-99.3% up 100 cycles. The CE was notably lower in the 1st cycle, where all cells displayed a similar initial CE of about 74.7-75.5 %. In Section 2.7.1, it was discussed that during the formation of a PPy layer, the $PF_6^-$ anion is typically doped into the PPy structure to maintain charge balance, and $Li^+$ should not be consumed in this process. Therefore, a possible explanation for the low initial CE rather than $Li^+$ being consumed during the electropolymerization process, could be that the PPy layer hindered the transport of $Li^+$ from the LNMO and through the PPy-layer during charge, thereby reducing the availability of $Li^+$ for the discharge process. From the 1st cycle in Figure 4.25a, the cells containing Py have a higher charge capacity than the cells without Py. This may indicate that the PPy layer formed at the beginning of the charge is being overcharged. This effect may also explain the lower initial CE for

the cells containing Py. Irreversible overcharging may introduce a risk of overoxidation, potentially leading to a degradation of the polymer's electroactivity. The formation of an SEI and a CEI layer may also have contributed to the lower initial CE. However, this contribution is expected to be minimal since the initial CE of the cells containing Py is notably lower than those without Py (Table 4.2). No discernible differences between the cells with pristine and carbon-coated LNMO electrodes with the Py additive are observed.

Table 4.3: Mean coulombic efficiency from long-term galvanostatic cycling (GC) from three-parallel coin half-cells with pristine and carbon-coated LNMO electrodes (R6T10-C/LNMO and R6T20-C/LNMO) with the Py electrolyte additive. Cycles 1-5 had a C-rate of C/20, while cycles 5-100 had a C-rate of C/10.

| Cell | Pristine LNMO | R6T10-C/LNMO | R6T20-C/LNMO |
|---|---|---|---|
| Cycle nr. | C.E (%) | C.E (%) | C.E (%) |
| 1 | 74.7 | 75.5 | 74.9 |
| 5 | 96.9 | 96.7 | 96.2 |
| 30 | 99.3 | 99.1 | 99.0 |
| 50 | 99.4 | 99.1 | 99.0 |
| 100 | 99.3 | 98.1 | 99.0 |

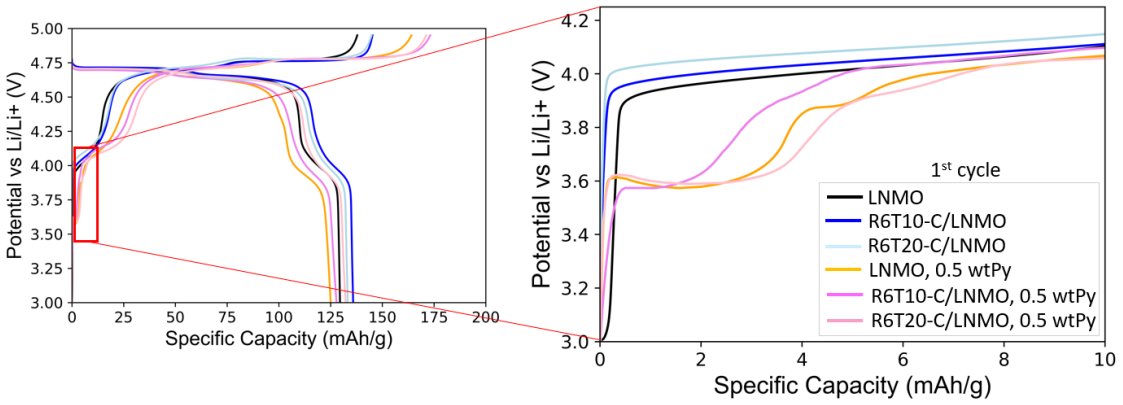


(a)

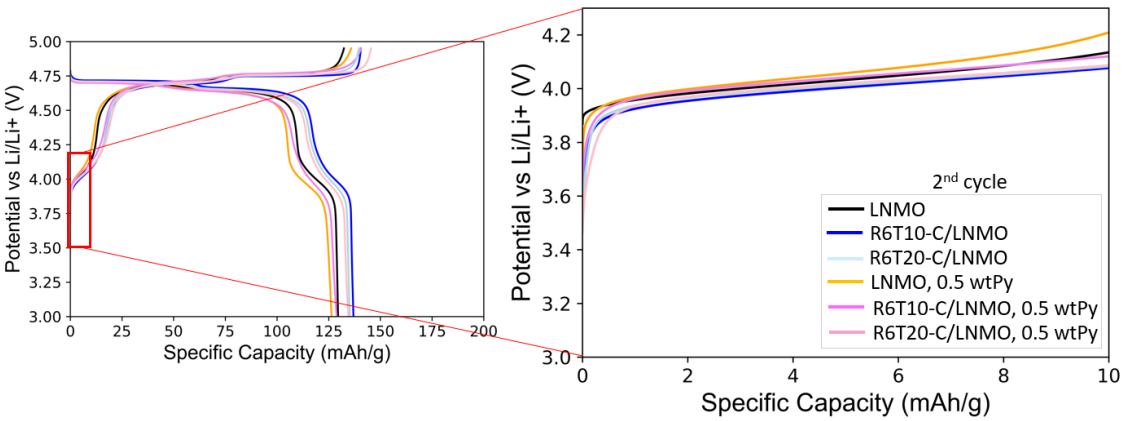


(b)

Figure 4.25: Charge-discharge plot of coin half-cells with pristine and carbon-coated LNMO electrodes (R6T10-C/LNMO and R6T20-C/LNMO) with and without 0.5 %Py electrolyte additive. Figure (a) shows the 1st cycle while (b) shows the 2nd cycle. Both figures include a zoomed-in section of the beginning of charge, and all cells are charged/discharged at C/20.

Given that a PPy-layer is formed on the LNMO surface upon the 1st charge half-cycle, as strongly indicated from the above-discussed results, it could be assumed that a PPy-layer is present in all

subsequent cycles. The mean initial discharge capacity and the capacity retention after 60, 80, and 100 cycles of three parallels of the cells shown in Figure 4.24 are presented in Table 4.4. The pristine LNMO, R6T10-C/LNMO, and R6T10-C/LNMO with 0.5 wt%Py had an average initial discharge capacity of 121, 126, and 131 mAh/g, respectively. The initial discharge capacity of all cells containing Py is generally lower than for the cells without the Py additive, which had an initial discharge capacity of about 134 mAh/g (Table 4.1). The PPy layer should be electrochemically active during charge and discharge and due to its lower specific capacity (72 mAh/g) compared to LNMO (140 mAh/g), the lower initial capacity was expected [40, 41]. These results align with previous studies, such as Gao et al. [12], who also reported a reduced initial capacity for their PPy-coated LNMO cells (112.9 mAh/g) compared to their pristine LNMO cells (116 mAh/g). It is, however, uncertain whether the lower initial capacity can solely be attributed to the PPy-layer contribution to the capacity, or if the functional properties of the PPy-layer have been degraded due to exposure to high voltages (4.95V) leading to a decreased capacity. The cells with carbon-coated LNMO particles demonstrated a generally higher initial discharge capacity compared to the cells with pristine LNMO, where the LNMO particles hybridized for 20 minutes (R6T20-C/LNMO) had the highest initial capacity. As discussed in Section 4.1.2, the R6T20-C/LNMO particles appeared to have denser, more evenly distributed, and more uniform carbon coating compared to the R6T10-C/LNMO particles. Therefore, a possible explanation for the higher initial discharge capacity of the R6T20-C/LNMO could be that the PPy-layer deposited more evenly on LNMO particles with a more uniform carbon coating. However, since a PPy-layer is not expected to contribute to increased discharge capacity, it remains unclear why a potentially more uniform PPy-layer results in a higher initial discharge capacity. In future work, to examine if the PPy-layer is more uniform on the R6T20-C/LNMO electrodes than the pristine LNMO and the R6T10-C/LNMO electrodes, the electrodes should be examined post-most cycling using SEM and Transmission Electron Microscopy (TEM).

Table 4.4: Mean initial discharge capacity and capacity retention from long-term galvanostatic cycling (GC) from three-parallel coin half-cells with pristine and carbon-coated LNMO electrodes (R6T10-C/LNMO and R6T20-C/LNMO) with 0.5 %Py electrolyte additive.

| Cell. | Initial discharge cap. (mAh/g) | Cap. retention (%) 60 cycles | Cap. retention (%) 80 cycles | Cap. retention (%) 100 cycles |
|---|---|---|---|---|
| Pristine LNMO, 0.5 wt%Py | 121 (±5.7) | 84 | 79 | 72 |
| R6T10-C/LNMO, 0.5 wt%Py | 126 (±2.7) | 87 | 79 | 58 |
| R6T20-C/LNMO, 0.5 wt%Py | 131 (±0.87) | 79 | 68 | 56 |

A plot of the long-term cycling performance of the pristine LNMO, R6T10-C/LNMO and R6T20-C/LNMO cells with and without the Py electrolyte additive, is presented in Figure 4.26. The performance of the cells without Py was previously discussed in Section 4.1.3. When the C-rate was increased from C/20 to C/10 after the formation cycles, the pristine LNMO and the R6T10-C/LNMO cells with Py experienced a capacity fade similar to the pristine LNMO without Py. Such a capacity fade was not observed for the R6T10-C/LNMO cell without Py, and the PPy-layer assumed to have formed during the first charge half-cycle seems to have worsened the cell's performance. The R6T20-C/LNMO cell with Py displayed a similar behavior to the R6T20-C/LNMO without Py when the C-rate was increased from C/20 to C/10.

After 60 cycles, the pristine LNMO, R6T10-C/LNMO, and R6T20-C/LNMO with Py had a capacity retention of 84, 87, and 79 %, respectively. All cells displayed relatively similar capacity retention after 60 cycles compared to those without Py from Table 4.1, thus, the addition of Py did not contribute to increased cycling stability.

After 80 cycles, all cells containing Py had lost over 80 % of their initial discharge capacity. The pristine LNMO and R6T10-C/LNMO cells with Py had a capacity retention of 79%, while the R6T20-C/LNMO with Py had a capacity retention of 68%. The cells without Py had a capacity retention of 78% (pristine), 72% (R6T10-C/LNMO), and 81% (R6T20-C/LNMO). Thus, the R6T20-C/LNMO cell with Py experienced a larger capacity than the cell without Py. As discussed in Section 4.2.2 and shown in Figure 4.21, a carbon-coating did seem to improve the uniformity of the PPy layer on the LNMO electrodes. Additionally, the R6T20-C/LNMO particles appeared to have a more uniform carbon coating than the R6T20-C/LNMO particles. Therefore, given that a PPy-layer is formed upon the initial charge-half cycle, it could be assumed that

this layer would cover a larger fraction of the R6T20-C/LNMO electrodes than the cell with pristine LNMO and R6T10-C/LNMO electrodes. In section 4.2.1, it was also discussed that at high operating voltages (up to 4.9 V), the morphology of the characteristic PPy seems to change. Therefore, it was uncertain if such a change would affect the functional properties of the PPy layer. According to Krische et al. [46], conducting polymers tends to deteriorate upon charge and discharge due to overoxidation of the polymers as the oxidation of the Py monomer occurs at a higher potential than the redox process of the polymer. Therefore, a possible explanation for the lower cycling stability of the R6T20-C/LNMO cells with a PPy-layer may be that the high voltage led to overoxidation of the PPy layer which may have destroyed its functional properties, resulting in reduced electric conductivity. The reason why the pristine and R6T10-C/LNMO cell with Py did not experience a reduced capacity retention compared to the cells without Py, could be that the PPy layer did not cover the entire electrode, and the cycling performance was not affected by the poor functional properties of the PPy-layer. In future work, to further investigate how the PPy layer is affected by the high operating voltage and how this affects the PPy-layers functional properties, an X-ray photoelectron spectroscopy (XPS) analysis should be conducted.

After 100 cycles the pristine LNMO, R6T10-C/LNMO, and R6T20-C/LNMO with Py had a capacity retention of 72, 58, and 56 %, respectively. Hence, the cells with carbon-coated LNMO particles showed a significantly worse cycling stability than the pristine LNMO. However, it should be mentioned that after 80 cycles, all cells showed a relatively unstable cycling performance. This is evident from the deviation between the three parallels, as shown in Figure A.3 in Appendix A.

The cycling stability of all the cells with the Py additive, where a PPy-layer is assumed to be formed upon the inital charge half-cycle generally showed worse cycling stability than previously reported in the literature. For example, Gao et al. [12] achieved capacity retention of 76.7 % and 91 % after 300 cycles for their cell's pristine and PPy-coated LNMO particles, respectively. An in-situ formed PPy-layer on carbon-coated LNMO particles did not contribute to increased cycling stability or function as intended.

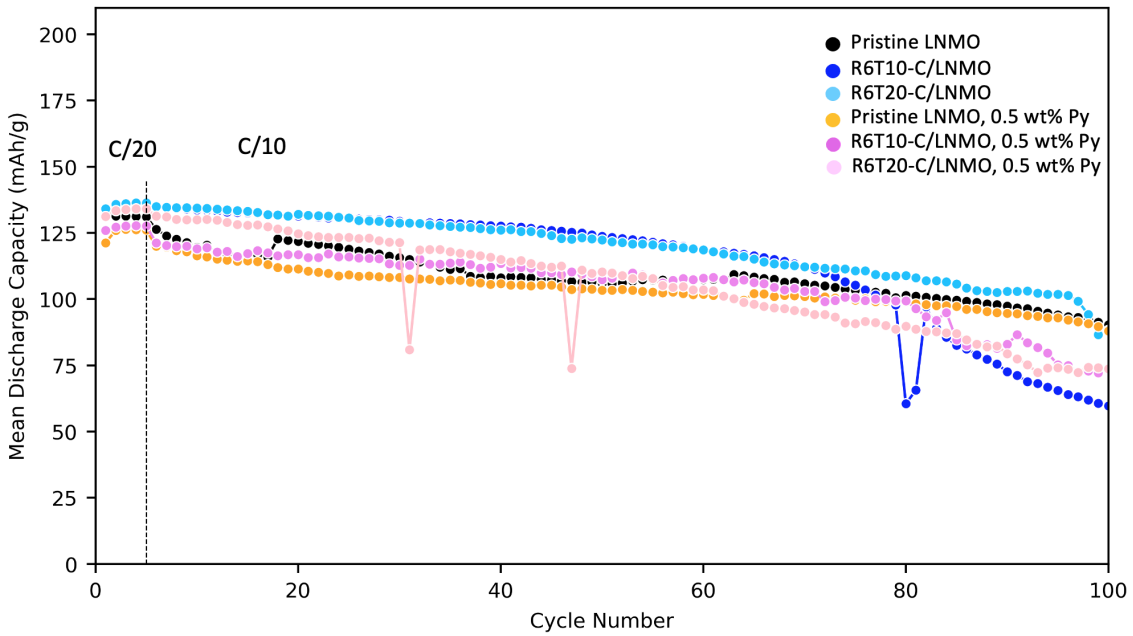


Figure 4.26: Mean specific discharge capacity as a function of cycle index of LNMO coin half-cells based on three parallels of the pristine LNMO and carbon coated LNMO electrodes (R6T10-C/LNMO and R6T20-C/LNMO) with and without 0.5 %Py additive. Cycles 1-5 have a C-rate of C/20, while cycles 5-100 have a C-rate of C/10.

# Chapter 5

# Conclusion

In this project, the aim was to develop a double-layer coating to enhance the stability of the LNMO electrode-electrolyte interface. The strategy was first to create a carbon coating, and then use Py as an electrolyte additive and electropolymerize it to form a protective coating on the carbon-LNMO composite during electrochemical cycling.

Using acetylene as a carbon source to form a carbon coating on the LNMO particles via the CVD method was not a success. The acetylene most likely resulted in a reducing atmosphere, ultimately leading to a decomposition of the LNMO structure.

Changing the coating processes to a dry coating process using a hybridizer machine and carbon black as the coating material, resulted in relatively thick (0-1.2 nm thickness) and non-uniform coatings. These carbon coatings did not affect the LNMO crystal structure. Despite the non-uniform and thick coating, the cells with carbon-coated LNMO demonstrated improved cycling stability (up to 60 cycles) and rate capability relative to non-carbon-coated cathodes. From an ICI test, the cells with carbon-coated LNMO showed reduced cell resistance at the beginning of the charge and the end of the discharge. A potential explanation for the enhanced electrochemical performance could therefore be due to enhanced electrical conductivity provided by the carbon coating. This may allow for better utilization of AM and improved electrical contact between the LNMO particles and the current collector. Additionally, the carbon coating might have acted as a protective barrier against the electrolyte, which also may have contributed to improved electrochemical performances.

From SEM images and Raman analysis, a PPy layer was confirmed to be present on the positive LNMO electrode from a positive CV scan (up to 4.1 V). Moreover, the PPy-layer on the carbon-coated LNMO appeared more uniform than the non-carbon-coated LNMO. The PPy layer was found to be formed during the initial charge half cycle both from CV and galvanostatic cycling tests. However, from galvanostatic cycling at high operating voltages (4.9 V), the PPy layer lead to poor cycling performance. A potential explanation for the reduced electrochemical performance could be that the PPy was overoxidized, which may have destroyed its functional and electrochemical properties.

It can be concluded that a pure carbon coating could lead to improved electrochemical performance of LNMO based cells. Additionally, a carbon coating does seem to help create a more uniform PPy coating. However, the PPy coating seems to worsen the cell performance due to instability at high operating voltages (4.9 V). Thus, an LNMO composite with a double-layer coating was developed in this project. However, it did not lead to enhanced electrochemical properties of LNMO based cells.

# Chapter 6

# Future work

Several aspects should be further examined to assess if carbon-coated LNMO and PPy-CB-coated LNMO are viable strategies to stabilize the LNMO electrode-electrolyte interface.
The uneven surface of the LNMO particles made it challenging to create a thin and uniform carbon coating using a hybridizer machine. The non-uniform and thick coating was most likely one of the main reasons for the large deviation in cycling stability after prolonged cycling. Therefore, one of the main focuses in future work should be to create a more uniform coating with a coating thickness below 70 nm. An alternative approach to achieve this could be to use graphite with a larger particle size that would function as a kind of "bedsheet bridge" over the gaps on the surface of the LNMO particle rather than filling the gaps with carbon. In previous research, coating thicknesses below 70 nm have been achieved by coating the LNMO with sucrose, carbon black, graphene oxide, reduced graphene oxide, or reduced graphene oxide via a wet chemical coating processes [14, 15, 16, 17, 18]. Therefore, using a wet chemical process with one of the mentioned carbon materials could also be an interesting alternative to explore further.

Further investigation is needed to evaluate the protective effect of carbon coatings against the dissolution of TMs from the LNMO structure. Specifically, the deposition of Ni and Mn on the counter electrode should be examined. To determine the extent of TM dissolution, prolonged cycling (more than 100 cycles) experiments are preferable. However, in our studies, all cells demonstrated an unstable cycling performance after only 80 cycles. The unstable cycling performance was partly attributed to the lack of optimization of mass loadings and general casting quality, as this was not the primary focus of this project. Therefore, once a coating thickness $< 70$ nm and a more uniform carbon coating are obtained, the casts should be optimized to compare the cells with carbon-coated and non-carbon-coated LNMO cells more accurately. Enhanced cycling stability will make determining the extent of TM dissolution easier. To expedite the effect of carbon coating, the cells should also be cycled at elevated temperatures to accelerate HF production and hence the TM dissolution.

Since the carbon-coated LNMO seems to reduce the contact resistance between the current collector and the LNMO particles, the possibility of reducing the amount of CB additive in the cathode cast should also be examined. By doing so, the amount of electrochemical inactive materials which does not contribute to the battery capacity could be minimized.

A carbon coating did seem to result in a more uniform PPy-coating. However, at high operating voltages (4.9 V), the PPy-layers surface morphology seems to change, and the cells containing Py display poor electrochemical properties. Therefore, the main focus of future work should be to obtain a more comprehensive understanding of how the high operating voltage affects the electrochemical and functional properties of the PPy layer. To achieve this, its chemical composition should be investigated via an X-ray photoelectron spectroscopy (XPS) analysis. The uniformity and morphology of the PPy layer should be examined using Transmission Electron Microscopy (TEM). In addition, an extensive literature review should be conducted to find a functional polymer that can be electropolymerized via anodic oxidation and is stable at high operating voltages.

Once the abovementioned points are achieved, the concept should be tested in full cells.

# References


[1] IEA. 'World Energy Outlook 2022'. In: *World Energy Outlook* (2022). ISSN: 1026-1141. DOI: 10.1787/3a469970-en.

[2] M Akhilash et al. 'A journey through layered cathode materials for lithium ion cells-From lithium cobalt oxide to lithium-rich transition metal oxides'. In: *Journal of Alloys and Compounds* 869 (2021), p. 159239. ISSN: 0925-8388. DOI: 10.1016/j.jallcom.2021.159239.

[3] Ting-Feng Yi, Jie Mei and Yan-Rong Zhu. 'Key strategies for enhancing the cycling stability and rate capacity of LiNi0.5Mn1.5O4 as high-voltage cathode materials for high power lithium-ion batteries'. In: *Journal of Power Sources* 316 (2016), pp. 85–105. ISSN: 0378-7753. DOI: 10.1016/j.jpowsour.2016.03.070.

[4] Linda Ager Wick Ellingsen et al. 'Life Cycle Assessment of a Lithium-Ion Battery Vehicle Pack'. In: *Journal of Industrial Ecology* 18.1 (2014), pp. 113–124. ISSN: 15309290. DOI: 10.1111/jiec.12072.

[5] Reiner Korthauer. *Lithium-Ion Batteries: Basics and Applications*. Ed. by Reiner Korthauer. Berlin, Heidelberg: Springer Berlin Heidelberg, 2018, pp. 1–413. ISBN: 978-3-662-53069-6. DOI: 10.1007/978-3-662-53071-9. URL: http://link.springer.com/10.1007/978-3-662-53071-9.

[6] John B Goodenough and Kyu-Sung Park. 'The Li-Ion Rechargeable Battery: A Perspective'. In: *Journal of the American Chemical Society* 135.4 (2013), pp. 1167–1176. ISSN: 0002-7863. DOI: 10.1021/ja3091438.

[7] Keith B. Oldham, Jan C. Myland and Alan M. Bond. 'Electrochemical Science and Technology'. In: (2018). DOI: 10.1002/9781119965992.

[8] Hyeon Jeong Lee et al. 'Ordered LiNi0.5Mn1.5O4 Cathode in Bis(fluorosulfonyl)imide-Based Ionic Liquid Electrolyte: Importance of the Cathode–Electrolyte Interphase'. In: *Chemistry of Materials* 33.4 (2021), pp. 1238–1248. ISSN: 0897-4756. DOI: 10.1021/acs.chemmater.0c04014.

[9] Xingwen Yu, Wiley A. Yu and Arumugam Manthiram. 'Advances and Prospects of High-Voltage Spinel Cathodes for Lithium-Based Batteries'. In: *Small Methods* 5.5 (2021), p. 2001196. ISSN: 2366-9608. DOI: 10.1002/smtd.202001196.

[10] Burak Aktekin et al. 'Cation Ordering and Oxygen Release in LiNi0.5-xMn1.5+xO4-Y (LNMO): In-Situ Neutron Diffraction and Performance in Li-Ion Full Cells'. In: (2018). DOI: 10.26434/chemrxiv.7200863.

[11] Elise R. Østli et al. 'Limitations of Ultrathin Al2O3 Coatings on LNMO Cathodes'. In: *ACS Omega* 6.45 (2021), pp. 30644–30655. ISSN: 2470-1343. DOI: 10.1021/acsomega.1c04457.

[12] Xuan-Wen Gao et al. 'Improving the electrochemical performance of the LiNi 0.5 Mn 1.5 O 4 spinel by polypyrrole coating as a cathode material for the lithium-ion battery'. In: *Journal of Materials Chemistry A* 3.1 (2014), pp. 404–411. ISSN: 2050-7488. DOI: 10.1039/c4ta04018j.

[13] Saïd Sadki et al. 'The mechanisms of pyrrole electropolymerization'. In: *Chemical Society Reviews* 29.5 (2000), pp. 283–293. ISSN: 0306-0012. DOI: 10.1039/a807124a.

[14] Tongyong Yang et al. 'Enhanced rate performance of carbon-coated LiNi0.5Mn1.5O4 cathode material for lithium ion batteries'. In: *Electrochimica Acta* 56.11 (2011), pp. 4058–4064. ISSN: 0013-4686. DOI: 10.1016/j.electacta.2010.12.109.

[15] Naiqing Zhang et al. 'A facile method to prepare hybrid LiNi0.5Mn1.5O4/C with enhanced rate performance'. In: *Journal of Alloys and Compounds* 509.9 (2011), pp. 3783–3786. ISSN: 0925-8388. DOI: 10.1016/j.jallcom.2010.12.188.

[16] Xin Fang et al. 'Graphene - oxide -coated LiNi 0.5 Mn 1.5 O 4 as high voltage cathode for lithium ion batteries with high energy density and long cycle life'. In: *Journal of Materials Chemistry A* 1.12 (2013), pp. 4083–4088. ISSN: 2050-7488. DOI: 10.1039/c3ta01534c.

[17] S. Monaco et al. 'Electrochemical performance of LiNi0.5Mn1.5O4 composite electrodes featuring carbons and reduced graphene oxide'. In: *Journal of Power Sources* 278 (2015), pp. 733–740. ISSN: 0378-7753. DOI: 10.1016/j.jpowsour.2014.12.099.

[18] Chao Gao et al. 'Enhanced rate performance of nanosized RGO-LiNi0.5Mn1.5O4 composites as cathode material by a solid-state assembly method'. In: *Ionics* 25.1 (2019), pp. 71–79. ISSN: 0947-7047. DOI: 10.1007/s11581-018-2599-y.

[19] Taejin Hwang et al. 'Surface-modified carbon nanotube coating on high-voltage LiNi0.5Mn1.5O4 cathodes for lithium ion batteries'. In: *Journal of Power Sources* 322 (2016), pp. 40–48. ISSN: 0378-7753. DOI: 10.1016/j.jpowsour.2016.04.118.

[20] Carl H. Hamann, Andrew Hamnett and Wolf Vielstrich. *Electrochemistry*. English. Second. Wiley-VCH Verlag GmbH & Co- KGaA. Weinheim. ISBN: 9783527310692.

[21] Elahe Talaie et al. 'Methods and Protocols for Electrochemical Energy Storage Materials Research'. In: *Chemistry of Materials* 29.1 (2017), pp. 90–105. ISSN: 0897-4756. DOI: 10.1021/acs.chemmater.6b02726.

[22] Jun Lu et al. 'High-Performance Anode Materials for Rechargeable Lithium-Ion Batteries'. In: *Electrochemical Energy Reviews* 1.1 (2018), pp. 35–53. ISSN: 25208136. DOI: 10.1007/s41918-018-0001-4. URL: https://doi.org/10.1007/s41918-018-0001-4.

[23] Xin Li et al. 'Review on comprehending and enhancing the initial Coulombic efficiency of anode materials in lithium-ion/sodium-ion batteries'. In: *Nano Energy* 77.June (2020), p. 105143. ISSN: 22112855. DOI: 10.1016/j.nanoen.2020.105143. URL: https://doi.org/10.1016/j.nanoen.2020.105143.

[24] 'The Development and Future of Lithium Ion Batteries'. In: *Journal of The Electrochemical Society* 164.1 (Dec. 2017), A5019–A5025. ISSN: 0013-4651.

[25] Nourhan Mohamed and Nageh K. Allam. 'Recent advances in the design of cathode materials for Li-ion batteries'. In: *RSC Advances* 10.37 (2020), pp. 21662–21685. DOI: 10.1039/d0ra03314f.

[26] Burak Aktekin et al. 'Cation Ordering and Oxygen Release in LiNi0.5-xMn1.5+xO4-Y (LNMO): In-Situ Neutron Diffraction and Performance in Li-Ion Full Cells'. In: (2018). DOI: 10.26434/chemrxiv.7200863.

[27] XiaoLong Xu et al. 'Research Progress in Improving the Cycling Stability of High-Voltage LiNi0.5Mn1.5O4 Cathode in Lithium-Ion Battery'. In: *Nano-Micro Letters* 9.2 (2017), p. 22. ISSN: 2311-6706. DOI: 10.1007/s40820-016-0123-3.

[28] Muharrem Kunduraci, Jafar F. Al-Sharab and Glenn G. Amatucci. 'High-Power Nanostructured LiMn2-xNixO4 High-Voltage Lithium-Ion Battery Electrode Materials: Electrochemical Impact of Electronic Conductivity and Morphology'. In: *Chemistry of Materials* 18.15 (2006), pp. 3585–3592. DOI: 10.1021/cm060729s. eprint: https://doi.org/10.1021/cm060729s. URL: https://doi.org/10.1021/cm060729s.

[29] Chaofeng Liu, Zachary G. Neale and Guozhong Cao. 'Understanding electrochemical potentials of cathode materials in rechargeable batteries'. In: *Materials Today* 19.2 (2016), pp. 109–123. ISSN: 1369-7021. DOI: 10.1016/j.mattod.2015.10.009.

[30] Kang Xu. 'Nonaqueous Liquid Electrolytes for Lithium-Based Rechargeable Batteries'. In: *Chemical Reviews* 104.10 (2004), pp. 4303–4418. ISSN: 0009-2665. DOI: 10.1021/cr030203g.

[31] Nicholas P. W. Pieczonka et al. 'Understanding Transition-Metal Dissolution Behavior in LiNi0.5Mn1.5O4 High-Voltage Spinel for Lithium Ion Batteries'. In: *The Journal of Physical Chemistry C* 117.31 (2013), pp. 15947–15957. ISSN: 1932-7447. DOI: 10.1021/jp405158m.

[32] Huizhe Niu et al. 'Recent Advances in Application of Ionic Liquids in Electrolyte of Lithium Ion Batteries'. In: *Journal of Energy Storage* 40 (2021), p. 102659. ISSN: 2352-152X. DOI: 10.1016/j.est.2021.102659.

[33] Zawar Alam Qureshi et al. 'Impact of coatings on the electrochemical performance of LiNi0.5Mn1.5O4 cathode materials: A focused review'. In: *Ceramics International* 48.6 (2022), pp. 7374–7392. ISSN: 0272-8842. DOI: 10.1016/j.ceramint.2021.12.118.

[34] Nicholas P. W. Pieczonka et al. 'Lithium Polyacrylate (LiPAA) as an Advanced Binder and a Passivating Agent for High-Voltage Li-Ion Batteries'. In: *Advanced Energy Materials* 5.23 (2015), p. 1501008. ISSN: 1614-6832. DOI: 10.1002/aenm.201501008.

[35] China, State Key Laboratory of Physical Chemistry of Solid Surfaces, Collaborative Innovation Center of Chemistry for Energy Materials, College of Chemistry and Chemical Engineering, Xiamen University, Xiamen 361005, P R and Weiqing Lin. 'Improving the Electrochemical Performance of LiNi0.5Mn1.5O4 Cathode Materials by Surface Coating with Cyclized Polyacrylonitrile for Lithium-Ion Batteries'. In: *International Journal of Electrochemical Science* (2017), pp. 12047–12059. DOI: 10.20964/2017.12.104.

[36] Taewhan Kim et al. 'Applications of Voltammetry in Lithium Ion Battery Research'. In: *Journal of Electrochemical Science and Technology* 11.1 (2020), pp. 14–25. ISSN: 2093-8551. DOI: 10.33961/jecst.2019.00619.

[37] Ting Wang et al. 'Improvement of the overall performances of LiMn2O4 via surface-modification by polypyrrole'. In: *Materials Research Bulletin* 71 (2015), pp. 91–97. ISSN: 0025-5408. DOI: 10.1016/j.materresbull.2015.06.051.

[38] Hongyu Dong et al. 'Improved High Temperature Performance of a Spinel LiNi0.5Mn1.5O4 Cathode for High-Voltage Lithium-Ion Batteries by Surface Modification of a Flexible Conductive Nanolayer'. In: *ACS Omega* 4.1 (2019), pp. 185–194. ISSN: 2470-1343. DOI: 10.1021/acsomega.8b02571.

[39] Evan Baltazzi and Lewis I Krimen. 'Recent Advances in the Chemistry of Pyrrole.' In: *Chemical Reviews* 63.5 (1963), pp. 511–556. ISSN: 0009-2665. DOI: 10.1021/cr60225a004.

[40] Yun-Hui Huang, Kyu-Sung Park and John B. Goodenough. 'Improving Lithium Batteries by Tethering Carbon-Coated LiFePO4 to Polypyrrole'. In: *Journal of The Electrochemical Society* 153.12 (2006), A2282–A2286. ISSN: 0013-4651. DOI: 10.1149/1.2360769.

[41] Renáta Oriňáková, Andrea Fedorková and Andrej Oriňák. 'Effect of PPy/PEG conducting polymer film on electrochemical performance of LiFePO4 cathode material for Li-ion batteries'. In: *Chemical Papers* 67.8 (2013), pp. 860–875. ISSN: 0366-6352. DOI: 10.2478/s11696-013-0350-8.

[42] Dana Pantea et al. 'Electrical conductivity of thermal carbon blacks Influence of surface chemistry'. In: *Carbon* 39.8 (2001), pp. 1147–1158. ISSN: 0008-6223. DOI: 10.1016/s0008-6223(00)00239-6.

[43] Utkarsh D. Chavan, P. Prajith and Balasubramanian Kandasubramanian. 'POLYPYRROLE BASED CATHODE MATERIAL FOR BATTERY APPLICATION'. In: *Chemical Engineering Journal Advances* 12 (2022), p. 100416. ISSN: 2666-8211. DOI: 10.1016/j.ceja.2022.100416.

[44] G.X. Wang et al. 'An investigation of polypyrrole-LiFePO4 composite cathode materials for lithium-ion batteries'. In: *Electrochimica Acta* 50.24 (2005), pp. 4649–4654. ISSN: 0013-4686. DOI: 10.1016/j.electacta.2005.02.026.

[45] Xiaobo Zhu, Tobias Schulli and Lianzhou Wang. 'Stabilizing High-voltage Cathode Materials for Next-generation Li-ion Batteries'. In: *Chemical Research in Chinese Universities* 36.1 (2020), pp. 24–32. ISSN: 1005-9040. DOI: 10.1007/s40242-020-9103-8.

[46] B. Krische and M. Zagorska. 'Overoxidation in conducting polymers'. In: *Synthetic Metals* 28.1-2 (1989), pp. 257–262. ISSN: 0379-6779. DOI: 10.1016/0379-6779(89)90530-4.

[47] Gemeng Liang et al. 'Developing high-voltage spinel LiNi 0.5 Mn 1.5 O 4 cathodes for high-energy-density lithium-ion batteries: current achievements and future prospects'. In: *Journal of Materials Chemistry A* 8.31 (2020), pp. 15373–15398. ISSN: 2050-7488. DOI: 10.1039/d0ta02812f.

[48] Ziling Chen, Qian Zhang and Qijie Liang. 'Carbon-Coatings Improve Performance of Li-Ion Battery'. In: *Nanomaterials* 12.11 (2022), p. 1936. ISSN: 2079-4991. DOI: 10.3390/nano12111936.

[49] Brindha Ramasubramanian et al. 'Recent Development in Carbon-LiFePO4 Cathodes for Lithium-Ion Batteries: A Mini Review †'. In: *Batteries* 8.10 (2022), p. 133. DOI: 10.3390/batteries8100133.

[50] Seong-Ju Sim et al. 'Use of carbon coating on LiNi0.8Co0.1Mn0.1O2 cathode material for enhanced performances of lithium-ion batteries'. In: *Scientific Reports* 10.1 (2020), p. 11114. DOI: 10.1038/s41598-020-67818-5.

[51] Xin Qi et al. 'Investigation of PF 6 and TFSI anion intercalation into graphitized carbon blacks and its influence on high voltage lithium ion batteries'. In: *Physical Chemistry Chemical Physics* 16.46 (2014), pp. 25306–25313. ISSN: 1463-9076. DOI: 10.1039/c4cp04113e.

[52] Youngsu Kuk et al. 'Facile synthesis of high-performance LiFePO4-reduced graphene oxide composites using ball milling'. In: *Ionics* 26.6 (2020), pp. 2803–2812. ISSN: 0947-7047. DOI: 10.1007/s11581-019-03395-6.

[53] Yanqing Fu et al. 'LiFePO4-Graphene Composites as High-Performance Cathodes for Lithium-Ion Batteries: The Impact of Size and Morphology of Graphene'. In: *Materials* 12.6 (2019), p. 842. ISSN: 1996-1944. DOI: 10.3390/ma12060842.

[54] Sung Hoon Ha and Yun Jung Lee. 'Core–Shell LiFePO4/Carbon-Coated Reduced Graphene Oxide Hybrids for High-Power Lithium-Ion Battery Cathodes'. In: *Chemistry – A European Journal* 21.5 (2015), pp. 2132–2138. ISSN: 0947-6539. DOI: 10.1002/chem.201404952.

[55] Huilong Fei et al. 'LiFePO 4 nanoparticles encapsulated in graphene nanoshells for high-performance lithium-ion battery cathodes'. In: *Chemical Communications* 50.54 (2014), pp. 7117–7119. ISSN: 1359-7345. DOI: 10.1039/c4cc02123a.

[56] Chang Su et al. 'A novel LiFePO4/graphene/carbon composite as a performance-improved cathode material for lithium-ion batteries'. In: *Electrochimica Acta* 64 (2012), pp. 190–195. ISSN: 0013-4686. DOI: 10.1016/j.electacta.2012.01.014.

[57] Liang Bao et al. 'Olivine LiFePO4 nanocrystallites embedded in carbon-coating matrix for high power Li-ion batteries'. In: *Electrochimica Acta* 222 (2016), pp. 685–692. ISSN: 0013-4686. DOI: 10.1016/j.electacta.2016.11.024.

[58] Guodong Jiang et al. 'Enhanced performance of LiFePO4 originating from the synergistic effect of graphene modification and carbon coating'. In: *Journal of Alloys and Compounds* 767 (2018), pp. 528–537. ISSN: 0925-8388. DOI: 10.1016/j.jallcom.2018.07.078.

[59] Dong Jin Ku et al. 'Effects of carbon coating on LiNi0.5Mn1.5O4 cathode material for lithium ion batteries using an atmospheric microwave plasma torch'. In: *Surface and Coatings Technology* 376 (2019), pp. 25–30. ISSN: 0257-8972. DOI: 10.1016/j.surfcoat.2018.09.082.

[60] Jinglu Yu et al. 'Uniform Carbon Coating on Silicon Nanoparticles by Dynamic CVD Process for Electrochemical Lithium Storage'. In: *Industrial & Engineering Chemistry Research* 53.32 (2014), pp. 12697–12704. ISSN: 0888-5885. DOI: 10.1021/ie5010465.

[61] Chanikarn Tomon et al. 'Core-shell structure of LiMn2O4 cathode material reduces phase transition and Mn dissolution in Li-ion batteries'. In: *Communications Chemistry* 5.1 (2022), p. 54. DOI: 10.1038/s42004-022-00670-y.

[62] Robert Pfeffer et al. 'Synthesis of engineered particulates with tailored properties using dry particle coating'. In: *Powder Technology* 117.1-2 (2001), pp. 40–67. ISSN: 0032-5910. DOI: 10.1016/s0032-5910(01)00314-x.

[63] Takashi Kawaguchi, Hideya Nakamura and Satoru Watano. 'Parametric study of dry coating process of electrode particle with model material of sulfide solid electrolytes for all-solid-state battery'. In: *Powder Technology* 305 (2017), pp. 241–249. ISSN: 0032-5910. DOI: 10.1016/j.powtec.2016.09.085.

[64] Noémie Elgrishi et al. 'A Practical Beginner's Guide to Cyclic Voltammetry'. In: *Journal of Chemical Education* 95.2 (2018), pp. 197–206. ISSN: 0021-9584. DOI: 10.1021/acs.jchemed.7b00361.

[65] Shuo Yang et al. 'Electrochemical and Electronic Charge Transport Properties of Ni-Doped LiMn2O4 Spinel Obtained from Polyol-Mediated Synthesis'. In: *Materials* 11.5 (2018), p. 806. ISSN: 1996-1944. DOI: 10.3390/ma11050806.

[66] Ming Zhou and Jürgen Heinze. 'Electropolymerization of pyrrole and electrochemical study of polypyrrole: 1. Evidence for structural diversity of polypyrrole'. In: *Electrochimica Acta* 44.11 (1999), pp. 1733–1748. ISSN: 0013-4686. DOI: 10.1016/s0013-4686(98)00293-x.

[67] Zeyang Geng, Torbjörn Thiringer and Matthew J Lacey. 'Intermittent current interruption method for commercial lithium ion batteries aging characterization'. In: *arXiv* (2021). DOI: 10.48550/arxiv.2104.09260. eprint: 2104.09260.

[68] M. Kunduraci and G. G. Amatucci. 'Synthesis and Characterization of Nanostructured 4.7 V Li x Mn1.5Ni0.5O4 Spinels for High-Power Lithium-Ion Batteries'. In: *Journal of The Electrochemical Society* 153.7 (2006), A1345–A1352. ISSN: 0013-4651. DOI: 10.1149/1.2198110.

[69] Miroslawa Pawlyta, Jean-Noël Rouzaud and Stanislaw Duber. 'Raman microspectroscopy characterization of carbon blacks: Spectral analysis and structural information'. In: *Carbon* 84 (2015), pp. 479–490. ISSN: 0008-6223. DOI: 10.1016/j.carbon.2014.12.030.

[70] Stanislav Valtera et al. 'Dye-stimulated control of conducting polypyrrole morphology'. In: *RSC Advances* 7.81 (2017), pp. 51495–51505. ISSN: 2046-2069. DOI: 10.1039/c7ra10027b.

[71] Vaibhav Varade et al. 'Probing disorder and transport properties in polypyrrole thin-film devices by impedance and Raman spectroscopy'. In: *Journal of Physics D: Applied Physics* 46.36 (2013), p. 365306. ISSN: 0022-3727. DOI: 10.1088/0022-3727/46/36/365306.

[72] L. Boulet-Roblin et al. 'Versatile Approach Combining Theoretical and Experimental Aspects of Raman Spectroscopy To Investigate Battery Materials: The Case of the LiNi0.5Mn1.5O4 Spinel'. In: *The Journal of Physical Chemistry C* 120.30 (2016), pp. 16377–16382. ISSN: 1932-7447. DOI: 10.1021/acs.jpcc.6b04155.

[73] Silje Nornes Bryntesen et al. 'Opportunities for the State-of-the-Art Production of LIB Electrodes—A Review'. In: *Energies (Basel)* 14.5 (2021), p. 1406. ISSN: 1996-1073.

# Appendix A

# Parallels galvanostatic cycling results

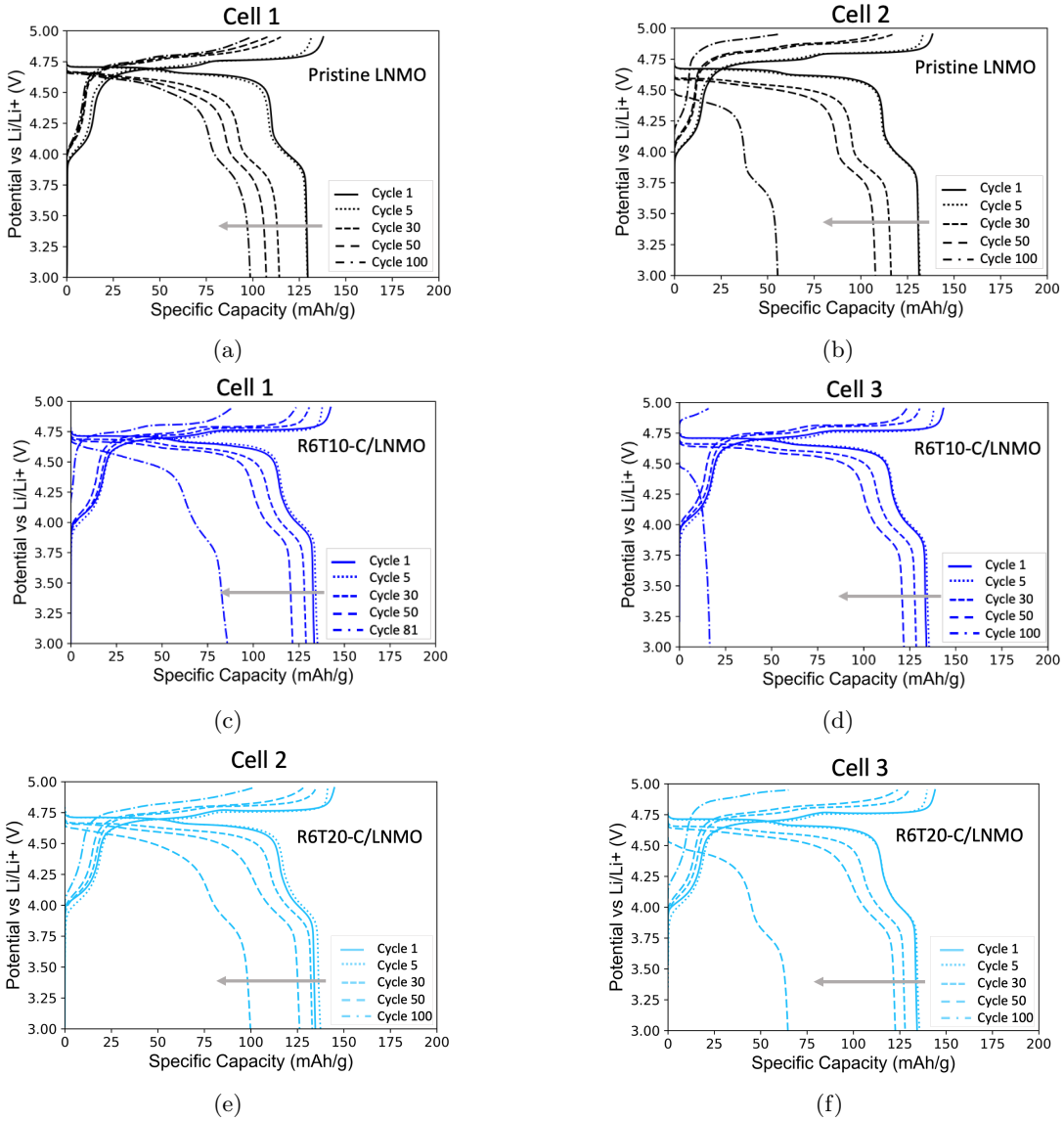


Figure A.1: Charge-discharge plot of coin half-cells with (a,b) pristine LNMO electrodes, (c,b) R6T10-C/LNMO electrodes, and (e,f) R6T20-C/LNMO electrodes. The specific capacity (mAh/g) is plotted as a function of voltage (V vs. $Li/Li^+$) for cycles 1-5 at C/20 and cycles 5-100 at C/10.

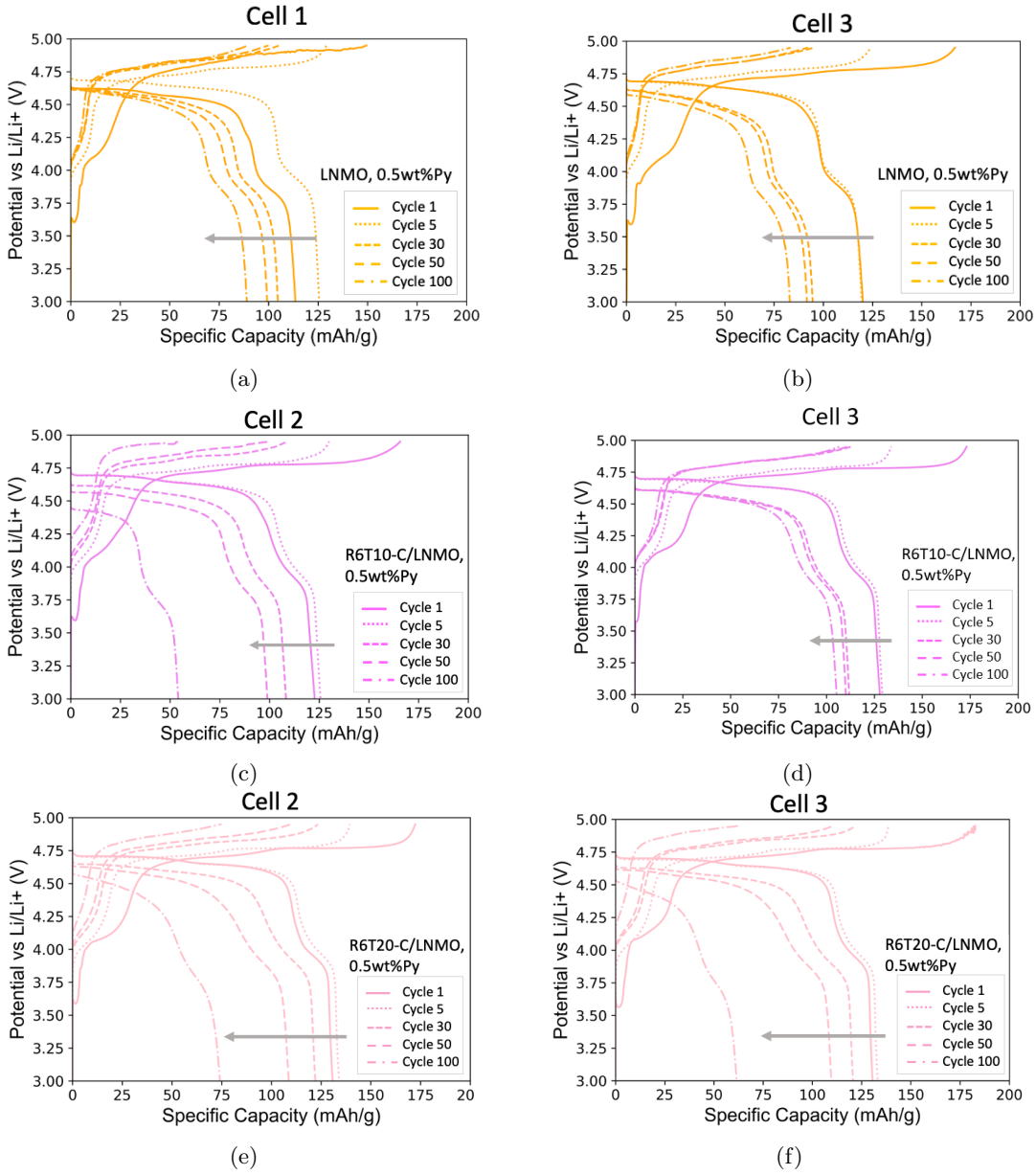


Figure A.2: Charge-discharge plot of coin half-cells with (a,b) pristine LNMO electrodes, (c,b) R6T10-C/LNMO electrodes, and (e,f) R6T20-C/LNMO electrodes with 0.5% pyrrole electrolyte additive. The specific capacity (mAh/g) is plotted as a function of voltage (V vs. $Li/Li^+$) for cycles 1-5 at C/20 and cycles 5-100 at C/10.

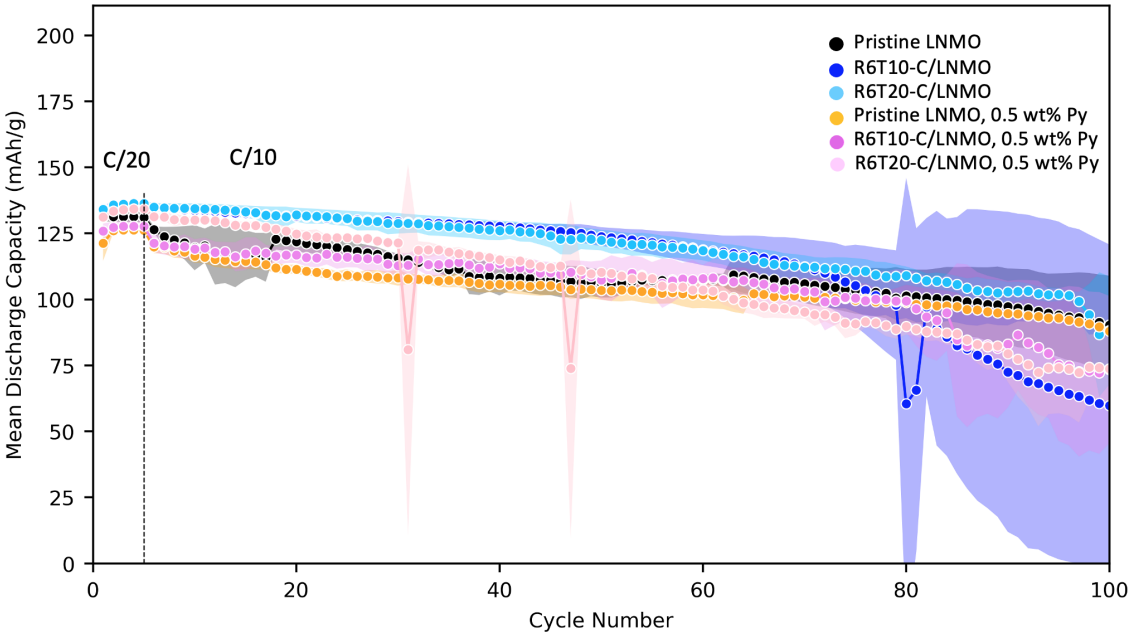


Figure A.3: Mean specific discharge capacity as a function of cycle index of LNMO coin half-cells based on three parallels of the pristine LNMO and carbon coated LNMO electrodes (R6T10-C/LNMO and R6T20-C/LNMO) with and without 0.5 %Py additive. Cycles 1-5 have a C-rate of C/20, while cycles 5-100 have a C-rate of C/10. The shaded area is the deviation between the different cell parallels.

# Appendix B

# Parallels intermittent current interruption

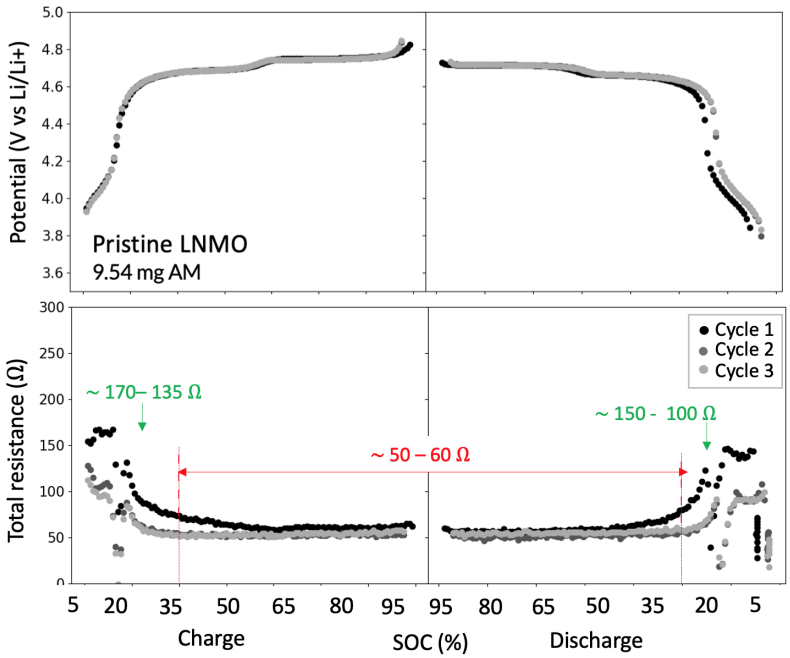


Figure B.1: The change in voltage with the corresponding change in total resistance as a function of the state of charge (SOC) from intermittent current interruption (ICI) tests of coin half-cells with a pristine LNMO electrode.

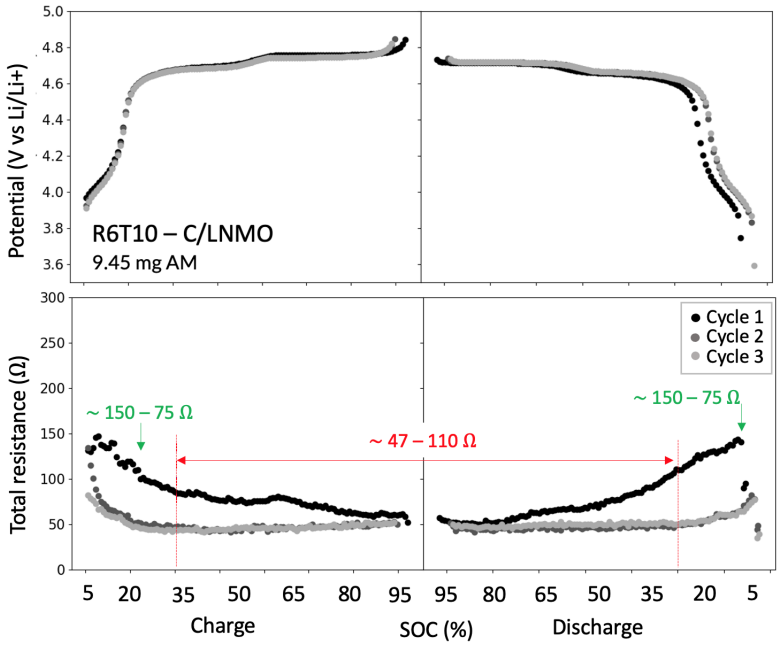


Figure B.2: The change in voltage with the corresponding change in total resistance as a function of the state of charge (SOC) from intermittent current interruption (ICI) tests of coin half-cells with a carbon-coated LNMO electrode (R6T10-C/LNMO).

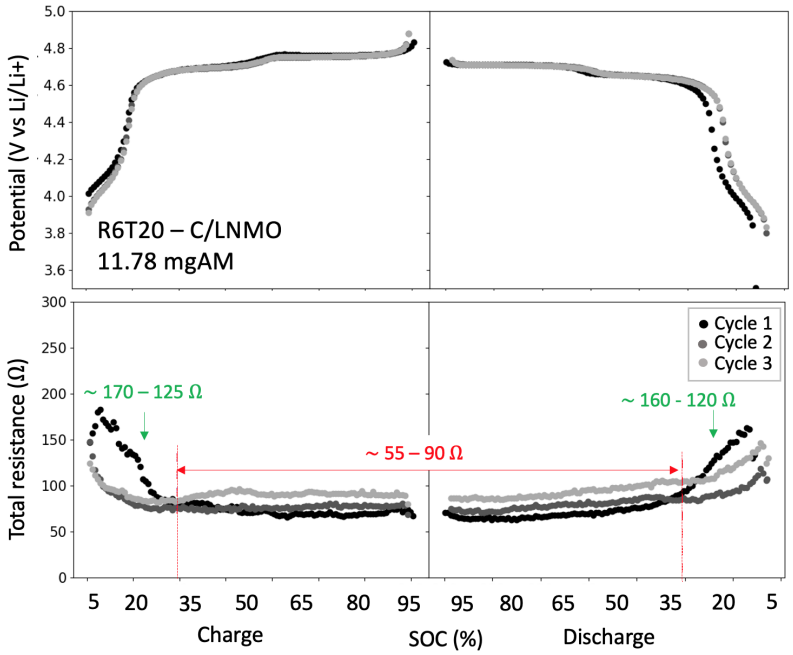


Figure B.3: The change in voltage with the corresponding change in total resistance as a function of the state of charge (SOC) from intermittent current interruption (ICI) tests of coin half-cells with a carbon-coated LNMO electrode (R6T20-C/LNMO).

# Appendix C

# Results Jun-Aug 2022, Al-Al electrodes

Figure C.1 shows the voltammograms obtained from three-electrode cells using Al as counter and working electrode with a varying weight percentage of pyrrole (Py). When the potential is swept up to 3.8 V a current of 0.008 mA for the 0 wt%Py cell and 1.2 mAh for the 5 wt%Py cell is achieved. The higher current of the 5 wt%Py cell compared to the 0 wt%Py cell indicates that Py has been electropolymerized to form polypyrrole (PPy). Oxidation and reduction peaks of the PPy-layer are also observed for the 5 wt%Py cells as denoted in Figure C.1b.

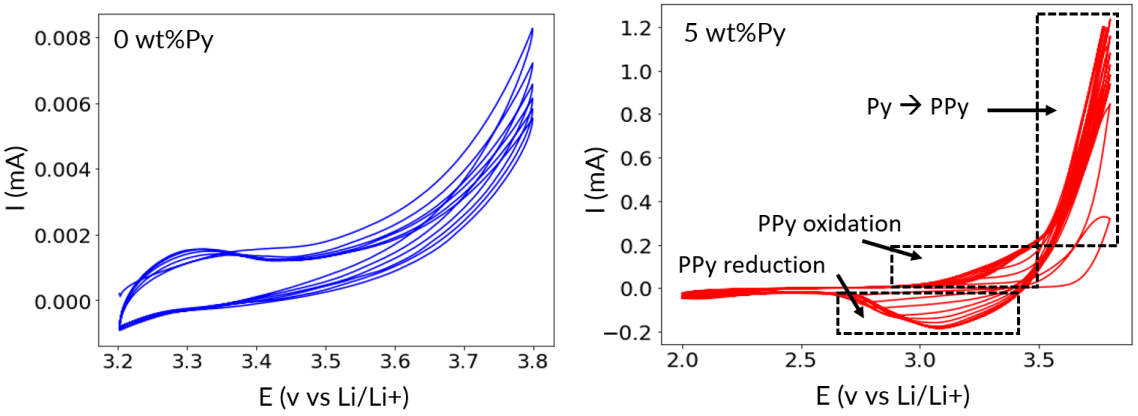


(a) (b)

Figure C.1: Voltammograms of three-electrode cells with Al as the working and counter electrode and Li as reference electrode, with a 1M $LiPF_6$, EC: DEC 1:1 with (a) 0 wt%Py, cell swept from 0V vs OCV to 3.8 V vs Li and back to 0 V vs OCV for 5 cycles (b) 5 wt%Py, swept from 0 V vs OCV to 3.8 V and back to 2 V vs Li for 10 cycles

From Table C.1, which is connected to the EDS spot analysis presented in Figure C.2, the nucleation sites with a spherical shape (Figure C.2a) and the areas with cauliflower/globular -like structure (Figure C.2b) and has an average concentration of 52.7 wt%C (±2.6) and 19.9 wt%F (±3.7) and 13.3 wt%N (±1.0). The high C, F, and N concentrations make sense as the PPy layer should mainly consist of C and N, and it should be doped with one F anion per 3 to 4 pyrrole unit. However, the C, F, and P signals may also originate from electrolyte decomposition or electrolyte residues.

A black layer with an average thickness of 4.2 $\mu$m, came off the Al - electrode and was attached to the separator, as shown in Figure C.3. It is most likely attached to the separator due to the rougher surface of the separator compared to the Al-electrode. However, this may indicate that a PPy film has been formed during CV. An average of 10.3 wt%N was found from spot EDS analysis from the remains of the PPy film on the Al cathode.

With relatively high certainty, a PPy-layer is formed on the Al working electrode through CV.

Table C.1: EDS results from spot analysis of Al cathode post-mortem CV of three electrode cells with a 1M $LiPF_6$, EC: DEC 1:1 and 5wt% Pyrrole electrolyte. The cell has been swept from 0V vs. OCV to 3.8V vs Li and back to 2V vs Li for 10 cycles. EDS values are connected to site 1-10 in Figure 4.

| **Wt%** | **1** | **2** | **3** | **4** | **5** | **6** | **7** | **8** | **9** | **10** |
|---|---|---|---|---|---|---|---|---|---|---|
| N | 14.8 | 13.3 | 12.5 | 14.0 | 12.5 | 12.8 | 14.2 | 11.9 | 0 | 0 |
| C | 56.5 | 50.4 | 53.1 | 54.2 | 52.7 | 53.4 | 53.6 | 47.7 | 0 | 8.3 |
| F | 17.4 | 23.4 | 12.5 | 19.8 | 18.4 | 21.9 | 22.3 | 23.1 | 8.4 | 12.6 |
| P | 6.0 | 6.2 | 4.4 | 6.1 | 6.4 | 6.2 | 5.7 | 6.0 | 3.8 | 3.9 |
| Al | 0.9 | 4.1 | 12.2 | 1.6 | 5.2 | 0.7 | 0 | 7.3 | 82.1 | 72.1 |

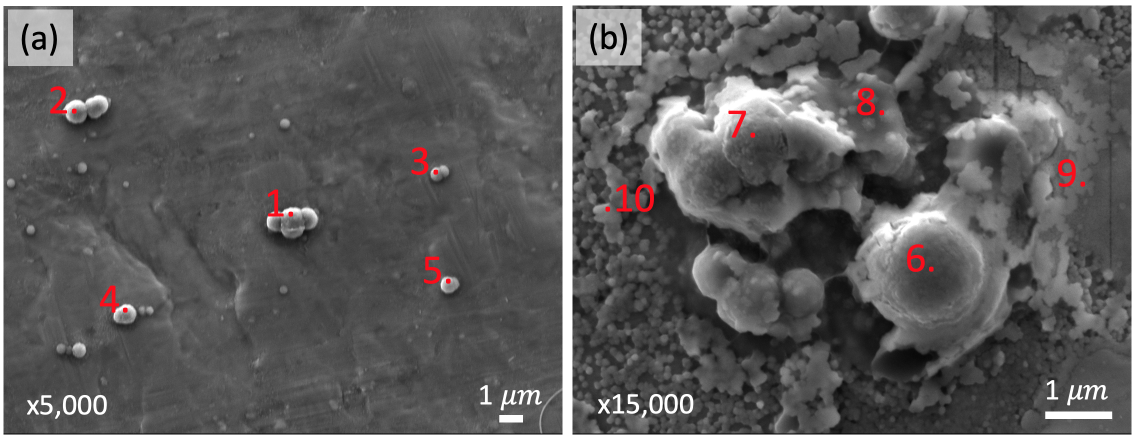


Figure C.2: SEM images of Al cathode post-mortem CV of three electrode cells with a 1M $LiPF_6$, EC: DEC 1:1 and 5wt% Pyrrole electrolyte system. The cell has been swept for ten cycles from 0V vs OCV to 3.8V and back to 2V vs Li. (a) PPy nucleation sites with a magnification of x5,000 (b) PPy growth from nucleation site magnification x15,000.

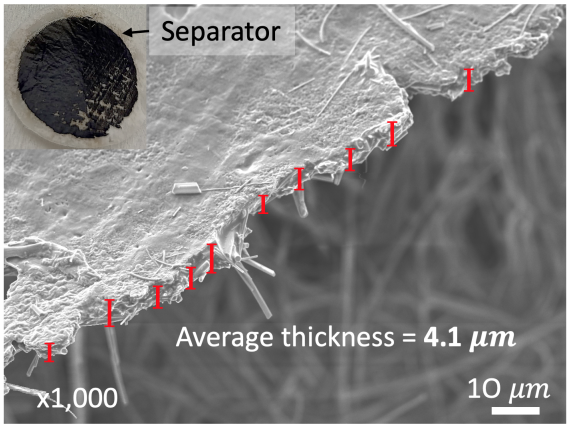


Figure C.3: SEM image of suspected PPy film on separator that came off the Al cathode after CV of three electrode cell with a 1M $LiPF_6$, EC: DEC 1:1 and 5wt% Pyrrole electrolyte system. The cell was swept from 0V vs. OCV to 3.8V vs Li and then 4V vs Li, a total of 10 cycles.

# Appendix D

# Main results Specialization Project Aug-Dec 2022

Figure D.1 and D.2 shows the charge-discharge profile of the first and second cycles from galvanostatic cycling of coin half cells with LNMO electrodes cycled against Li-metal in a 1M $LiPF_6$, EC:DMC:DEC (1:1:1) electrolyte system containing different weight percentages of pyrrole (Py). The Figures also include a section of their respective charge cycles. When reaching about 3.6 V vs. $Li/Li^+$, the cells containing Py experience a voltage drop accompanied by an earlier contribution to capacity compared to the cells without Py. This may suggest that a portion of the current is used to oxidize Py, thus initiating an electropolymerization process. This behavior indicate that a polypyrrole layer may have formed on the positive LNMO electrode.

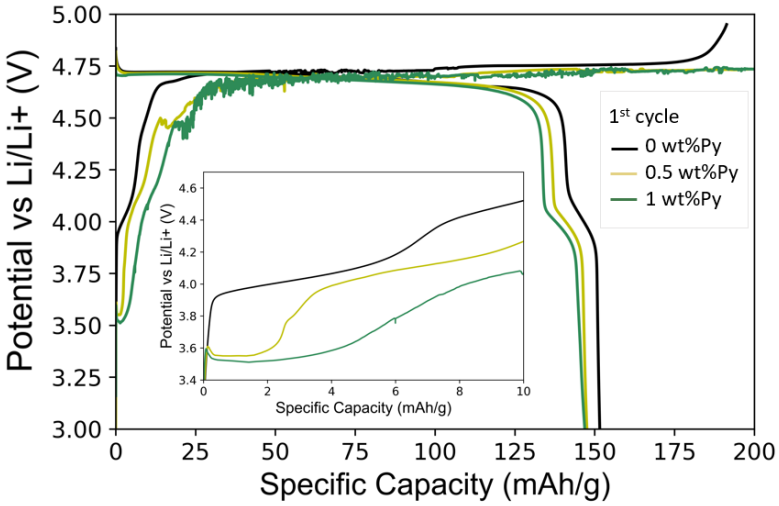


Figure D.1: Charge-discharge profile of the 1st cycle of an LNMO coin half-cells with various weight percentages of Py in a $LiPF_6$, EC:DMC:DEC (1:1:1) electrolyte system. The specific capacity (mAh/g) is plotted as a function of voltage (V vs $Li/Li^+$).

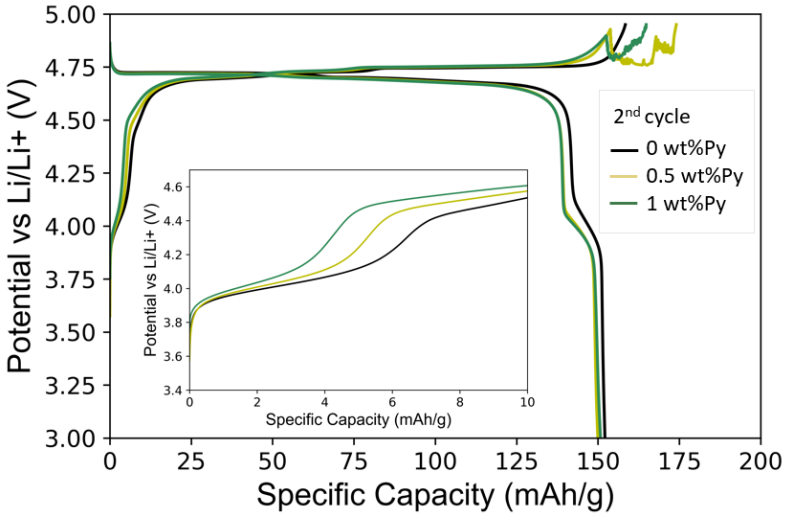


Figure D.2: Charge-discharge profile of the 2$^{nd}$ cycle of an LNMO coin half-cell with various weight percentages of Py in a $LiPF_6$, EC:DMC:DEC (1:1:1) electrolyte system. The specific capacity (mAh/g) is plotted as a function of voltage (V vs $Li/Li^+$).

Figure D.3 presents the surface morphology of a pristine LNMO cast, as well as the surface morphology of the LNMO electrodes post-mortem galvanostatic cycling with 0wt%Py and 0.5wt%Py. The LNMO particle is recognized from its spherical shape, while the smaller surrounding particles are the PVDF binder and carbon black additive. For the 0.5 wt%Py sample, chains seem to have formed between the smaller particles on top of the LNMO particle, and it appears different from the pristine and 0 wt% Py samples. This may indicate that a polypyrrole layer has deposited on the LNMO electrode during galvanostatic cycling. However, the polypyrrole layer seems to have a preferential growth in carbon-rich areas, resulting in a non-uniform coating. This makes sense since carbon has higher electronic conductivity than LNMO particles.

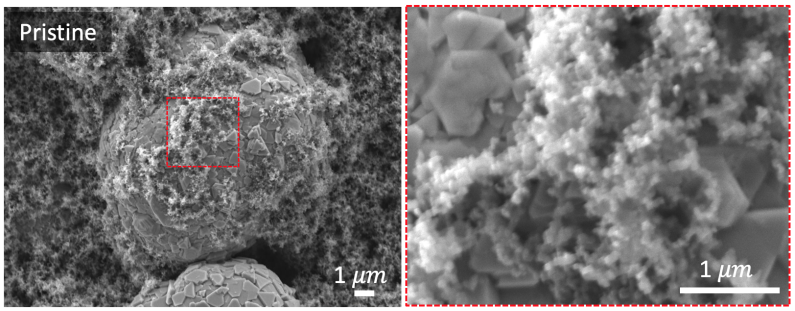


(a) 0 cycles

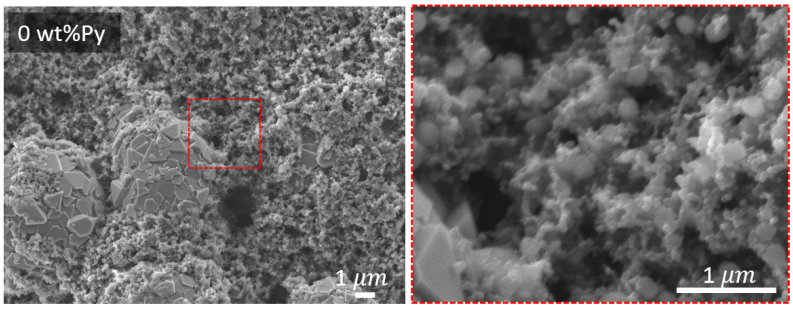


(b) 34 cycles

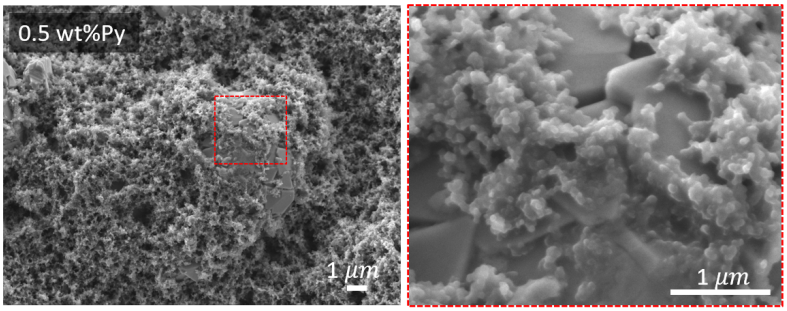


(c) 5 cycles

Figure D.3: SEM images of (a) A pristine LNMO electrode, and LNMO electrodes post-mortem galvanostatic cycling with (b) 0 wt%Py after 34 cycles and (c) 0.5 wt%Py after 5 cycles. Working distance 9.5 mm, magnification x5000 (right image) and x15000 (left image).

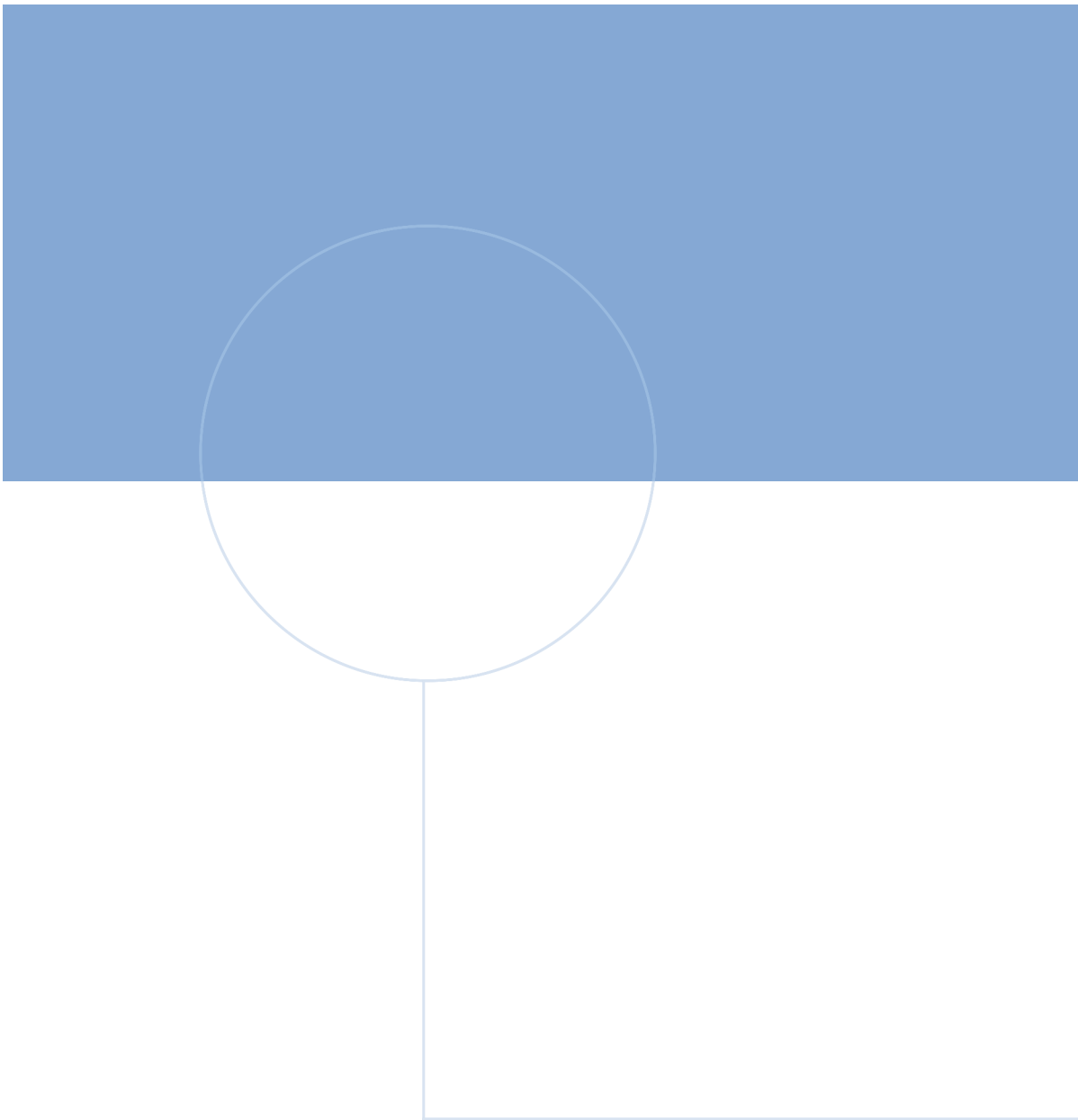

NTNU
Norwegian University of
Science and Technology

IFE Institutt for
energiteknikk